EXPLORING RELATIVISTIC GRAVITY WITH NUMERICAL SIMULATIONS

A Dissertation

Presented to the Faculty of the Graduate School

of Cornell University

in Partial Fulfillment of the Requirements for the Degree of

Doctor of Philosophy

by

François M. A. Hébert

January 2017

EXPLORING RELATIVISTIC GRAVITY WITH NUMERICAL SIMULATIONS

François M. A. Hébert, Ph.D.

Cornell University 2017

Numerical simulations play a key role in the study of systems where gravity is strong enough that it must be treated relativistically. In the first portion of this work, I apply a recent numerical method, the discontinuous Galerkin (DG) method, to improve the accuracy of simulations in which matter couples to strong gravity. I use the DG method to simultaneously evolve both the spacetime geometry and the matter on the same computational grid, and I deform this grid to conform to the problem symmetries. I show results for 3D evolutions of a Kerr black hole, a neutron star in which the spacetime metric is held fixed, and, finally, a neutron star where the spacetime and matter are both dynamical. These results mark the first application of the DG method to simultaneous evolution of the spacetime geometry and matter. The evolutions show long-term stability, good accuracy, and an improved rate of convergence as compared to evolutions with a comparable-resolution finite volume method.

In the second portion of this work, I contribute to the development of a new visualization technique for systems with strong gravitational fields. We present a method of calculating the strong-field gravitational lensing caused by many analytic and numerical spacetimes. We then use this method to simulate the visual distortions near isolated black holes and black hole binary systems; we produce both demonstrative images that illustrate details of the spatial distortion, and realistic images of collections of stars, taking both lensing amplification and redshift into account.

BIOGRAPHICAL SKETCH

François Hébert was born in Santa Barbara, CA, in 1987. He received his primary education by correspondence through the Centre national d'enseignement à distance, and he divided his remaining time between LEGOs and piano.

In 2005, François enrolled at the University of California, Santa Barbara, where he studied physics in the College of Creative Studies. He discovered the field of theoretical astrophysics during his senior thesis project — modeling sedimentation in low-mass helium white dwarf stars with Prof. Lars Bildsten. François became fascinated by this field for the varied and complex problems it presented, and he also acquired a growing interest in the use of computational approaches for solving physics problems.

François spent a gap year at JILA in Boulder, CO, visiting with the group of Prof. Juri Toomre. There, his work on magnetohydrodynamic simulations of stellar convection was his first experience in high-performance computing.

In 2010, François joined the Cornell physics graduate program with the intent of pursuing his interests in computational physics and astronomy. In Prof. Saul Teukolsky's group, which he joined in Summer 2011, François has been doing just that: implementing new algorithms that improve the accuracy and efficiency of numerical simulations of relativistic astrophysical systems.

When he is not doing science, François is likely to be ballroom dancing — an activity he shares with his partner in dance and life, Susanna Kohler. When the Ithaca weather permits it, he also enjoys cycling and hiking.

Upon completion of his Ph.D., François will be starting a postdoctoral position at Caltech, where he will continue his work in the field of numerical relativity.

This dissertation is dedicated to my parents,

with my gratitude for their love and support through my studies.

ACKNOWLEDGEMENTS

I first thank my advisor, Prof. Saul Teukolsky, for offering me the freedom to explore research directions to my satisfaction, for providing guidance when I needed it, and for being patient when I took on a few side projects. From Saul I have gained a better appreciation of what it means to be a scientist, to see to the heart of a problem, and to ask good questions.

I thank Dr. Larry Kidder for his mentorship and advice through many challenges in my research, and also for his help as I learned to work with the *Spectral Einstein Code*, the primary code I used in my research projects.

I thank Profs. Lars Bildsten, my undergraduate research advisor; Juri Toomre, my mentor during a gap year at JILA; Ram Nair, my mentor during a summer internship at the National Center for Atmospheric Research. All have shaped my understanding of astrophysics and/or computational science.

I thank my committee members, Profs. Éanna Flanagan and Matthias Liepe, for their guidance and instruction.

I thank the many members of the *Simulating eXtreme Spacetimes* collaboration, without whose prior work my own projects would not have been feasible.

For countless discussions, whiteboard physics sessions, board games, and comic relief, I thank the graduate students with whom I shared the sixth floor of the Space Science building — particularly Andy Bohn, Curran Muhlberger, Dan Hemberger, Jolyon Bloomfield, Kate Henriksson, Nils Deppe, and Will Throwe. I especially thank Andy and Will for the time we spent creating images of black hole binaries; this project remains a highlight of my time at Cornell.

Finally I thank my partner, Susanna Kohler, and my parents, Jean-Pierre and Claire Hébert, who have always provided a listening ear, support, and encouragement when I needed it — I wouldn't be here today without you.

TABLE OF CONTENTS

LIST OF TABLES

LIST OF FIGURES

PREFACE

Previously published work

Significant portions of this dissertation have been previously published, or are being prepared for publication, in the following journals:

- Chapter 2 is a manuscript currently being prepared for submission to *Physical Review D*;
- Chapter 3 is a paper [1] published in *Classical and Quantum Gravity*:

  What does a binary black hole merger look like?
  A. Bohn, W. Throwe, F. Hébert, K. Henriksson, D. Bunandar, M. A. Scheel, and N. W. Taylor, *Classical and Quantum Gravity*, March 2015.

CHAPTER 1

INTRODUCTION

The most energetic phenomena in the universe tap into gravity as their power source. The study of these events — whether through observational, theoretical, or computational approaches — can therefore provide key insights both into the physics of matter in strong gravitational fields and also into gravity itself.

In this dissertation I present two projects, both of which seek to improve the numerical simulations used to explore the behavior and effects of gravity in astrophysical scenarios. In my primary project, I focus on more accurately modeling systems that include both matter and gravitational forces strong enough for general-relativistic effects to become important. In my secondary project, I contribute to the development of a new technique for visualizing the merger of black hole binaries, a process driven by the emission of gravitational waves.

1.1 Astrophysical context

Two of the most energetic events in the universe are core-collapse supernovae and compact binary mergers, and both are ultimately powered by gravity. Much of what we know about the physics of these events, and the role that gravity plays in them, is dependent on observations of electromagnetic signatures and, now, gravitational waves. Observations alone are not enough, however; theoretical models are necessary to complete our understanding.

1.1.1 The role of observations

The first example of a gravitationally powered event, a core-collapse supernova, occurs at the end of a massive star's main-sequence life, when the mass of the accumulating iron core at its center surpasses the Chandrasekhar limit (1.4 $M_\odot$). At this point the degenerate electrons can no longer support the core against gravity, and it rapidly collapses to form a proto-neutron star. The enormous amount of gravitational binding energy released during this collapse powers a number of observables: a burst of gravitational waves, a 10^{53} erg pulse of neutrinos, and electromagnetic radiation emitted through various processes.

In the second example, a compact binary merger, a pair of black holes or neutron stars in a close binary orbit radiates energy in gravitational waves. This causes a slow gravity-driven decrease in the orbital separation (an "inspiral") and eventually leads to the merger of the two objects. For a binary system consisting of two black holes, there is no expected electromagnetic observable from the merger as there is no matter in the system; however, several percent of the system's mass-energy is radiated in the form of gravitational waves. If instead one or both members of the binary is a neutron star, the stellar matter can be tidally disrupted. In this case, gravitationally bound matter forms a radiating accretion disk around the merger remnant and may also launch a relativistic jet, observable as a gamma-ray burst. Unbound matter, rich in unstable heavy r-process elements, is heated by radioactive decay and can form a kilonova, detectable in optical and near-infrared wavelengths.

In the electromagnetic spectrum, gravitationally powered and highly energetic events like supernovae and compact binary mergers are observed as transients, with durations ranging from seconds (gamma-ray bursts) to weeks

(supernovae), which means they are typically detected by large-field surveys. Ground-based telescope survey campaigns such as *Sloan Digital Sky Survey* and the upcoming *Large Synoptic Survey Telescope* provide large datasets enabling a statistical understanding of supernovae. Complementing these are space-based observatories such as *Swift Gamma-ray Burst Mission* and the *Fermi Gamma-ray Space Telescope*, which survey the sky in the higher-energy wavelengths.

Besides learning about these events from their associated electromagnetic transients, we are now able to study them based on their gravitational-wave emission as well. With the recent first direct detection of a gravitational-wave signal [2] in September 2015 by the *Laser Interferometer Gravitational-Wave Observatory* (LIGO), we have entered the era of gravitational-wave astronomy. This first signal and a subsequent detection [3] are consistent with the mergers of binary black holes. As LIGO's sensitivity is further increased, it is predicted to additionally detect black hole-neutron star and binary neutron star mergers, and perhaps core-collapse events as well.

With electromagnetic and gravitational-wave observatories working in tandem, "multi-messenger" astronomy becomes possible. Observing a core-collapse or merger event through both channels has the potential to greatly increase constraints on the underlying dynamics, as each channel carries information about a different component of the physical system. The gravitational waves are emitted in the highest-density regions, and escape at the speed of light. Electromagnetic radiation is instead emitted in low-density regions further from the center of the system, and it can be delayed by the time needed for the energy to be transported to these regions.

1.1.2 The role of numerical relativity

As optical and gravitational-wave observatories increase in sensitivity, they will make increasingly numerous and precise observations of gravitationally powered events. In order to take full advantage of this data, it is important that we have the ability to explain and interpret the observations through theory.

For energetic astrophysical events such as those described above, computational approaches are necessary for any quantitative understanding of the dynamics. The spacetime geometry and matter are both dynamical and governed by highly non-linear evolution equations, resulting in a system of equations too complex for simple analysis. Nuclear reactions, neutrino physics, and magnetic fields can also play significant roles in systems with matter, further increasing the complexity. This is the origin of the field of *numerical relativity*: the use of numerical algorithms to study systems where gravity plays an important and dynamical role.

Numerical relativity has had many successes in the past decade. Today, several independent codes are capable of accurately simulating compact binaries through inspiral and merger [4]. These simulations provide the gravitational waveforms needed to calibrate (in the late inspiral and merger) the phenomenological models used in LIGO's analysis pipeline [5]. Simulations of black hole-neutron star binaries have constrained the parameter space in which the star is disrupted and an accretion disk forms [6]. In recent merger simulations where at least one binary companion is a magnetized neutron star, the formation of an accretion disk and relativistic jet has been shown [7, 8], marking a critical step toward understanding the precise origin of gamma-ray bursts. For the problem of core-collapse supernovae, where the mechanism that drives the accretion

shock to expand outwards and disrupt the star is still unknown, simulations are a crucial tool when assessing the importance of pre-collapse convective motions [9], neutrino treatment [10, 11], and other physics.

1.2 Discontinuous Galerkin evolutions of neutron stars

Over the past decade, numerical simulations of general-relativistic hydrodynamics (GR-hydro) have seen great progress in their stability and accuracy, enabling the computational study of energetic astrophysical events. From simulations of black hole-neutron star and binary neutron star mergers, we can explore the possible outcomes of the merger, as well as produce gravitational waveform templates. Of recent interest is the question of whether a post-merger accretion disk is able to launch a relativistic jet [7, 8], or whether a sufficient mass of unstable heavy elements is present in unbound disrupted stellar material to produce a kilonova [12]. From simulations of core-collapse supernovae, we can assess the importance of convective motions [9], neutrinos [10, 11], and other physics in reviving the accretion shock during the core collapse.

In spite of these many successes, GR-hydro simulation codes still face challenges. One challenge arises from the need to resolve the fluid turbulence over a large range of spatial scales, which requires very fine grids that are too computationally expensive to be practical. Furthermore, the presence of shocks and surfaces in the fluid reduces the order of convergence of the numerical method. As a result, GR-hydro simulations can struggle to reach the level of accuracy in their outputs required to constrain models from observations. In GR-hydro simulations of the inspiral of a binary neutron star, for example, the error in the

orbital phase can be over an order of magnitude larger than for a binary black hole inspiral [13], impacting the effectiveness of parameter estimation studies. A second example of insufficient accuracy comes from core-collapse simulations, where the accretion shock can stall or expand depending on the grid resolution [11], an indication that the simulations remain under-resolved.

An additional challenge for GR-hydro codes arises from the changing nature of supercomputing infrastructure: supercomputers are becoming progressively more parallel (i.e. more numerous processing cores), while their per-core performance gains are minimal. In order to perform simulations with increasingly detailed (i.e. expensive) physics, while making full use of future supercomputer hardware capabilities, it will be necessary for simulation codes to use algorithms that run efficiently on 10^6 or more cores. The algorithms in use today have communication patterns that typically do not lend themselves to such efficient scaling.

In efforts to improve the accuracy and scalability of simulation codes, discontinuous Galerkin (DG) methods have recently emerged as a promising contender for solving non-linear partial differential equations, but they have not yet seen much use in astrophysics. The first project in my dissertation explores the use of the DG method to improve the accuracy and scaling of GR-hydro simulations in numerical relativity. This work, detailed in Chapter 2, was done under the guidance of Prof. Saul Teukolsky and Dr. Larry Kidder. Below I discuss the features that make the DG method attractive for GR-hydro problems. I then describe the use of neutron star simulations as a benchmark and the implementation of the DG method within the *Spectral Einstein Code*.

1.2.1 Numerical methods for GR-hydro simulations

In GR-hydro simulations, two sets of coupled partial differential equations (PDEs) are solved simultaneously: the Einstein equations for the spacetime geometry, and the relativistic Euler equations for the hydrodynamics. The methods used to solve these PDEs by present-day numerical relativity codes fall under two broad categories: finite volume methods and spectral methods. I briefly describe their relative strengths, as this sets the stage for a discussion of the DG method.

Finite volume methods

Finite volume (FV) methods were developed to solve PDEs in conservative form, $\partial_t u + \nabla \cdot \vec{F}(u) = s$, for a conserved quantity u with a flux vector $\vec{F}(u)$ and source s. The equations of hydrodynamics — both Newtonian and relativistic — can be written in this form.

In a FV method, the simulation domain is partitioned into cells. Cartesian grids are the norm, with each cell a small cubical volume in the domain. On this grid, the solution is discretized by encoding the cell-averaged value of the solution u at a grid point at the cell center. The flux $\vec{F}$ is computed consistently at the interface between two neighboring cells, which results in a conservative method by construction. To obtain schemes with high accuracy, $\vec{F}$ is computed using a broad stencil, i.e. using data from several cells; this is the problem of flux reconstruction. In the neighborhood of shocks, the FV method is prone to spurious oscillations and overshoots in the solution because of Gibbs's phenomenon. So-called shock-capturing schemes ensure the solution remains physical in these regions.

Today, FV methods are the standard technique for solving the equations of relativistic hydrodynamics in GR-hydro codes. This method is favored for its robustness and for the shock-capturing schemes that enable handling fluid shocks and stellar surfaces. The FV method nevertheless has inherent limitations when used as a high-order method: the large stencils required for the corresponding differencing and shock-capturing schemes make it difficult to adapt the grid to the problem geometry, and can also lead to challenges in efficiently parallelizing the algorithm.

Many codes also use the FV method to solve the Einstein equations; although these PDEs cannot be written in conservative form, they take the similar hyperbolic form, and so much of the same formalism applies. The shock-capturing properties of the FV method are not needed for the smooth spacetime variables.

Spectral methods

Spectral methods also divide the computational domain into elements; these elements are typically large regions with simple topologies, such as cubes, spherical shells, etc. On each of these elements, a set of N polynomial basis functions is introduced. The solution u is expressed as an expansion over this basis. When the solution is a smooth function, the error in the expansion decreases exponentially as the order N is increased, giving rise to the exponential convergence of the spectral method. However, when there is a discontinuity in the solution u, the nice convergence properties of the method are lost. For this reason, spectral methods are not commonly used in fluid dynamics, where shocks can arise.

Spectral methods are in use today in the *Simulating eXtreme Spacetimes* collab-

oration's *Spectral Einstein Code* (SpEC) to produce numerous binary black hole merger simulations. The high accuracy of the spectral method permits long (tens of orbits) and efficient inspiral simulations with excellent control of the errors in the waveforms. When simulating binaries that contain one or two neutron stars, SpEC uses the spectral method to evolve the spacetime and a FV method to evolve the matter . This dual-grid approach allows the spacetime to be treated accurately and efficiently, while still correctly handling the fluid with its shocks and surfaces. However, there is substantial computational expense associated with communicating data between the spectral and FV grids, and the difficulties facing the FV method still apply.

Discontinuous Galerkin methods

Discontinuous Galerkin (DG) methods are, in an informal sense, a hybrid between spectral methods and FV methods. From spectral methods, DG methods draw the representation of the solution, on each element, as an expansion over a set of basis functions. From FV methods, DG methods draw the concepts that enable robust handling of the hydrodynamics: the use of a unique flux between neighboring elements to ensure conservation, and the shock-capturing techniques to handle discontinuities in the solution. As a result, DG methods combine the properties of exponential convergence in regions where the solution is smooth with the ability to handle shocks. In addition, they present several other desirable qualities:

1. geometric flexibility: the grid can be deformed to conform to the symmetries of the problem, or to the shape of an external domain boundary;
2. hp-adaptivity: the grid resolution can be tailored to the problem by adapt-

ing either the local order of approximation on the element (p-refinement), or the size of the (and the number of) elements (h-refinement); and,

3. local formulation: the method only requires exchanging data with nearest-neighbor elements, simplifying communication patterns and enabling good scaling on large machines.

The development of DG methods has undergone steady progress since the 1980s, with early emphasis on finding a stable formulation for non-linear conservation laws via the development of (low-order) shock-capturing schemes. More recently, in the early 2000s, work on more advanced WENO-based shock-capturing schemes [14, 15] promises to improve the accuracy of the method in problems with shocks. Paralleling these developments, the use of the DG method has expanded, with solutions to problems in electromagnetism, acoustics, plasma physics, gas dynamics, and atmospheric modeling.

The application of the DG method to problems in relativistic astrophysics is recent and remains, thus far, exploratory in nature.

The first use of a DG method for the evolution of spacetime geometry was by Zumbusch [16], who used a variational principle to obtain a space-time DG method for the linearized Einstein equations in harmonic gauge. For the commonly used Baumgarte-Shapiro-Shibata-Nakamura (BSSN) formulation of the Einstein equations, Field *et al.* [17] and later Brown *et al.* [18] developed DG methods in spherical symmetry. More recently, Miller and Schnetter [19] developed a DG method for the full BSSN equations in 3D, and showed success in evolving test problems.

Efforts on the hydrodynamics side began with Radice and Rezzolla [20], who

presented a formulation of DG for the evolution of fluids in curved spacetimes and evolved a neutron star in spherical symmetry. In their work, the spacetime is treated self-consistently by satisfying a radial constraint equation. In [21], Zhao and Tang implemented DG with a WENO shock-capturing scheme for special-relativistic hydrodynamics in 1D and 2D, and showed improved accuracy near shocks. Bugner *et al.* [22] were the first to apply DG to a 3D astrophysical fluid problem, evolving a neutron star in the Cowling approximation (in which the background metric remains fixed) and comparing different WENO schemes for handling of the star surface.

Prior to the work reported here, the use of a DG method to solve simultaneously the coupled system of spacetime geometry and general-relativistic hydrodynamics has not been attempted.

1.2.2 Neutron star evolutions

As the primary goal of this project is to determine whether the use of a DG method can improve the accuracy of simulations in GR-hydro, a benchmark test is needed with which to quantify the simulation errors. I simulate an isolated, non-rotating neutron star — a standard test case throughout the history of GR-hydro code development.

The neutron star is an ideal physical system for benchmarking new methods and algorithms: the matter and spacetime geometry are strongly coupled to each other, and both components must be correctly formulated and accurately resolved in order to preserve the equilibrium configuration of the star. At the star's surface, where the density vanishes, errors tend to be large as the code

attempts to resolve the discontinuity in the matter profile. This provides a good test of the code's handling of surfaces and weak shocks. Additionally, the existence of an exact solution enables quantitative analysis of the errors that arise during the evolution.

To perform the neutron star simulations, I implemented the DG method as a new module within the framework of the *Spectral Einstein Code* (SpEC). SpEC is (primarily) a compact-object binary simulation code maintained by the *Simulating eXtreme Spacetimes* collaboration. As part of its core code infrastructure, SpEC combines a PDE solver with techniques for solving Einstein's equations in single and binary compact object spacetimes, and is therefore well-suited to experiments in numerical relativity.

The SpEC framework provides many components needed in any simulation code. Components that were particularly useful when implementing the DG method include: grid-related algorithms (elements, mappings, basis functions and differentiation matrices), time-stepping algorithms, parallelization using the *Message Passing Interface* (MPI), and I/O. By implementing my DG code as a module of SpEC, I was able to build on this pre-existing work and focus my efforts on implementing the algorithms specific to the DG method itself.

New algorithms I added to SpEC for the DG module include: a new communication pattern for the data needed by the DG algorithm; numerical fluxes, which compute the unique flux in the conserved variables at the interface between neighboring elements; and slope limiters, a shock-capturing scheme that ensures that the solution remains physical near shocks.

1.2.3 Outcomes and future direction

Chapter 2 gives a detailed discussion of the formulation of the DG method and the algorithms implemented. It then describes the suite of tests used to validate the code and finally shows the results for neutron star evolutions using the DG method. I summarize the key results here:

- I show a stable evolution of a Kerr (isolated, spinning) black hole over long timescales ($10^4\ M_{\rm BH}$ in geometric units). This is the first time a black hole simulation in 3D using the DG method is shown.
- In the Cowling approximation (i.e. keeping the spacetime metric fixed), I evolve a neutron star for a duration of 50 ms ($10^4\ M_\odot$ in geometric units). I show that the evolution has well-controlled errors and recovers the first few oscillation mode frequencies expected from linear theory.
- I evolve the fully self-consistent neutron star for a duration of 50 ms. Again the errors are well-controlled, and I recover the first few oscillation mode frequencies from linear theory. This is the first time a self-consistently treated neutron star simulation using the DG method is shown.
- I compare the errors in the neutron star evolution when using the DG method versus a traditional FV method. I find the DG evolution has reduced errors and significantly less drift in the star's central density. The errors in the DG evolution also converge away more rapidly with increasing resolution, consistent with the higher-order nature of the method.

I conclude that the DG method shows excellent accuracy for simulations in GR-hydro. Further improvements in the accuracy could be obtained by the use of a higher-order shock-capturing scheme (e.g. WENO or sub-cell schemes) at

the surface of the star. While the low-order scheme I implemented is sufficient to obtain long and stable evolutions of neutron stars, it is the dominant source of error. The use of a grid conforming to the neutron star geometry increases the accuracy but is not fully general. An adaptive mesh refinement (AMR) scheme would allow for adapting the grid to more general problems.

While the results showed the expected accuracy properties from the DG method, I was unable to explore the method's scalability properties. As the underlying SpEC framework is optimized for use as a multi-domain spectral code with $O(10\text{–}100)$ spectral subdomains, it scales poorly to the large number of elements often used in DG simulations. In spite of several improvements to the data structures, I found that the memory usage and parallelism become inefficient when the domain approaches $O(10^4)$ elements. To address this shortcoming, work is underway on a new simulation code for GR-hydro problems, SpECTRE [23], designed for use with the DG method. This new code implements the task-based parallelism paradigm and has already shown good scaling to 10^6 elements on similarly many processors.

Future work towards performing astrophysical simulations with the DG method will focus on further developing the new SpECTRE code. It is in this code that an AMR infrastructure and high-order shock-capturing schemes will be implemented, tested, and used.

1.3 Gravitational lensing by black hole binaries

Simulations of merging black hole binaries are primarily carried out to generate gravitational waveform templates for LIGO data analysis. From the numerically

computed spacetimes of these simulations, it can also be interesting to visualize geometric quantities like the apparent horizons, the event horizons [24], or integral curves of the electric and magnetic parts of the Weyl tensor [25, 26]. Visualizations of these quantities are useful both for enabling an intuitive understanding of their behavior during the merger, and also for providing an engaging visual illustration of the merger process. However, the geometric quantities shown in these visualizations are not observable in practice in the binary black hole spacetime.

The second project in my dissertation develops a new visualization technique that aims to reproduce what an observer would see if they were watching a binary black hole merger. Photons are traced through the warped spacetime of the binary to compute the lensing effects due to the spacetime. Through this new approach, images and videos of the merger can be rendered. The work on this project is done in equal parts with Andy Bohn and Will Throwe; additionally, many other members of the *Simulating eXtreme Spacetimes* collaboration gave useful input and contributions. The details are discussed in Chapter 3 of this dissertation.

Our binary black hole lensing shares much with the (more commonly known) gravitational lensing of cosmology, but the magnitude of the photon deflections is significantly larger for lensing by black holes. The so-called strong gravitational lensing of cosmology describes the case where the lensing effects qualitatively alter the shape of the background galaxy — perhaps into an arc, a pair of images, or an Einstein ring. This strong lensing can occur when photon trajectories are deflected by as little as fractions of an arcsecond. In our visualizations, however, photons are traced near the black hole event horizons, where their trajectories

can (and do) take multiple orbits around the black holes.

1.3.1 Camera-to-sky mappings

To render an image, we must first determine the origin of each light ray that reaches the observer. We take the observer to be a simple pinhole camera, for which all measured light rays end at a fixed spacetime point, the pinhole aperture; the direction of the ray corresponds to the pixel it illuminates in the final image. To make the problem computationally tractable, we trace the light rays *away* from the camera, *backwards* in time, and determine their origin. Each light ray (i.e. null geodesic) is traced through the spacetime data using the geodesic equation, until it reaches a sufficiently large distance from the system. Each traced geodesic samples one point of the lensing map — the map from the camera's image plane to the sky.

To obtain a high-quality image, the rendering algorithm samples the camera-to-sky mapping multiple times per pixel, ensuring a smooth sampling of the light source. This proves to be computationally prohibitive for a high-resolution image with millions of pixels to be rendered, if each sample of the map requires tracing a geodesic.

My primary contribution to the project is therefore the development of an interpolation algorithm that approximates the sky-to-camera mapping to greatly reduce the required number of geodesics. In regions of the image far from the binary black holes, the lensing map is slowly varying, and it is possible to trace as few as one geodesic for every 100 pixels with no discernible loss of accuracy. In regions close to the black holes, where neighboring geodesics can take wildly

different trajectories, the mapping must be sampled more finely. I therefore implemented an adaptive algorithm, summarized below:

1. Define the parameters of the observer/camera.
2. Select geodesics that will be used to sample the camera-to-sky map.
3. Trace geodesics through the spacetime data.
4. Construct a continuous map by interpolating between the traced geodesics. If the interpolation is not sufficiently smooth, return to step 2 and select new geodesics that will improve the resolution of the map.
5. Finally, render the image by sampling the mapping.

In step 2, the first geodesics are selected to lie on a uniform rectilinear grid on the camera plane. On this grid, each set of four neighboring geodesics defines a patch on which the mapping is linearly interpolated. When an interpolation is not sufficiently smooth and step 2 is revisited, I select new geodesics by refining the grid on only those under-resolved patches.

In practice, I found that with five levels of grid refinement (i.e. a factor in 32 in geodesic spacing), a good balance is reached between the computational cost and the ability to resolve fine details in high-resolution images. This corresponds to an $O(100)$-fold reduction in the number of traced geodesics, while maintaining the quality of the final image. When using more refinement levels, it is possible to "zoom in" to portions of the image near the edge of a black hole shadow, where we discovered interesting structure.

The reduction in computation from the interpolation also made possible the production of movies at high (1080p) resolution of the inspiral and merger of

binary black holes, with each movie frame an independently ray-traced and rendered image.

1.3.2 Outcomes and future direction

Chapter 3 gives further discussion of this project, with an emphasis on understanding the different features visible in the lensing images of the binary black hole merger spacetime. We find that the images give some intuitive insights into the structure of the spacetime. Some of these insights are:

- We can identify frame-dragging visually by the distortion effects on the background.
- Each black hole lenses the shadow of the other black hole, creating secondary shadows. These are called the eyebrows because of their shape.
- We find evidence for self-similarity in the shadow structure. Visually, the eyebrows have eyebrows. The repeating shadows are caused by photons taking increasingly complex trajectories with many orbits around the black holes.

The images we produce additionally have the potential to serve as a valuable outreach and educational tool, as evidenced by their use in the press event announcing LIGO's first detection of a gravitational wave. One of our merger videos hosted on the *Simulating eXtreme Spacetimes* YouTube channel [27] has been viewed hundreds of thousands of times. The physically motivated, realistic nature of our images makes them better able to capture the imagination and inspire than previous visualization techniques.

Future continuation of this project could apply the visualization technique to different spacetimes. With lensing images from compact-object binaries with matter (a black hole-neutron star or a binary neutron star system), further insights may be gained and interesting new visualizations created.

CHAPTER 2

GENERAL-RELATIVISTIC NEUTRON STAR EVOLUTIONS WITH THE DISCONTINUOUS GALERKIN METHOD

Simulations of relativistic, astrophysical hydrodynamics often have need of both high accuracy and robust shock-handling properties. The discontinuous Galerkin (DG) method combines these features — a high order of convergence in regions where the solution is smooth, and shock-capturing properties for regions where it is not — with geometric flexibility, and is therefore well suited to solve the PDEs describing astrophysical scenarios. We present here evolutions of a general-relativistic neutron star with the DG method. In these simulations, we simultaneously evolve the spacetime geometry and the matter on the same computational grid, which we conform to the spherical geometry of the problem. To verify the correctness of our implementation, we perform standard convergence and shock tests. We then show results for evolving, in 3D, a Kerr black hole, a neutron star in the Cowling approximation (holding the spacetime metric fixed), and, finally, a neutron star where the spacetime and matter are both dynamical. These results mark the first application of the DG method to simultaneous evolution of the spacetime geometry and matter. The evolutions show long-term stability, good accuracy, and improved rate of convergence versus a comparable-resolution finite volume method.

2.1 Introduction

Numerical simulations are a crucial tool in the study of core-collapse supernovae, compact binary mergers, accretion disks with relativistic jets, and other energetic astrophysical sources. In these events, the dynamics are governed by the

high-density matter and its coupling to the strong gravitational field. Nuclear reactions, neutrino physics, and magnetic fields can also play significant roles. Because of the highly nonlinear nature of the underlying general-relativistic hydrodynamics (GR-hydro), simulations are necessary to obtain observable predictions from physics models. Achieving sufficient accuracy in the simulation outputs (e.g. gravitational waveforms, ejected masses, nucleosynthesis products) remains a challenge, however. High resolution is needed to resolve multi-scale fluid flows, and the presence of shocks in the matter reduces the accuracy of the numerical schemes.

The standard approach taken in present-day GR-hydro codes is to cast the partial differential equations into conservative form, and discretize them using a finite-volume (FV) method. The FV method is favored for its robustness and the various "shock-capturing" schemes to handle fluid shocks and stellar surfaces. The Einstein equations for the spacetime geometry are solved either by using the FV method, or by using a spectral method on a different computational grid. Over the past decade, the application of improved high-resolution shock-capturing schemes (e.g. PPM, WENO) and higher-order difference schemes has led to significant advances in the accuracy and stability of the numerical results. In spite of these successes, the FV method has inherent limitations when used as a high-order method: the large stencils required for the differencing and shock-capturing schemes make it difficult to adapt the grid to the problem geometry, and can also lead to challenges in efficiently parallelizing the algorithm.

In the pursuit of improved accuracy and efficiency, discontinuous Galerkin (DG) methods have recently emerged as a promising contender for astrophysical problems. DG methods share properties with both spectral methods and

FV methods — they inherit the high-order accuracy of the former for smooth solutions while maintaining the robust shock-handling properties of the latter. They are geometrically flexible, enabling the use of grids adapted to the problem geometry. They are well suited to hp-adaptivity, where the grid resolution can be set either by adjusting the order of the polynomial approximation within an element (p-refinement), or by adjusting the size of the element (h-refinement). Finally, DG methods are locally formulated, enabling efficient parallelization and good scaling.

The application of the DG method to problems in relativistic astrophysics is recent and remains exploratory in nature. The first evolution of the space-time geometry was by Zumbusch [16], who obtained a space-time DG scheme for the linearized vacuum Einstein equations in harmonic gauge. For the commonly used Baumgarte-Shapiro-Shibata-Nakamura (BSSN) formulation of the Einstein equations, Field *et al.* [17] and Brown *et al.* [18] developed DG schemes in spherical symmetry. More recently, Miller and Schnetter [19] developed an operator-based (vs. the typical differential equation-based) DG discretization of the BSSN equations, and showed success in evolving 3D test problems. Efforts on the hydrodynamics side began with Radice and Rezzolla [20], who presented a formulation of DG for the evolution of fluids in curved spacetimes and evolved a neutron star (NS) in spherical symmetry. In this work, the spacetime is treated self-consistently by satisfying a radial constraint equation. In [21], Zhao and Tang implemented DG with a WENO shock-capturing scheme for special-relativistic hydrodynamics in 1D and 2D. Bugner *et al.* [22] were the first to apply DG to a 3D astrophysical fluid problem, evolving a NS in the Cowling approximation (i.e. fixed background metric). In a new DG code using a task-based parallelism paradigm (SpECTRE), Kidder *et al*. [23] showed special-relativistic

magneto-hydrodynamic tests in 2D and 3D.

In this paper we use a DG method to evolve a NS in coupled GR-hydro in 3D for the first time. As tests of our implementation, we also evolve a NS in the Cowling approximation and a Kerr black hole (BH). In these simulations, we investigate the use of "cubed sphere" grids conforming to the spherical geometry of the BH and NS problems. We adopt the DG formulation described by Teukolsky [28], using the generalized harmonic formulation of Einstein's equations and the "València" formulation of the general-relativistic hydrodynamics.

We implement our DG code in the framework of the Spectral Einstein Code [29] (SpEC). SpEC combines a multi-domain penalty spectral method to evolve binary BH spacetimes [30, 31] with a FV method to evolve the matter in BH-NS [32] and NS-NS [33, 34] systems. Our DG GR-hydro code is independent from SpEC's FV component, and is instead built on the algorithms from SpEC's vacuum spectral code: spectral bases and differentiations, domain mappings, communication, etc.

There are two main goals of this work:

- Explore the DG method for solving the GR and hydrodynamics equations simultaneously. As we will see below, the equations of the two theories take fundamentally different forms (conservative vs. non-conservative), so it is not a priori obvious that solving them on the same grid with the same technique will work.
- Explore the use of conforming grids for BH and NS applications. In this case, cubical elements are mapped to match the spherical geometry of an excision boundary inside the BH, or the spherical boundary at large

distances from the BH or NS.

This paper is organized as follows. In Sec. 2.2 we summarize the formulation of the DG method. In Sec. 2.3 we discuss our use of geometrically adapted grids, "manual" mesh refinement, and limiters. We detail the GR-hydro equations and the numerical algorithms in Sec. 2.4. We validate the code by performing standard test cases shown in Sec. 2.5. In Sec. 2.6 we present results for neutron star evolutions, before concluding in Sec. 2.7.

2.2 Discontinuous Galerkin formulation

Our code uses a DG method to solve conservation laws in curved spacetimes, and also to evolve the spacetime itself. We express the spacetime metric $g_{\mu\nu}$ using the standard 3+1 form

$$\begin{aligned} ds^2 &= g_{\mu\nu} dx^\mu dx^\nu \\ &= -\alpha^2 dt^2 + \gamma_{ab}(dx^a + \beta^a dt)(dx^b + \beta^b dt), \end{aligned} \tag{2.1}$$

where α is the lapse function, β^a is the shift vector, and γ_{ab} is the spatial metric (with determinant γ) on hypersurfaces of constant time t. Our index convention is as follows: Greek indices (μ,ν,...) refer to spacetime components and range from 0 to d in d spatial dimensions. Latin indices (a,b,...) refer to spatial components and range from 1 to d. Repeated indices are summed over. We use units where $G, c = 1$. We additionally set $M_\odot = 1$ for our neutron star simulations in Sec. 2.6.

A conservation law in this curved spacetime can be written as a 4-divergence $\nabla_\mu F^\mu = s$, where ∇_μ is the covariant derivative, F^μ encodes the conserved

quantity $u = F^0$ and its corresponding spatial flux vector $F^a(u)$, and s is the source term for u. Separating the time and spatial components gives the more common form

$$\frac{1}{\sqrt{\gamma}}\partial_t(\sqrt{\gamma}u) + \frac{1}{\sqrt{\gamma}}\partial_a(\sqrt{\gamma}F^a) = s, \tag{2.2}$$

which we aim to solve for $u(x^a, t)$ given initial conditions $u(x^a, 0)$ and suitable boundary conditions. When solving a system of conservation laws (e.g. for mass, energy and momentum in hydrodynamics), u is a vector of several conserved quantities and F^a is a vector of flux vectors.

We numerically solve the conservation law [1] using a strong-form, nodal DG method on square/cube elements. In this section we summarize the method, and give the specifics of our implementation. We follow the formulation given by Teukolsky [28], where greater detail may be found.

2.2.1 Representing the solution

We divide the spatial domain into K elements. On each element we expand the quantities u, F^a, s, etc. over a set of polynomial basis functions ϕ_i, e.g.

$$u(\mathbf{x}, t) = \sum_i u_i(t)\phi_i(\mathbf{x}). \tag{2.3}$$

We adopt a nodal representation: we evolve the values $u_i(t) = u(\mathbf{x}_i, t)$ at the nodes $\mathbf{x}_i$ of the computational grid, and the ϕ_i interpolate between these grid nodes. Below we provide definitions; more detailed discussion can be found in textbooks [35, 36].

[1] The conservation law is discretized (see Sec. 2.2.2) and solved for a numerical approximation u_h to the true solution u. We do not make the distinction between u_h and u.

The partition into elements is chosen so that each element is a mapping of a topologically simple reference element: a cube (in 3D), square (in 2D), or interval (in 1D). The mapping from the reference element coordinates $\bar{\mathbf{x}}$ to the computational coordinates $\mathbf{x} = \mathbf{x}(\bar{\mathbf{x}})$ of each element has a Jacobian matrix

$$\mathbf{J} = \frac{\partial x^a}{\partial x^{\bar{a}}} \tag{2.4}$$

and Jacobian $J = \det \mathbf{J}$.

In each direction, the $x^{\bar{a}}$ coordinate spans the interval $[-1, 1]$ on which we place the nodes $x_i^{\bar{a}}$ of a Gauss-Legendre-Lobatto quadrature. The 1D Lagrange interpolation polynomials $\ell_j(x^{\bar{a}})$ are defined on these nodes, and satisfy $\ell_j(x_i^{\bar{a}}) = \delta_{ij}$. In the full d dimensions, we obtain the the grid nodes $\bar{\mathbf{x}}_i$ by the direct product of the $x^{\bar{a}}$, and the basis functions by tensor product of the $\ell_i(x^{\bar{a}})$, e.g. (with some abuse of indices to indicate the tensor product)

$$\phi_i(\bar{\mathbf{x}}) \to \phi_{ijk}(\bar{\mathbf{x}}) = \ell_i(x^{\bar{1}})\ell_j(x^{\bar{2}})\ell_k(x^{\bar{3}}). \tag{2.5}$$

With N_p nodes in the $x^{\bar{a}}$ coordinate, $\ell_i(x^{\bar{a}})$ is a polynomial of degree $N = N_p - 1$. When N is the same in all directions, we say we have an N^{th}-order DG element.

We will occasionally use a modal representation in which the solution is expanded over a basis of orthonormal polynomials, e.g.

$$u(\bar{\mathbf{x}}, t) = \sum_i \hat{u}_i(t)\psi_i(\bar{\mathbf{x}}). \tag{2.6}$$

The $\hat{u}_i$ are the expansion weights and the ψ_i are obtained from the tensor product of 1D basis functions, the Legendre polynomials P_l. The Vandermonde matrix $\mathcal{V}_{ij} = P_j(x_i)$ gives the transformation between the nodal and modal representations,

$$u_i = \sum_j \mathcal{V}_{ij}\hat{u}_j. \tag{2.7}$$

2.2.2 DG for conservation laws

We impose the conservation law (2.2) in a Galerkin sense, by integrating the equation against each basis function ϕ_i on each element. We integrate over proper volume $\sqrt{\gamma}d^3x$, giving

$$\int \left[\partial_t(\sqrt{\gamma}u) + \partial_a(\sqrt{\gamma}F^a) - \sqrt{\gamma}s\right] \phi_i(\mathbf{x})d^3x = 0. \tag{2.8}$$

To establish the flow of information between neighboring elements, we integrate the flux divergence term by parts, and apply Gauss's law to the resulting boundary term (see [28]),

$$\begin{aligned}\int \partial_a(\sqrt{\gamma}F^a)\phi_i(\mathbf{x})d^3x = &-\int \sqrt{\gamma}F^a\partial_a\phi_i(\mathbf{x})d^3x \\ &+ \oint F^a n_a \phi_i(\mathbf{x})d^2\Sigma.\end{aligned} \tag{2.9}$$

Here $d^2\Sigma$ is the proper surface element on the element's boundary, and n_a is the outward-directed unit normal.

The flux vector F^a is double-valued on the boundary because of the local (i.e. discontinuous) nature of the solution. For the scheme to be conservative, a unique flux must cross the boundary between adjacent elements. This value, the so-called *numerical* flux F^{a*}, is computed from the data on both sides of the boundary, and serves to connect the solution between elements across the domain. Computing F^{a*} requires the communication of boundary data between nearest-neighbor elements only. We substitute $F^a \to F^{a*}$ in the last term of (2.9).

We now undo the integration by parts, using (2.9) to eliminate the second (i.e. $\partial_a\phi_i$) term (this time, however, we do not substitute in the numerical flux), and

obtain

$$\int \partial_a(\sqrt{\gamma}F^a)\phi_i(\mathbf{x})d^3x \to \int \partial_a(\sqrt{\gamma}F^a)\phi_i(\mathbf{x})d^3x + \oint (F^{a*} - F^a)n_a\phi_i(\mathbf{x})d^2\Sigma \tag{2.10}$$

Defining $F = (F^{a*} - F^a)n_a$ and putting the terms back together, we get the DG equation in integral form,

$$\int \left[\partial_t(\sqrt{\gamma}u) + \partial_a(\sqrt{\gamma}F^a) - \sqrt{\gamma}s\right]\phi_i(\mathbf{x})d^3x = -\oint F\phi_i(\mathbf{x})d^2\Sigma. \tag{2.11}$$

To obtain a form more suitable for computation, we first expand each term of (2.11) using the nodal expansion (2.3). We rewrite the integrals in the reference coordinates $\bar{\mathbf{x}}$, where $d^3x \to Jd^3\bar{x}$ and $d^2\Sigma \to \sqrt{^{(2)}\gamma}d^2\bar{x}$, with $^{(2)}\gamma$ the determinant of 2D metric induced by γ_{ab} on the surface. Finally, we evaluate the integrals with a Gauss-Lobatto quadrature rule. By using the grid nodes $\bar{\mathbf{x}}_i$ as the quadrature nodes we can use the identity $\ell_i(x_j^{\bar{1}}) = \delta_{ij}$ to greatly simplify the scheme. The tradeoff is that the quadrature rule will not be exact — especially when a non-trivial Jacobian J multiplies the integrand — and this can lead to aliasing and introduce instabilities that require filtering.

Finally, after simplifying the geometric factors on the boundary terms (see [28], Appendix A) and dividing through by common factors, we arrive at the

evolution equation,

$$\begin{aligned}
\frac{d(\sqrt{\gamma}u)_{ijk}}{dt} + \Big[\frac{\partial x^{\bar{1}}}{\partial x^a}\Big|_{ijk} \sum_l D^{\bar{1}}_{il} \left(\sqrt{\gamma}F^a\right)_{ljk} + \frac{\partial x^{\bar{2}}}{\partial x^a}\Big|_{ijk} \sum_m D^{\bar{2}}_{jm} \left(\sqrt{\gamma}F^a\right)_{imk} \\
+ \frac{\partial x^{\bar{3}}}{\partial x^a}\Big|_{ijk} \sum_n D^{\bar{3}}_{kn} \left(\sqrt{\gamma}F^a\right)_{ijn} \Big] - (\sqrt{\gamma}s)_{ijk} \\
= -\frac{\sqrt{\gamma^{\bar{1}\bar{1}}_{Njk}}}{w_N}(\sqrt{\gamma}F)_{Njk}\delta_{iN} + \frac{\sqrt{\gamma^{\bar{1}\bar{1}}_{0jk}}}{w_0}(\sqrt{\gamma}F)_{0jk}\delta_{i0} \\
- \frac{\sqrt{\gamma^{\bar{2}\bar{2}}_{iNk}}}{w_N}(\sqrt{\gamma}F)_{iNk}\delta_{jN} + \frac{\sqrt{\gamma^{\bar{2}\bar{2}}_{i0k}}}{w_0}(\sqrt{\gamma}F)_{i0k}\delta_{j0} \\
- \frac{\sqrt{\gamma^{\bar{3}\bar{3}}_{ijN}}}{w_N}(\sqrt{\gamma}F)_{ijN}\delta_{kN} + \frac{\sqrt{\gamma^{\bar{3}\bar{3}}_{ij0}}}{w_0}(\sqrt{\gamma}F)_{ij0}\delta_{k0}.
\end{aligned} \tag{2.12}$$

Here $D^{\bar{1}}_{il}$ is the differentiation matrix along the $x^{\bar{1}}$ direction, given by

$$D^{\bar{1}}_{il} = \partial_{\bar{1}} \ell_l(x^{\bar{1}})\big|_i. \tag{2.13}$$

Although our derivation and resulting evolution equation (2.12) are given for the 3D case, restricting to a lower-dimensional problem is straightforward. For instance, in a 2D problem, the 3$^{\text{rd}}$ tensor-product index on each term is dropped (e.g. $u_{ijk} \to u_{ij}$), as are the "$\bar{3}$" terms of the flux derivative and flux boundary terms.

2.2.3 DG for the Einstein equations

We use a formulation of the Einstein equations, detailed in the next section, that cannot be written in conservative form. These equations are instead in hyperbolic form,

$$\partial_t u + A^a \partial_a u = s, \tag{2.14}$$

where the matrices A^a and vector s may be functions of u, but not of derivatives of u. To obtain the corresponding DG algorithm, we again multiply by a basis function ϕ_i and integrate over the proper volume element. We integrate by parts twice, substituting the numerical flux after the first integration, to obtain the integral form akin to (2.11),

$$\begin{aligned} \int \left[\partial_t u + A^a \partial_a u - s\right] \phi_i(\mathbf{x}) \sqrt{\gamma} d^3x = \\ - \oint \left[(A^a u)^* - (A^a u)\right] n_a \phi_i(\mathbf{x}) d^2\Sigma. \end{aligned} \tag{2.15}$$

Evaluating the integrals as before, we find

$$\begin{aligned} \frac{du_{ijk}}{dt} + A^a_{ijk} \left[\frac{\partial x^{\bar{1}}}{\partial x^a}\Big|_{ijk} \sum_l D^{\bar{1}}_{il} u_{ljk} + \ldots\right] - s_{ijk} \\ = -\frac{\sqrt{\gamma^{\bar{1}\bar{1}}_{Njk}}}{w_N} \left([(A^a u)^* - (A^a u)] n_a\right)_{Njk} \delta_{iN} + \ldots . \end{aligned} \tag{2.16}$$

This result is analogous to (2.12), so we have reproduced here only one term of each type.

Comparison with SpEC's penalty spectral algorithm

SpEC solves the Einstein equations using a multi-domain penalty pseudospectral method (see, e.g. [37]). This method is closely related to our nodal DG method: the DG boundary term represents a particular type of penalty term, one chosen to enforce conservation via the numerical flux. Indeed, the spectral method in SpEC takes the form of (2.16) with an upwind flux, differing only in the numerical prefactor multiplying the boundary flux term. Where our DG method has a prefactor of $1/w_N$ arising from the Legendre Gauss-Lobatto quadrature rule, the SpEC penalty method instead uses the prefactor derived for stability of a Chebyshev penalty method.

The similarity between the methods enables the techniques used to evolve the spacetime in SpEC to transfer well to our DG code. In numerical experiments, we observe that the DG code exhibits a higher order of convergence under h-refinement (DG: order $N+1$; SpEC: order N), which, empirically, we attribute to the difference in the boundary term prefactor.

2.3 Approach to grid structure, mesh refinement, and limiting

Previous applications of the DG method to problems in astrophysics have used uniform grids [20, 22, 23]. We adopt a different philosophy and take advantage of the DG method's geometric flexibility to tailor our grid to the problem being solved. We discuss here our choice of grid structures, mesh refinement, and limiting.

2.3.1 Grid structure and mesh refinement

It is well known that constructing the computational grid to mirror the underlying symmetries of the problem can greatly increase the accuracy of a numerical method. In astrophysical problems, the symmetry is often spherical, reflecting the gravitational potential of a star or BH. The use of a conforming spherical grid comes with a loss of generality: the grid must remain centered on the astrophysical body. This is especially important when taking advantage of the spherical grid to excise the singularity inside a BH. With the use of moving grids [38] and control systems [31], however, conforming grids can be successfully used in simulations of binary mergers.

The evolutions shown in this paper make use of two basic types of grid structures.

1. **Cartesian grids**, obtained by a straightforward affine mapping (a translation and a scaling) of the reference element. These grids are used in several standard test problems.
2. **Cubed spheres**, obtained by conforming several cube-like elements to the surface of a sphere, using mappings detailed in App. 2.A and illustrated in, e.g., Fig. 2.3. These grids are used for problems with spherical geometry such as single BH or NS evolutions. The cubed sphere may be a hollow spherical shell, allowing for excision of the spacetime region inside the BH's event horizon, or a filled ball, for evolution of the full NS. As we consider isolated systems at rest, moving grids are not needed.

To further take advantage of the geometric flexibility of the DG method, we use hp-adaptivity to vary the spatial resolution across the simulation domain. The AMR infrastructure of SpEC is designed to operate under a restricted set of conditions, and is not general enough to handle the shocks and surfaces encountered in the hydrodynamic evolutions. We instead manually set up "fixed" mesh refinement, where we initially assign the size and order of the DG elements based on a priori knowledge of the solution. When constructing the grid for a NS evolution, for instance, we use larger, higher-N elements inside the star, and smaller, lower-N elements at the surface.

The SpEC framework, designed and optimized for evolutions on $O(10\text{–}100)$ spectral elements, scales poorly to the large number of elements often used in DG simulations. In spite of several improvements to the datastructures, we find

that the memory usage and parallelism become inefficient when the domain approaches $O(10^4)$ elements. We therefore stay below this threshold in most of the tests presented. This restriction on the maximum number of elements would be problematic for a typical DG implementation, in which the domain is split into a regular grid of many small cubical elements. As we instead conform our grids to the problem geometry, we obtain satisfactory accuracy using many fewer elements.

2.3.2 Limiting

In DG elements containing a shock or surface in the fluid, the solution is susceptible to spurious oscillations (Gibbs phenomenon) and overshoots. If unaddressed, these overshoots can lead to unphysical fluid states (e.g. negative densities) in which the fluid equations are no longer solvable. A limiter controls these oscillations and overshoots by modifying the solution in a way that is conservative and (ideally) does not overly degrade the accuracy of the method.

Typical DG implementations apply the limiter agnostically across the uniform grid. A "troubled-cell" detector identifies cells containing spurious oscillations and applies the limiter to those cells. While this is the most general way to set up the problem, finding a general troubled-cell detector that does not mis-identify smooth extrema in the solution can be challenging. This can lead to problems, such as a smearing out of the density maximum at the center of a star.

In the context of an hp-adaptive DG method, however, the AMR criteria can also be used to inform the troubled-cell detector. When the solution is not smooth (i.e. the modal coefficients do not fall off rapidly enough) the AMR will reduce

the order and trigger h-refinement. High-order elements, by construction, have smooth solutions and do not require limiting. In our manually-refined grid, we apply the limiter only to elements with $N \leq 2$ in any spatial direction.

While our choices of grid setup and limiter application are not fully general, they are representative of the result of a more general AMR DG code. Our results are an exploration and will serve to inform the choices made in a future AMR update to SpECTRE (a new DG code mentioned in Sec. 2.1).

2.4 Evolution of GR and hydro

2.4.1 Spacetime geometry

Generalized harmonic equations

We evolve the spacetime geometry using the generalized harmonic formulation of Einstein's equations [39, 40]. We use a first-order representation of the system [41] in which the evolved variables are the spacetime metric $g_{\mu\nu}$, its spatial first derivatives $\Phi_{i\mu\nu} = \partial_i g_{\mu\nu}$, and its first derivative $\Pi_{\mu\nu} = -t^\sigma \partial_\sigma g_{\mu\nu}$ along the (timelike, future-directed) normal t^σ to the constant-t hypersurface. The complete equations for $\partial_t g_{\mu\nu}$, $\partial_t \Phi_{i\mu\nu}$, and $\partial_t \Pi_{\mu\nu}$ [2] in a vacuum spacetime can be found in [41]; when coupling the spacetime to matter, we add the source term

$$\partial_t \Pi_{\mu\nu} = \Big(\text{vacuum terms}\Big) - 2\alpha \left(T_{\mu\nu} - \frac{1}{2} g_{\mu\nu} T^{\rho\sigma} g_{\rho\sigma}\right). \tag{2.17}$$

[2] Where we use $g_{\mu\nu}$, the cited papers use $\psi_{\mu\nu}$ to denote the spacetime metric. The symbols for the metric derivatives are unchanged.

The DG method for this system of equations takes the form (2.16). The characteristic variables and speeds for the system, used in the upwind numerical flux shown below, are also given in [41].

For the cases we present in this paper, the natural coordinates of the initial data are well-suited to prolonged time-evolution. The generalized harmonic gauge function H_σ, which specifies the coordinates, is therefore independent of time. Its precise form will depend on the data being evolved. The constraint-damping parameters γ_0 and γ_2, which constrain the evolution of the coordinates and the growth of short-wavelength perturbations respectively, are also problem-dependent. Following [41], we fix the parameter γ_1 to -1 to obtain a symmetric hyperbolic system and avoid the formation of shocks.

Upwind flux

As the solutions to the Einstein equations are smooth, we use an upwind numerical flux, which sets the flux through the boundary according to the propagation direction of each characteristic variable. The characteristic decomposition of the system is given by

$$A^a n_a u = S \Lambda S^{-1} u, \tag{2.18}$$

where S diagonalizes the product $A^a n_a$, i.e. the i^{th} column of S is the right eigenvector of $A^a n_a$, with eigenvalue λ_i. Physically, the $S^{-1}u$ are the characteristic variables of the system, and λ_i are the associated propagation speeds with respect to the normal n_a. The diagonal matrix $\Lambda = \text{diag}(\lambda_1, ..., \lambda_n)$ holds these eigenvalues, and can be separated by the sign of the eigenvalues, $\Lambda = \Lambda^+ + \Lambda^-$. At a boundary with two edge states u^{L}, u^{R} and a normal n_a directed towards the

R state, the upwind numerical flux takes the form

$$(A^a n_a u)^{\text{upwind}} = S\left(\Lambda^+ S^{-1} u^{\text{L}} + \Lambda^- S^{-1} u^{\text{R}}\right), \tag{2.19}$$

so that characteristic variables propagating left-to-right (in the direction of n_a, with $\lambda_i > 0$) are set from the u^{L} state, whereas variables propagating right-to-left (with $\lambda_i < 0$) are set from u^{R}.

2.4.2 Hydrodynamics

Relativistic fluid equations

We treat the matter as a perfect fluid. Its stress-energy tensor takes the form

$$T_{\mu\nu} = \rho h u_\mu u_\nu + p g_{\mu\nu}, \tag{2.20}$$

where ρ is the fluid's rest-frame mass density, p the pressure, and $h = 1 + \epsilon + p/\rho$ the relativistic specific enthalpy, with ϵ the specific internal energy density. From the fluid's 4-velocity $u^\mu = W(1, v^i)$, we define the lower 3-velocity components $v_i = \gamma_{ij} v^j$ and the Lorentz factor $W = \alpha u^0 = 1/\sqrt{1 - v_i v^i}$. An equation of state (EOS) relates p, ρ, and ϵ; we use an ideal gas EOS $p = (\Gamma - 1)\rho\epsilon$, with Γ the adiabatic index. In the absence of shocks, this is equivalent to a polytropic EOS where $p = K\rho^\Gamma$, with K some constant.

The dynamics of the fluid are governed by the relativistic Euler equations. We use the "València" form of these equations [42], with conserved quantities $\{D, S_i, \tau\}$: the mass-energy density, momentum density, and internal energy,

respectively, as measured by a generalized Eulerian observer. These are given by

$$\sqrt{\gamma}u = \begin{pmatrix} \tilde{D} \\ \tilde{S}_i \\ \tilde{\tau} \end{pmatrix} = \begin{pmatrix} \sqrt{\gamma}W\rho \\ \sqrt{\gamma}W^2\rho h v_i \\ \sqrt{\gamma}\left(W^2\rho h - p - W\rho\right) \end{pmatrix}. \tag{2.21}$$

The corresponding flux vector and source term are

$$\sqrt{\gamma}F^a = \begin{pmatrix} \tilde{D}v^a_{\rm tr} \\ \tilde{S}_i v^a_{\rm tr} + \sqrt{\gamma}\alpha p \delta^a_i \\ \tilde{\tau}v^a_{\rm tr} + \sqrt{\gamma}\alpha p v^a \end{pmatrix} \tag{2.22}$$

$$\sqrt{\gamma}s = \begin{pmatrix} 0 \\ (\alpha/2)\tilde{S}^{lm}\partial_i\gamma_{lm} + \tilde{S}_k\partial_i\beta^k - \tilde{E}\partial_i\alpha \\ \alpha\tilde{S}^{lm}K_{lm} - \tilde{S}^l\partial_l\alpha \end{pmatrix}. \tag{2.23}$$

Here $v^a_{\rm tr} = \alpha v^a - \beta^a = u^a/u^0$ is the transport velocity relative to the coordinates, S^{lm} and E are components of the stress-energy,

$$\tilde{S}^{lm} = \gamma^{l\mu}\gamma^{m\nu}T_{\mu\nu} = \sqrt{\gamma}\rho h W^2 v^l v^m + \sqrt{\gamma}p\gamma^{lm} \tag{2.24}$$

$$\tilde{E} = n^\mu n^\nu T_{\mu\nu} = \sqrt{\gamma}\rho h W^2 - \sqrt{\gamma}p, \tag{2.25}$$

and K_{lm} is the usual extrinsic curvature to the constant-t hypersurface. The system of equations is evolved according to the discretized form (2.12). The characteristic speeds, used in the numerical fluxes shown below, are given in [43].

Solving for the primitive variables $\{\rho, v_i, \epsilon\}$ from $\{D, S_i, \tau\}$ requires root finding, and may additionally require "atmosphere fixing" in regions of low density where the solve may be numerically poorly behaved. In the test problems of Sec. 2.5, fixing is not needed; for the NS evolutions of Sec. 2.6 we follow the inversion and fixing procedure of [44], App. C.

Numerical fluxes

For the fluid, we use a numerical flux chosen to approximately solve the Riemann problem corresponding to the discontinuity between elements. As before, we label the two states at the boundary as u^{L}, u^{R}, and the normal n_a points towards the R state. A popular choice of numerical flux, because of its robustness and simplicity, is the local Lax-Friedrichs (LLF) flux. This flux is computed according to

$$(F^{a*}n_a)^{\mathrm{LLF}} = \frac{F^a(u^{\mathrm{L}})n_a + F^a(u^{\mathrm{R}})n_a}{2} - \frac{C}{2}\left(u^{\mathrm{R}} - u^{\mathrm{L}}\right), \tag{2.26}$$

where $C = \max(|\lambda_i(u^{\mathrm{L}})|, |\lambda_i(u^{\mathrm{R}})|)$ is the largest speed across the interface. The speeds λ_i are again the eigenvalues of the flux Jacobian (see the upwind flux discussion above, with $A^a \to \partial F^a/\partial u$). We maximize over the λ_i on both sides of the interface, but independently at each interface grid point.

A more sophisticated numerical flux, which includes an approximate treatment of the system's underlying wave structure, is given by Harten, Lax, and van Leer (HLL) [45, 46],

$$\begin{aligned}(F^{a*}n_a)^{\mathrm{HLL}} =& \frac{c_{\max}F^a(u^{\mathrm{L}})n_a + c_{\min}F^a(u^{\mathrm{R}})n_a}{c_{\max} - c_{\min}} \\ &- \frac{c_{\max}c_{\min}}{c_{\max} - c_{\min}}\left(u^{\mathrm{R}} - u^{\mathrm{L}}\right).\end{aligned} \tag{2.27}$$

Here $c_{\min}$, $c_{\max}$ are estimates for the fastest left- and right-moving signal speeds, respectively. We use the simple estimates [47], computed point-wise,

$$\begin{aligned}c_{\min} &= \min\left(\lambda_i(u^{\mathrm{L}}), \lambda_i(u^{\mathrm{R}}), 0\right) \\ c_{\max} &= \max\left(\lambda_i(u^{\mathrm{L}}), \lambda_i(u^{\mathrm{R}}), 0\right).\end{aligned} \tag{2.28}$$

Note that the HLL flux reduces to upwinding when all λ_i share the same sign, i.e. all characteristic variables are propagating in the same direction.

We find that the LLF and HLL fluxes give very similar results in most of the cases we tested (see Sec. 2.5.2 for one exception), and conclude that the use of an approximate solution to the Riemann problem does not introduce significant error in these problems. The results presented in this paper are computed using the HLL flux.

Limiters

In this work we use and compare two limiters. The first is the simple, but also low-order, minmod-based slope limiter [35, 48], which we will refer to simply as minmod. This limiter computes three different slope estimates for the element, using the local gradient and differences between neighboring element means. Taking the 1D case as example, the estimates are

$$a_1 = \frac{\partial u^k}{\partial x}, \quad a_2 = \frac{\bar{u}^{k+1} - \bar{u}^k}{h/2}, \quad a_3 = \frac{\bar{u}^k - \bar{u}^{k-1}}{h/2}, \tag{2.29}$$

where u^k is the solution on the k^{th} element, $\bar{u}^k$ is the mean of u^k over the element, and h is the width of the element. The limiter selects the estimate that is closest to 0 (or 0, if the three estimates differ in sign). If the selected estimate is not the original slope a_1, the limiter activates by setting the slope to the selected estimate (or 0) and discarding any higher-order terms in the approximation. In higher dimensions, the limiter is applied to each dimension in turn.

On higher-order elements with $N \geq 2$, we use the generalization of minmod described in [35]. The "total variation bound" (TVB) generalization, which sets a scale below which oscillations are tolerated, is not robust at star surfaces, so we use the standard minmod. We find that in more than one dimension, the limited solution may occasionally correspond a non-physical state. When this occurs, we

further reduce the slope until the following are satisfied throughout the element: $\min(D) > \sqrt{\gamma}\rho_{\text{atmo}}$, $\min(\tau) > 0$, and $S^2 < \tau(\tau + 2D)$.

The second limiter we consider is that of Moe *et al*. [49], henceforth MRS. This limiter acts by scaling the conserved variables u in an element about their means $\bar{u}$ (averaged over the element),

$$u \to \bar{u} + \theta(u - \bar{u}), \tag{2.30}$$

with $\theta \in [0, 1]$ determined from analysis of the minima and maxima of the solution in the immediate neighborhood of the element. Because the components of u can differ by a few orders of magnitude, we modify the MRS prescription so that the smoothness parameter $\alpha(h)$ in the computation of θ is relative. [3] We find the value $\alpha(h) = 10h^{3/2}$ performs well on many different test problems; all cases presented in this paper use this parameter value.

We obtain best results when computing θ from the primitive variables, as MRS recommend. However, care must be taken when computing the primitive variables, as the fluid state may be unphysical until limited. We "pre-limit" by applying an additional scaling of the form (2.30) to the conserved variables. The steps below restore a physical state and ensure the inversion procedure is well-posed:

1. if $\min(D) < \sqrt{\gamma}\rho_{\text{atmo}}$ or $\min(\tau) < 0$, scale to fix these violations.
2. if $S_i S^i > \tau(\tau + 2D)$ at any grid point, scale to fix this violation. This requires solving a quadratic equation for θ.
3. if the inversion to primitive variables encounters any of the errors outlined in [44], Appendix C, (this is rare), scale again with $\theta = 1/2$.

[3] Where MRS use $\bar{u} + \alpha(h)$, e.g. in their equations (6.4), (6.5), we use $\bar{u} + |\bar{u}|\alpha(h)$.

This procedure is conservative by construction, and we find it to be robust. After this "pre-limiting" step, we compute the primitive variables and limit according to the MRS prescription.

We apply the limiter to the hydro variables at the end of each timestepper substep. Unlike traditional DG implementations, we may not apply the limiter to every element, choosing instead to mimic an AMR scheme in which high-order elements are known to be smooth. The use of more complex, higher-order, limiters, e.g. sub-cell methods [20, 22] or the compact-stencil WENO [14] and HWENO [15] limiters, will be the subject of future investigation.

2.4.3 Combined GR-hydro system

For self-consistent NS evolutions the GH and hydro systems of equations are each treated as described above, and are evolved in parallel. The two systems couple via their respective source terms and the geometry terms in the hydro flux $F^a(u)$. We compute the characteristic speeds independently for each system, leaving out the cross-coupling arising from the off-diagonal $\partial F^a_{\text{hydro}}/\partial u_{\text{GH}}$ flux Jacobian terms. When the hydro variables require limiting, the limiter is applied to the hydro variables only, and the spacetime variables are left unmodified.

2.4.4 Filtering

The use of inexact quadratures in Sec. 2.2.2 to obtain an efficient scheme may result in instabilities due to aliasing. Where these instabilities exist, we address them by filtering the higher modes in the solution's modal representation. We

use an exponential filter, e.g. in 1D

$$\hat{u}_i \longrightarrow F(i)\hat{u}_i = \exp\left(-\alpha(i/N)^s\right)\hat{u}_i, \tag{2.31}$$

where α controls the strength of the filter's effect, and s is an even integer controlling how many modes are affected. In $d > 1$ dimensions, we take advantage of the tensor-product basis to apply the filter dimension-by-dimension; this gives d exponentials. We apply the filter at the end of each complete timestep to the components of u and on the elements that show instability.

2.4.5 Timestepping

We use the 3$^{\text{rd}}$-order strong stability-preserving Runge Kutta scheme of [50] for the time integration. Given the solution u^n at time t^n, the solution u^{n+1} at time $t^{n+1} = t^n + \Delta t$ is computed as

$$\begin{aligned} u^{(1)} &= u^n + \Delta t L(u^n) \\ u^{(2)} &= \frac{3}{4}u^n + \frac{1}{4}\left[u^{(1)} + \Delta t L(u^{(1)})\right] \\ u^{n+1} &= \frac{1}{3}u^n + \frac{2}{3}\left[u^{(2)} + \Delta t L(u^{(2)})\right] \end{aligned} \tag{2.32}$$

Here $L(u) = du/dt$ is computed from expressions (2.12) for the hydro variables or (2.16) for the GR variables.

In all cases presented, the initial $t = 0$ data is computed by pointwise evaluation of a known state. The limiter is applied to the initial data and at the end of every subsequent substep. Filtering is done at the end of full timesteps.

2.5 Code tests

In this section we present a selection of benchmark tests that we use to validate our implementation of the DG method within SpEC.

We first show tests of vacuum spacetime evolution. From a family of gauge wave evolutions at varying resolutions, we verify that the method converges to the exact solution at the expected rate. Next, by evolving a Kerr (i.e. isolated and spinning) black hole over long timescales, we show the stability of the algorithm.

We then show our tests of the hydrodynamics implementation. We again verify the convergence rate of the errors, now with a generalized Bondi problem in which the fluid undergoes spherically symmetric accretion onto a Schwarzschild black hole. This test verifies the fluid equations as well as the sourcing of the fluid by the spacetime curvature. We then show standard shock tests in 1D and 2D, comparing the effectiveness of the implemented limiters.

In these tests, whenever possible, we compare the numerical solution to an exact solution, and we use their difference as an error measure. We report a normalized error $\mathrm{err}[X]$ in a quantity X, defined as

$$\mathrm{err}[X] = \|X - X_{\mathrm{exact}}\| \big/ \|X_{\mathrm{exact}}\|. \tag{2.33}$$

Here $\|X\|$ is the square root of the L^2-norm, evaluated pointwise by direction summation over every node of the computational grid,

$$\|X\|^2 = \frac{1}{N_{\mathrm{nodes}}} \sum_{i=0}^{N_{\mathrm{nodes}}} X_i^2. \tag{2.34}$$

When X is a vector or tensor quantity, we compute the norm of the summed components $\|X_a\|^2 = \|X_0 + X_1 + ...\|^2$ rather than the physical norm $X_a X^a$. When

$X_{\text{exact}} = 0$ so that we cannot define the normalized error, we instead use $\|X\|$ as our error measure.

2.5.1 Spacetime tests

Gauge wave test

The spacetime of the "apples to apples" gauge wave test [51], obtained via a nonlinear, plane-wave transformation of Minkowski space, takes the form

$$ds^2 = -(1+a)dt^2 + (1+a)dx^2 + dy^2 + dz^2, \tag{2.35}$$

with

$$a = A\sin[2\pi(x-t)]. \tag{2.36}$$

We show results for a wave of amplitude $A = 0.1$ on a unit-cube domain with extents $[0,1]^3$. As the gauge wave is a perturbation of flat space, the generalized harmonic gauge function H_σ is zero. We set the constraint-damping parameters $(\gamma_0, \gamma_1, \gamma_2)$ to $(1, -1, 1)$, respectively, values that give stable evolutions over long timescales (up to at least $t_{\text{fin}} = 1000$, or 1000 crossing times). For the convergence study, however, we measure the error in the spacetime metric $g_{\mu\nu}$ at a final time $t_{\text{fin}} = 10$, after evolution with timesteps of size $\Delta t = 10^{-4}$. This timestep corresponds to $\Delta t/\Delta x_{\min} \simeq 0.074$ for the highest-resolution case in the convergence study ($K = 128$, $N = 4$).

We show in Fig. 2.1 the convergence under h-refinement, measured for elements of order $N = 2, 3, 4$. As a base resolution we partition the unit-cube domain into 16 elements along the x direction; we h-refine by splitting each element along x, reducing the element's width h in half each time. We do not

split in y or z — the anisotropic refinement is chosen to match the x-only dependence in the problem. For each order N of the DG method, we compare our measurements to the theoretical scaling of the error (see, for instance, [35]),

$$\mathrm{err}[g_{\mu\nu}] \leq Ch^{N+1} \propto 1/K^{N+1}, \tag{2.37}$$

for some constant C. We find excellent agreement between the measured and expected convergence rates. The highest-resolution case ($K = 128$ and $N = 4$) has slightly larger error, having reached the roundoff level error in the derivatives of the spacetime.

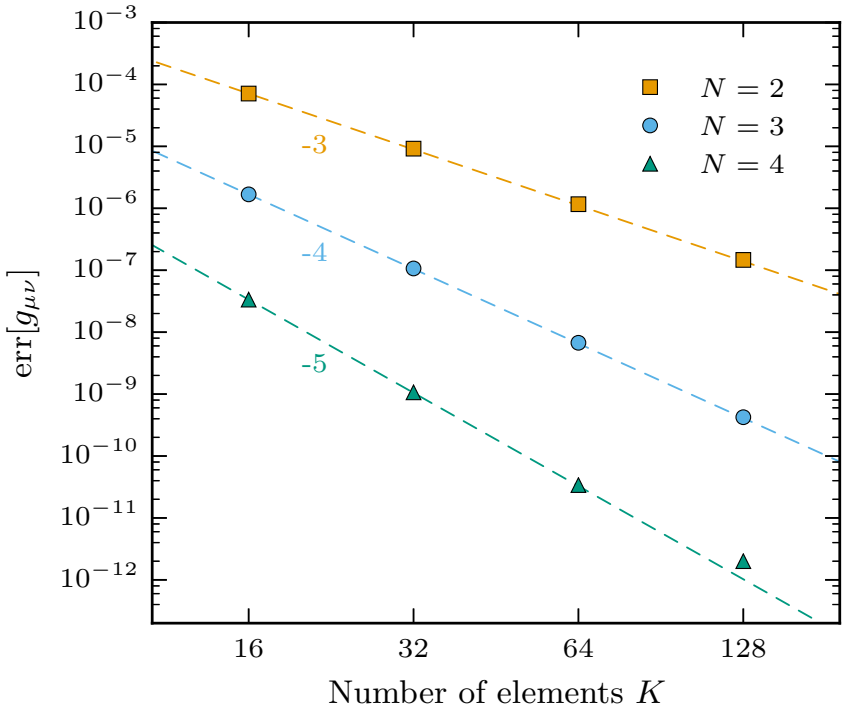

Figure 2.1: The error in $g_{\mu\nu}$ as a function of the number of elements (h-refinement) for the gauge wave test of Einstein's equations. The symbols indicate the measured error norms for methods of order $N = \{2, 3, 4\}$. The dashed lines, normalized to the $K = 16$ data, indicate the expected error scaling for third, fourth, and fifth order convergence.

In Fig. 2.2 we show the convergence under p-refinement, obtained by increasing the order N of the DG method while maintaining the base resolution of

16 elements. We expect the errors to decrease exponentially with the order N, and recover this behavior in our measurements. This result demonstrates the "spectral" convergence of the DG method for smooth solutions.

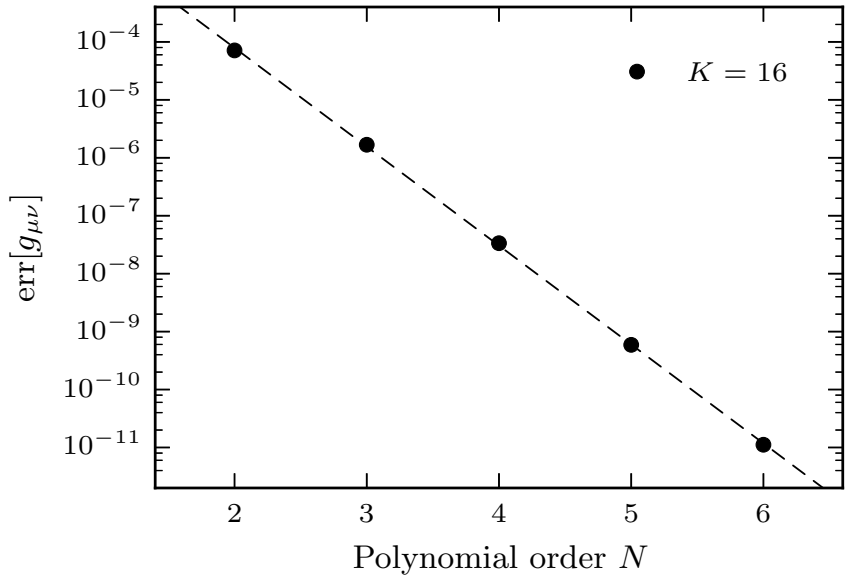

Figure 2.2: The error in $g_{\mu\nu}$ as a function of the order of approximation (p-refinement) for the gauge wave test of Einstein's equations. The number of elements is fixed at $K = 16$. The dots indicate the measured errors; the dashed line is a fit demonstrating the exponential decrease in error with N.

Kerr black hole

We next evolve the spacetime of a Kerr black hole, described by the Kerr metric in Kerr-Schild coordinates [52]. The black hole has spin $\vec{a} = (0.1, 0.2, 0.3)M_{\mathrm{BH}}$ with magnitude $a \approx 0.374M_{\mathrm{BH}}$, not aligned with any grid symmetries. We use units where $M_{\mathrm{BH}} = 1$.

The domain is a hollow spherical shell that excises the singularity within the black hole. In terms of the coordinate radius r, the domain extends from $r_{\mathrm{in}} = 1.8$ (just inside the event horizon) to $r_{\mathrm{out}} = 32$. At the inner boundary, all the

characteristics of the system are outgoing (i.e. are leaving the domain, towards the singularity) so no boundary condition needs to be imposed. Physically, no information enters the simulation from the interior of the black hole. At the outer boundary, we impose the analytic solution as a Dirichlet boundary condition. We choose constraint damping parameters

$$\gamma_0 = 3\exp[-(r/8)^2/2] + 0.1 \tag{2.38}$$

$$\gamma_1 = -1 \tag{2.39}$$

$$\gamma_2 = \exp[-(r/8)^2/2] + 0.1. \tag{2.40}$$

The GH gauge function $H_\sigma = \Gamma_\sigma \equiv g^{\mu\nu}\Gamma_{\sigma\mu\nu}$ is the trace of the Christoffel symbols of the Kerr-Schild metric; it is constant in time.

We use a cubed-sphere grid, with 5 spherical shells between the surfaces located at radii $r = \{1.8, 3.2, 5.7, 10, 18, 32\}$, and 2×2 tangential pieces in each of the six cubed-sphere wedges, for a total of 120 elements. We show in Fig. 2.3 two views of this grid: on the left a projected view showing the angular structure on a constant-radius surface, on the right an equatorial cut showing the radial structure. The clustering of the grid points towards the center helps to resolve the higher curvature in the spacetime near the black hole.

In Fig. 2.4 we show the stability of the Kerr black hole evolution by monitoring the simulation errors over a duration of $10^4 M_{\rm BH}$. We carry out the simulation using elements of order $N = 5$, 6, and 7; the timestep size is $\Delta t = 10^{-2}$, giving $\Delta t/\Delta x_{\rm min} \simeq 0.15$ for the $N = 7$ case. The figure's top panel shows the error $\mathrm{err}[g_{\mu\nu}]$ in the spacetime metric, a measure of the solution's drift from the exact value. The bottom panel shows the dimensionless norm $\|C\|$ of the generalized harmonic energy constraint [41], a measure of how well the numerical solution at each constant-t slice satisfies Einstein's equations. After a rapid settling of

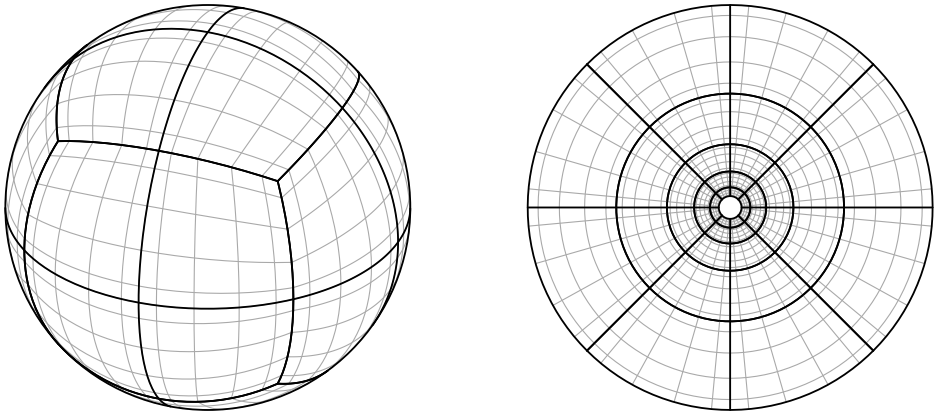

(a) Projection (b) Equatorial cut

Figure 2.3: The grid structure for the Kerr BH evolution test. Shown are (a) a projected view, and (b) an equatorial cut. The black lines show the element boundaries, the light grey lines show the Gauss Legendre Lobatto grid within each element for order $N = 5$.

the solution to its numerical equilibrium, we see clear convergence in the error quantities. We conclude that the method is convergent and stable up to at least $t = 10^4 M_{\rm BH}$, and, we presume, forever.

2.5.2 Relativistic hydrodynamic tests

Spherical accretion onto black hole

In the relativistic Bondi problem, ideal gas accretes radially onto a non-rotating black hole. The feedback from the gas onto the spacetime is ignored: the black hole mass is constant and the spacetime is Schwarzschild. We use Kerr-Schild coordinates, and again we set $M_{\rm BH} = 1$. The analytic profile for the gas flow is presented by Michel [53]; following [43], we pick a solution for a $\Gamma = 5/3$ fluid with the sonic point and mass accretion rate given by $r_{\rm crit} = 200$ and $\dot{M} = 10^{-3}$, respectively. We measure the error in the conserved relativistic density $\tilde{D}$ at a

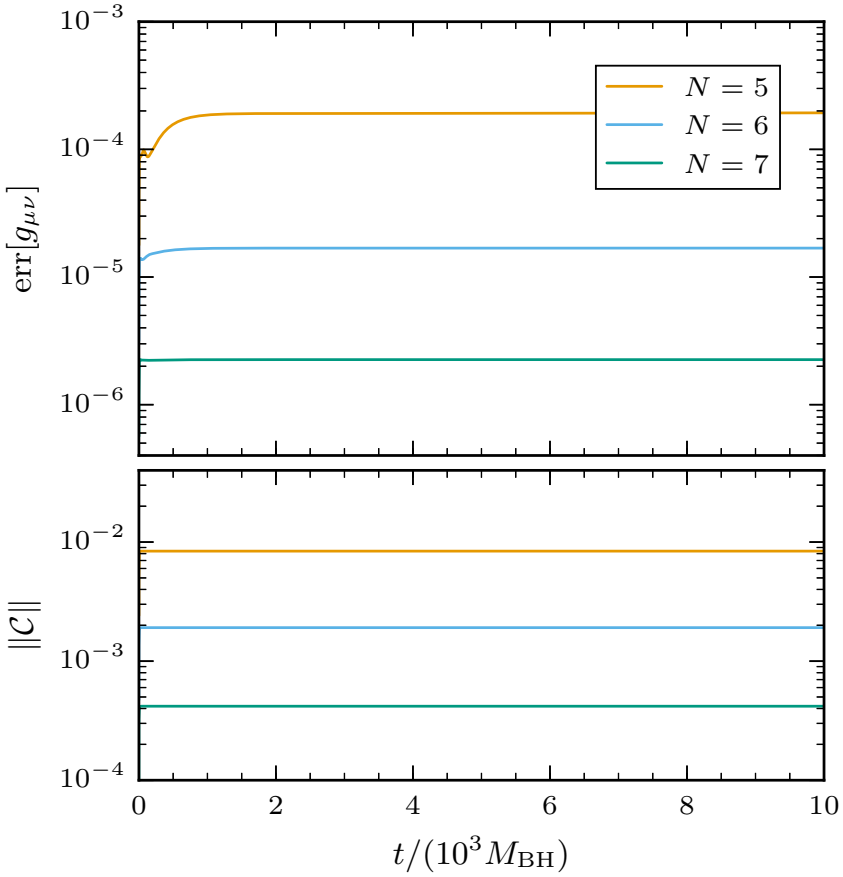

Figure 2.4: The errors during the Kerr BH evolution test. The top panel shows the error in the spacetime metric $g_{\mu\nu}$ for three different orders of the DG method. The lower panel shows the dimensionless norm of the generalized harmonic energy constraint at the same three orders.

final time $t_{\mathrm{fin}} = 100$, after evolution with timesteps of size $\Delta t = 5 \times 10^{-3}$. This timestep corresponds to $\Delta t/\Delta x_{\mathrm{min}} \simeq 0.15$ for the highest-resolution case in the convergence study ($K = 120 \times 4^3$, $N = 4$).

We evolve the fluid in a hollow spherical shell extending from $r_{\mathrm{in}} = 1.8$ (just inside the event horizon), to $r_{\mathrm{out}} = 12$. The sonic point in the accretion flow is located outside this region, so the flow is smooth and supersonic throughout the simulation domain. In this test problem we obtain significantly more accurate results when using the HLL numerical flux (vs. LLF), as the supersonic flow

is best represented by the HLL upwinding limit. At the inner boundary, the characteristics of the fluid system are outgoing (i.e. leaving the domain into the black hole), so no boundary condition needs to be applied. At the outer boundary, we impose the analytic solution as boundary condition.

We use a cubed-sphere grid similar to that of the Kerr black hole test above. At the base resolution, we divide the domain into 5 spherical shells between the surfaces located at radii $r = \{1.8, 2.7, 4, 6, 9, 12\}$, and we split each wedge into 2×2 angular portions.

We show in Fig. 2.5 the convergence under h-refinement of this grid, for elements of order $N = 2, 3, 4$. We h-refine by splitting each element into 2^3 smaller elements: we split *geometrically* in radius according to $r_{\text{split}} = \sqrt{r_{\text{lower}} r_{\text{upper}}}$, and linearly in the tangential directions. As the elements are not uniform this choice of radial split is not unique, but we find it gives reduced error compared to a linear split according to $r_{\text{split}} = (r_{\text{lower}} + r_{\text{upper}})/2$. We again see the errors converging at the expected rate.

In Fig. 2.6 we show the convergence under p-refinement. Again we use the "base" configuration of elements, and increase the order N of the method from 2 to 7. We confirm that for this smooth fluid evolution problem, the errors decrease exponentially with the order of the method.

1D shock tube test

We perform a standard 1D relativistic shock test problem, in which a high density and pressure fluid expands into a low density and pressure fluid. Following [32], we take a $\Gamma = 5/3$ ideal gas initially split at $x = 0.5$ into left and right states

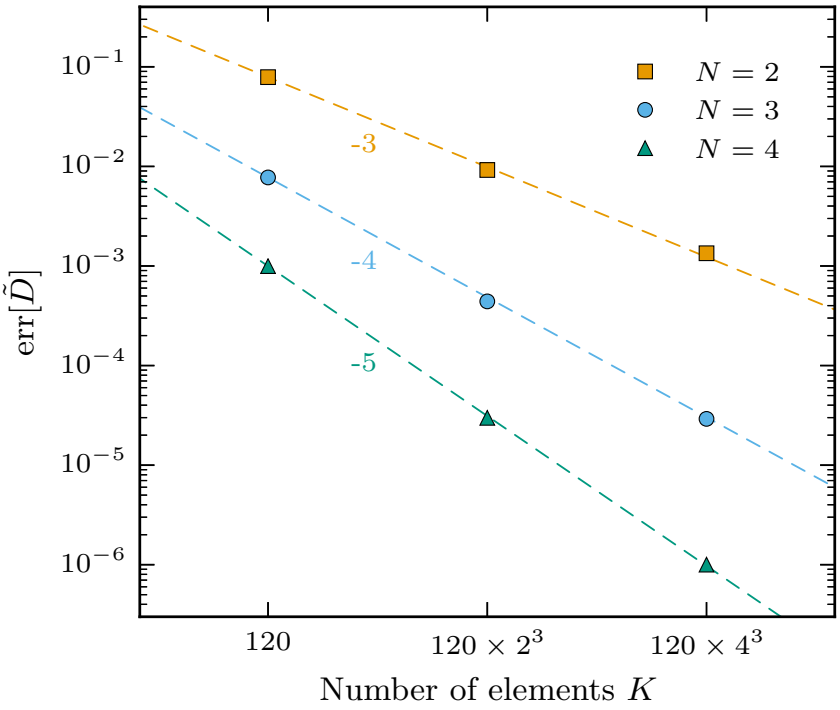

Figure 2.5: The error in the conserved density $\tilde{D}$ as a function of the number of elements (h-refinement) for the spherical accretion test. The symbols indicate the measured error norms for methods of order $N = \{2, 3, 4\}$. The dashed lines, normalized to the $K = 120$ data, indicate the expected error scaling for third, fourth, and fifth order convergence.

characterized by

$$(\rho, v_x, P) = \begin{cases} (10, 0, 40/3) & x < 0.5 \\ (1, 0, 0) & x > 0.5 \end{cases} \tag{2.41}$$

The simulation domain is an interval $x \in [0, 1]$, which we divide into $K = 160$ elements of order $N = 2$. We evolve the shock until a final time $t_{\mathrm{fin}} = 0.4$, with timesteps $\Delta t = 4 \times 10^{-3}$ ($\Delta t / \Delta x_{\mathrm{min}} = 0.128$).

In Fig. 2.7 we show the profiles of ρ, v, and P at the final state, comparing the minmod and MRS (with $\alpha = 10$) limiters. Both limiters capture the features of the shock profile. The minmod limiter produces a larger overshoot at the main shock front and increased oscillation at the front end of the rarefaction fan, a

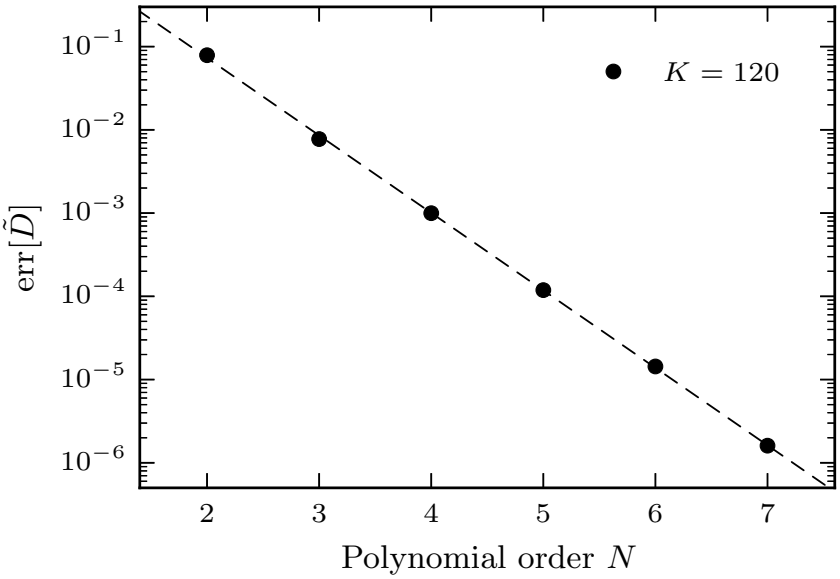

Figure 2.6: The error in the conserved density $\tilde{D}$ as a function of the order of approximation (p-refinement) for the spherical accretion test. The number of elements is fixed at $K = 120$. The dots indicate the measured errors; the dashed line is a fit demonstrating the exponential decrease in error with N.

known behavior when applying this limiter to the conserved variables (rather than characteristic variables [54]).

2D Riemann shock interaction test

We next study a standard 2D Riemann problem in which two shocks and two contact discontinuities interact. The initial conditions for the problem were first generalized from Newtonian to relativistic hydrodynamics by Del Zanna & Bucciantini [56] and later modified by Mignone & Bodo [57] to give a cleaner wave structure. The initial condition divides the computational domain $[-1, 1]^2$

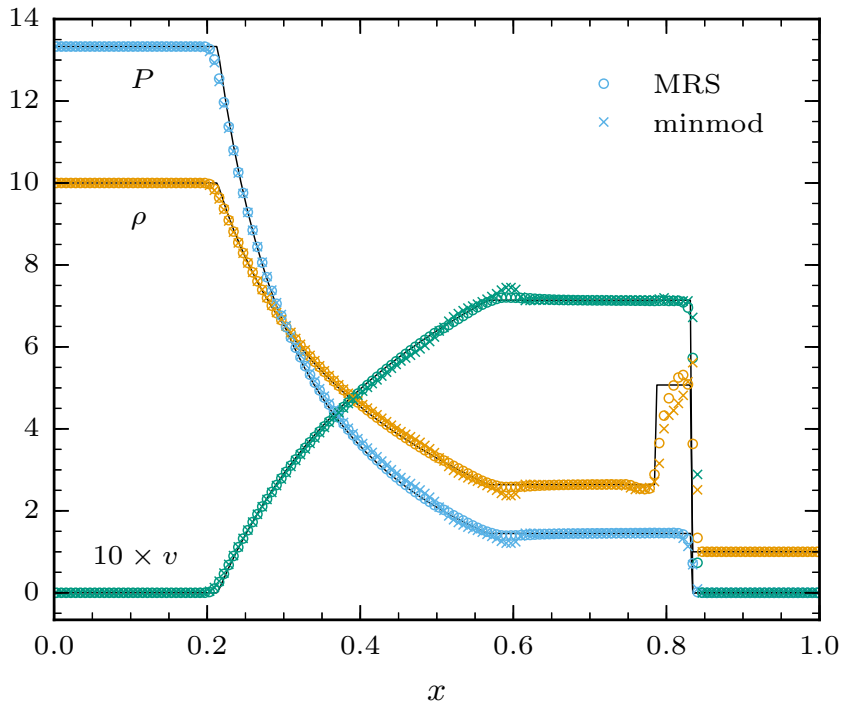

Figure 2.7: Snapshot of the fluid variables in the shock test. Shown are the fluid pressure P in blue, the rest-mass density ρ in orange, and the velocity v (scaled up 10×) in green. The mean value on each element is shown. The exact solution to the problem is given by Centrella & Wilson [55], and is plotted here in black.

into four quadrants, each of which holds a constant fluid state,

$$(\rho, v_x, v_y, P) = \begin{cases} (0.5, 0, 0, 1) & x < 0, y < 0 \\ (0.1, 0, 0.99, 1) & x > 0, y < 0 \\ (0.1, 0.99, 0, 1) & x < 0, y > 0 \\ (\rho_1, 0, 0, P_1) & x > 0, y > 0 \end{cases}, \tag{2.42}$$

where the low-density state in the upper-right quadrant is defined by $\rho_1 = 5.477875 \times 10^{-3}$ and $P_1 = 2.762987 \times 10^{-3}$. We partition the domain into 200×200 elements of order $N = 2$, and we evolve until a final time $t_{\text{fin}} = 0.8$ with timesteps $\Delta t = 10^{-3}$ ($\Delta t / \Delta x_{\text{min}} = 0.2$).

In Fig. 2.8 we show contour plots of the density ρ at the final state. We interpolate the evolved ρ onto a high-resolution uniform grid on which the contours are computed. The results in the top panel are computed with a minmod limiter, those in the bottom panel with MRS. We again see that both limiters properly resolve the structure of the solution. In this problem the MRS limiter smears out the contact discontinuities bounding the lower-left quadrant, whereas the minmod limiter keeps this feature sharp. The MRS limiter, however, gives a cleaner jet structure.

2.6 Neutron star evolutions

We evolve an isolated, spherical neutron star. The initial data for the fluid and spacetime are found by integrating the Tolman-Oppenheimer-Volkoff (TOV) equations [58, 59, 52] for the mass-energy density $\rho_E(R) \equiv \rho(R)(1 + \epsilon(R))$, enclosed ADM mass $m(R)$, and metric potential $\phi(R)$ in terms of the areal radius R. The spacetime metric is given by

$$ds^2 = -e^{2\phi}dt^2 + \left(1 - \frac{2m}{R}\right)^{-1} dR^2 + R^2 d\Omega^2. \tag{2.43}$$

In computing the TOV solution, we describe the neutron star matter by a polytropic equation of state $P = \kappa\rho^\Gamma$. From the polytrope and the density profile $\rho(R)$, the other fluid quantities can be computed. When time-evolving the solution, we return to the corresponding ideal-gas equation of state.

The results presented in this section are for a star with polytrope set by $\kappa = 100$ and $\Gamma = 2$. The star has central mass density $\rho_c = 1.28 \times 10^{-3}$, giving a stable, non-rotating TOV solution with ADM mass $M_{\rm NS} \simeq 1.4 M_\odot$ and areal

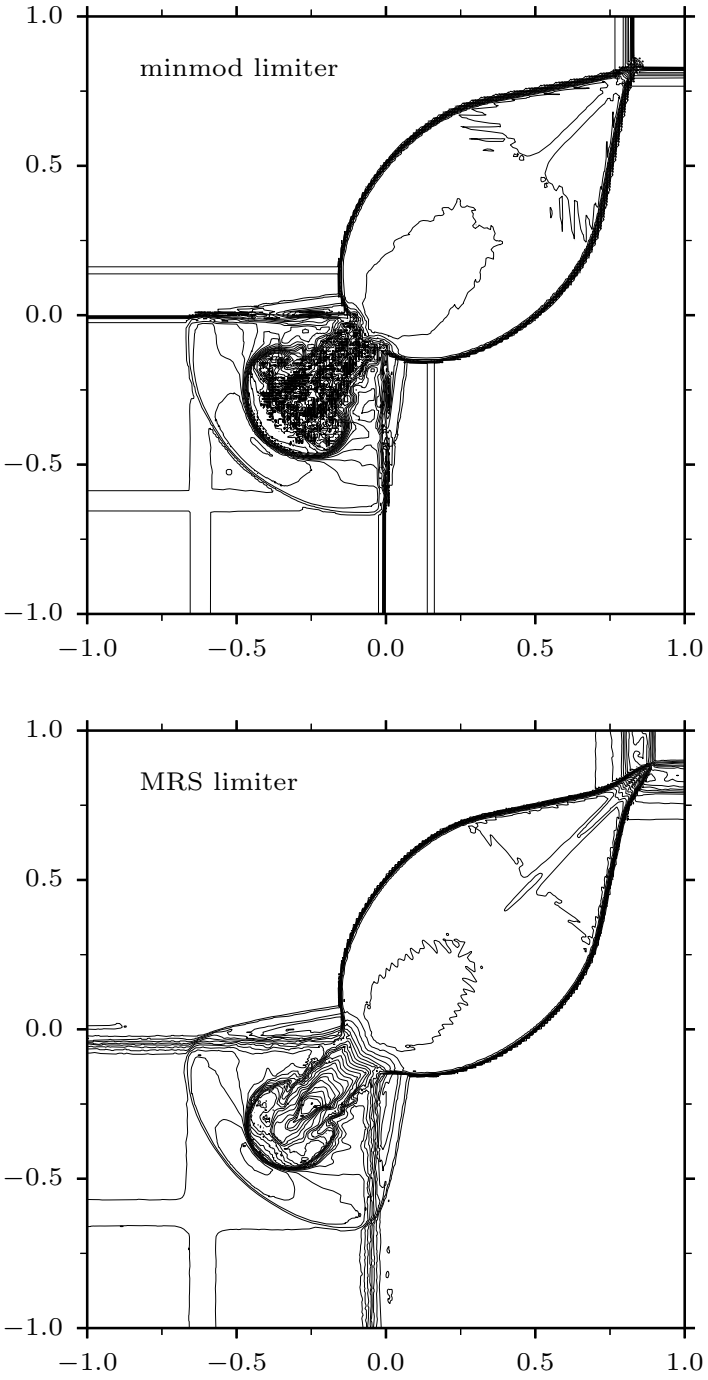

Figure 2.8: The density ρ in the 2D Riemann problem. The top panel is computed with the minmod limiter, the bottom panel with the MRS limiter. The plots each show 30 contour lines, equally spaced in $\log \rho$.

radius $R_{\rm NS} \simeq 9.6 M_\odot \simeq 14$ km. Its radius in the isotropic coordinates used during evolution is $r_{\rm NS} = 8.125$.

For the NS evolutions, we use the atmosphere fixing from [44], App. C. We set the density cutoff $\rho_{\rm atmo,cutoff} = 10^{-9}$ to give 6 orders of magnitude in density resolution. Where the density falls below this cutoff, we set the fluid to the "atmosphere" state where $\rho = \rho_{\rm atmo} = 10^{-13}$, $v_i = 0$, and $\epsilon = 0$. In regions of higher density, we constrain the specific internal energy to the range $100\rho \leq \epsilon \leq 10^4 \rho$ — bounds motivated by the polytrope describing the initial condition.

We first evolve the NS under the Cowling approximation, i.e. keeping the background spacetime fixed to the TOV solution. This remains a challenging test of the stability of the fluid code and the ability to resolve the discontinuity at the stellar surface. We then evolve the NS using the coupled GR-hydro system.

2.6.1 Cowling neutron star in spherical symmetry

We begin with 1D evolutions in spherical symmetry. For these simulations, we rewrite the conservation law (2.2) and the relativistic Euler equations in terms of spherical coordinates $\{r, \theta, \phi\}$. The DG formulation takes a form similar to (2.12) in 1D, but with a spherical divergence $\partial_r (r^2 u^r)/r^2$ instead of the Cartesian divergence $\partial_x u^x$ [4]. To avoid the coordinate singularity at $r = 0$, we set up a symmetric domain on the interval $[-12, 12]$ and use a staggered grid so that no nodes are located at the origin.

[4] The pressure term which appears in the $\tilde{S}_i$ flux, see (2.22), is included in the flux divergence term for convenience. Fundamentally, however, the pressure appears in the fluid equations as a gradient forcing term. In spherical coordinates, we treat the pressure term separately using the spherical gradient operator.

On this domain we consider two grids with different resolutions. The first grid, denoted G1, is representative of the resolution used in our 3D simulations. The second, denoted G2, has a higher resolution and is more aggressively refined near the surface of the star. In both grids, we divide the domain into five regions: the interior of the star, the surface on the left/right, and the exterior on the left/right. We use larger, higher-order elements in the interior and exterior regions, and smaller, lower-order elements in the neighborhood of the surface. The number and order of the elements within each region is listed in Table 2.1. For these 1D evolutions we only show results obtained with the minmod limiter, which is applied to the low-order elements in the surface region of the domain. We evolve the system until $t = 10^4 \simeq 50$ ms, with timesteps $\Delta t = 0.02$. On the G1 and G2 grids, this timestep corresponds to $\Delta t/\Delta x_{\rm min} = 0.14$ and 0.46 respectively.

Table 2.1: The parameters defining the 1D grids G1 and G2. For each grid, the parameters of the interior, right-side surface, and right-side exterior regions are given; the left-side surface and exterior are obtained by symmetry.

		extents	$K_{\rm region}$	$N_{\rm region}$
G1	interior	$[-7.5, 7.5]$	25	3
	surface (right side)	$[7.5, 10]$	10	1
	exterior (right side)	$[10, 12]$	4	3
G2	interior	$[-8, 8]$	101	3
	surface (right side)	$[8, 9]$	20	1
	exterior (right side)	$[9, 12]$	6	3

In Fig. 2.9 we compare evolutions of the 1D NS on the grids G1 and G2. We show, in the top two panels, the error norms in the conserved quantities $\tilde{D}$ and $\tilde{S}_r$ over the first $4000 M_\odot \simeq 20$ ms of evolution time. The evolution of err$[\tilde{D}]$ reveals two components in the dynamics: a short-period oscillatory behavior, and a gradual drift as the star settles to its numerical equilibrium configuration. The evolution of $\|\tilde{S}\|$ shows that the amplitude of the oscillations decays on a long ($t \sim 10^3$) dissipative timescale. In the bottom panel, we plot the time-dependence

of the central density ρ_c as a fractional error with respect to the initial central density $\rho_{c,0}$. The evolution on the high-resolution grid G2 shows significantly reduced errors, amplitude of oscillation, and central-density drift over time. In the full evolution to $t = 10^4$, not shown in the figure, the err$[\tilde{D}]$ values for the G1 case asymptote to roughly 10^{-3}, the oscillations in $\|\tilde{S}\|$ decay and approach a constant error floor, and the central density for the G1 case continues to slowly drop, reaching a 0.05% deficit at $t = 10^4$.

The oscillations are triggered by truncation errors from evaluating the exact TOV solution on the finite-resolution numerical grid. These errors seed perturbations in the various eigenmodes of the star, each of which subsequently resonates with its corresponding eigenfrequency. Modes with high frequencies (i.e. short wavelengths) may not be spatially resolved by the computational grid, in which case the power contained in these modes can alias into a lower-frequency mode. A common test of neutron star evolution codes is to compare the frequency spectrum of the observed oscillations to those obtained from linear theory.

We compute the frequency spectrum from the central rest-mass density during the first $4000M_\odot$ of evolution time. After subtracting the initial density offset $\rho_{c,0}$, we apply a Hanning window to the time interval and compute the discrete Fourier transform. We plot in Fig. 2.10 the absolute value of the Fourier coefficients against frequency. The dotted vertical lines indicate the (Cowling) NS's eigenfrequencies, as listed in Table I of [60]. The G1 evolution resolves few of the star's eigenmodes: the spectrum has sharp peaks corresponding to the fundamental mode and the first harmonic only. The G2 evolution, on the other hand, reproduces very clearly the fundamental mode frequency and the first four harmonic frequencies. At higher frequencies, the peaks are still identifiable,

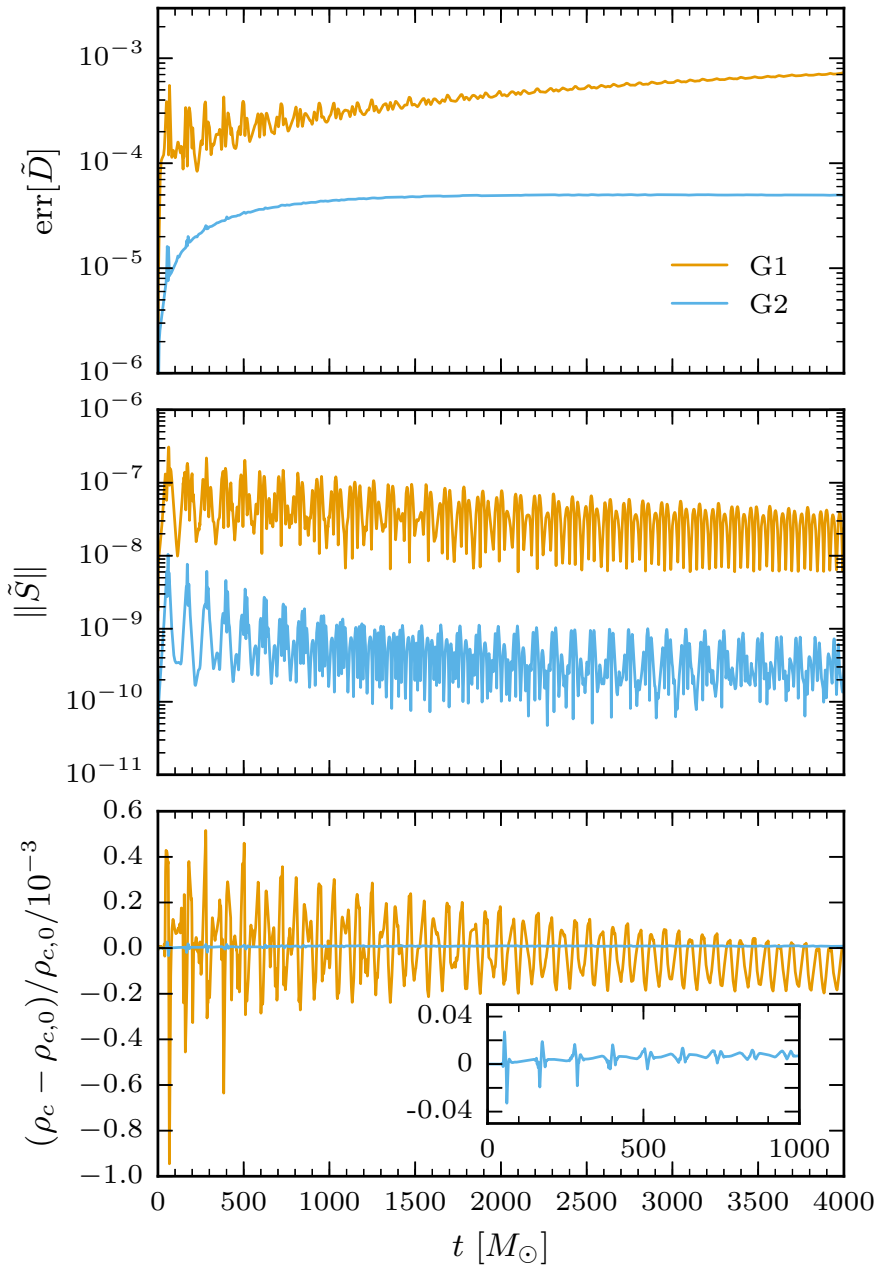

Figure 2.9: The errors in the spherically symmetric Cowling neutron star evolution. The normalized density error err$[\tilde{D}]$, the momentum error $\|\tilde{S}\|$, and the central rest-mass density error are plotted. The evolutions use the minmod limiter at the star surface. In each panel, the errors for the two grids G1 and G2 (see text for details) are plotted. The inset in the bottom panel zooms in to better show the central density evolution of the G2 case; the G1 curve is omitted from the inset for visual clarity.

though they become broader and less precisely centered. We note the presence of intermediate peaks in the spectrum, which may arise from non-linear mode interactions.

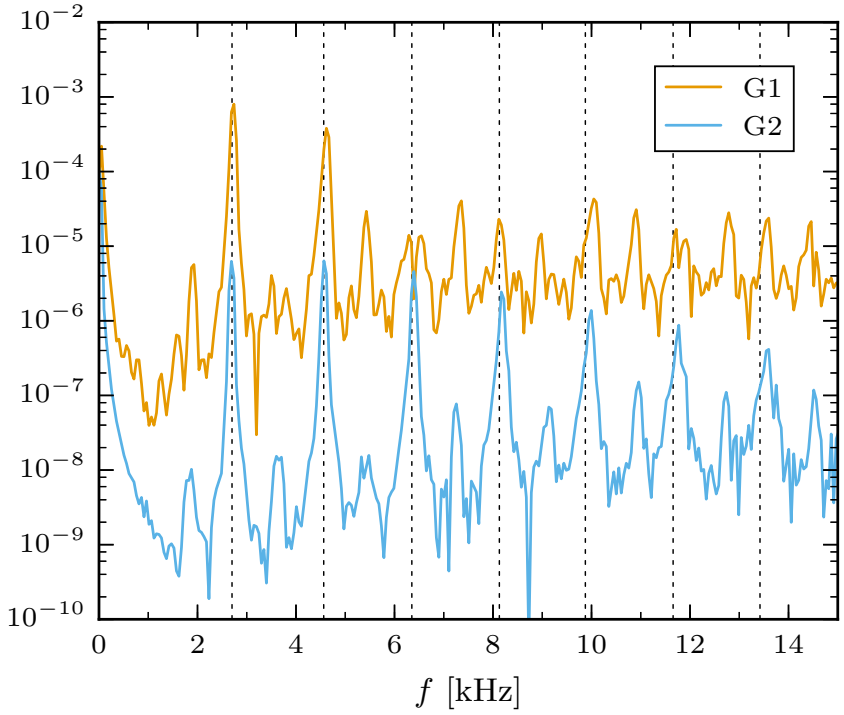

Figure 2.10: The Fourier transform of the central rest-mass density ρ_c from the spherically symmetric Cowling neutron star evolution. The data from the grids G1 and G2 are shown. The vertical dotted lines indicate the frequencies of the fundamental normal mode and the first six harmonics. The units of the vertical axis are arbitrary.

The G2 case, with roughly 210 points across the NS's radius, has a similar resolution to the 75-element simulation presented by Radice and Rezzolla [20]. While the results are not directly comparable (their 1D star self-consistently treats the gravity, and uses a uniform grid), we see a qualitative agreement in the number of resolved modes and the precision at which they are resolved. Their star, however, gives no indication of the intermediate-frequency peaks which we see.

From these results, it is clear that the evolution on the high-resolution G2 grid has significantly reduced errors. However, the lower-resolution G1 grid is sufficient to resolve the important dynamics: the star is stable on long timescales, and the oscillations as it settles to its numerical equilibrium correctly reflect the low-frequency normal modes from linearized theory.

2.6.2 Cowling neutron star in 3D

The simulation domain for the 3D star is a filled sphere extending to $r_{\max} = 24$. We construct a cubed sphere grid on this domain by using the mappings detailed in App. 2.A. As in the spherically symmetric case, we adapt the grid to the geometry by using larger, higher-resolution elements in the star's interior as well as outside the star. The region near the surface is composed of thinner spherical shells with fewer points. We consider two grids, differing in resolution at the star surface only. The grid S1 covers the surface region with $K = 10$ shells of linear ($N = 1$) order. The grid S2 uses $K = 5$ shells of quadratic ($N = 2$) order over the same physical region; an equatorial cut through this grid is shown in Fig. 2.11. The complete details of the two grid structures are listed in App. 2.B. In these 3D evolutions, we compare the action of the minmod and MRS limiters at the star's surface. As before, we apply the limiter to the surface region of the grid only. We evolve the hydro system until $t = 10^4$, with timesteps $\Delta t = 0.04$ (for both grids, $\Delta t/\Delta x_{\min} \simeq 0.61$).

In long evolutions on the cubed sphere grids, we find that the conserved momentum $\tilde{S}_i$ exhibits a slowly growing instability. The instability is caused by aliasing of the spectral modes as a result of an insufficiently resolved quadrature

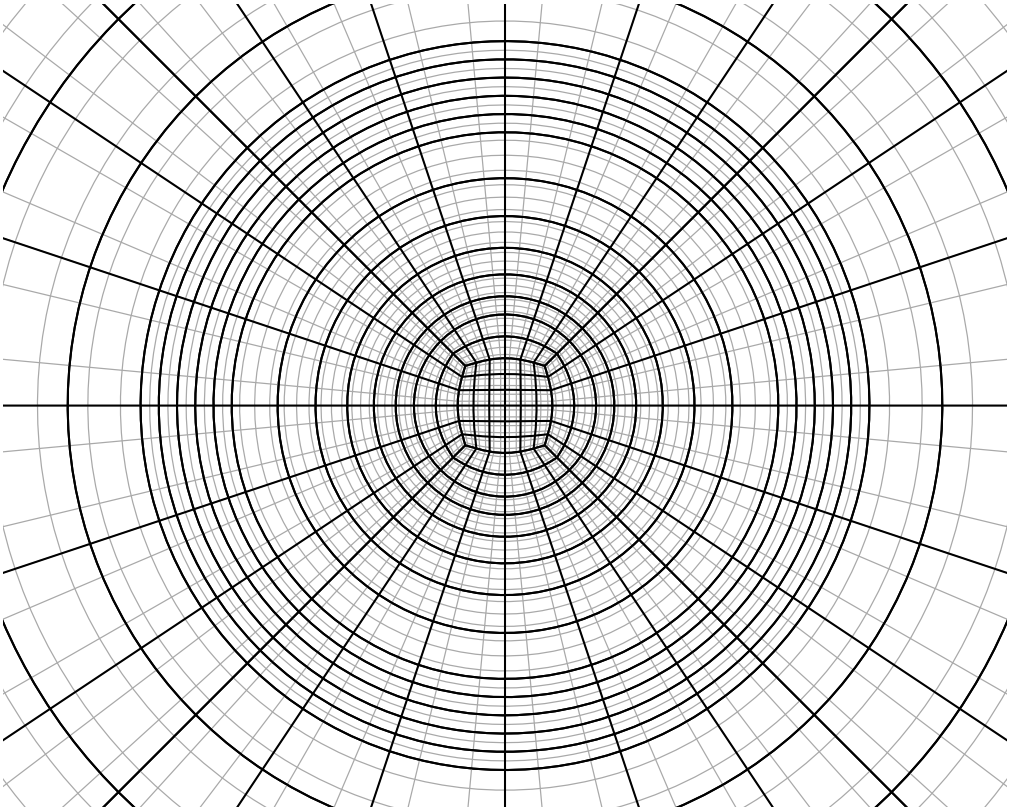

Figure 2.11: The grid S2 used in the 3D neutron star evolutions. The black lines show the element boundaries, the light grey lines show the Gauss Legendre Lobatto grid within each element. The details of the grid mappings and structure are given in Apps. 2.A and 2.B respectively. The S1 grid has a similar structure, but the thin shells forming the surface are split in half radially.

rule in the DG method (see paragraph below (2.11)), and is strongest in the central cube-to-sphere portion of the grid. We apply a filter, described in App. 2.C, to stabilize the problem and allow evolution to at least $t = 10^4$. The filter is broad (draws power from many modes) but weak (reduces mode power over long timescales). Because of this choice, the filter only weakly affects short-timescale dynamics such as the star's oscillations as it settles to the numerical equilibrium.

We plot, as before, the error norms in $\tilde{D}$, $\tilde{S}_i$, and ρ_c during the evolution in Fig. 2.12. From the four possible combinations of limiters and grids, we show here the best-performing grid for each limiter: the S1 grid for evolution with

minmod, and the S2 grid for evolution with MRS. The errors in the minmod-S1 simulation closely match those seen in the spherically symmetric case (the G1 curves in Fig. 2.9) for all three error norms. In the MRS-S2 evolution, however, we see a different behavior, with oscillations in err$[\tilde{D}]$ and ρ_c that slowly *grow* in amplitude over time. Additionally, in $\|\tilde{S}\|$, a growing error with a significant component at high frequencies is seen.

To better understand the difference in behavior between the minmod and MRS limiters, we look next at the radial distribution of the errors. In Fig. 2.13 we show the angle-averaged errors in the fluid density and 3-velocity as a function of radius in the star. The darker lines in this plot show the angle-averaged errors, and the lighter filled region shows the spread in error values at fixed radius [5]. From this plot several observations can be made. Firstly, while the minmod limiter maintains excellent spherical symmetry in the star, the MRS case shows a large spread in the error values, indicating a loss of spherical symmetry. Secondly, while the density and velocity errors in the minmod case are largest at the surface of the star, denoted by a vertical dotted line in the figure, the fluid remains confined within the true surface of the star. When using MRS, the star instead extends significantly beyond the true surface: matter with non-negligible densities and large ($v > 0.01$) velocities is present out to $r = 9.5$. Our interpretation is that the MRS limiter provides insufficient damping of small-scale fluctuations in the atmosphere near the star. These slowly grow, leading to the expansion of the star beyond its true surface and the contamination of the solution inside the star.

The two remaining limiter-grid combinations, minmod-S2 and MRS-S1, do

[5]Inside of $r = 2.5$, where the grid is no longer spherical, fewer points are located in each radius bin and so the angle averaging produces noisier data.

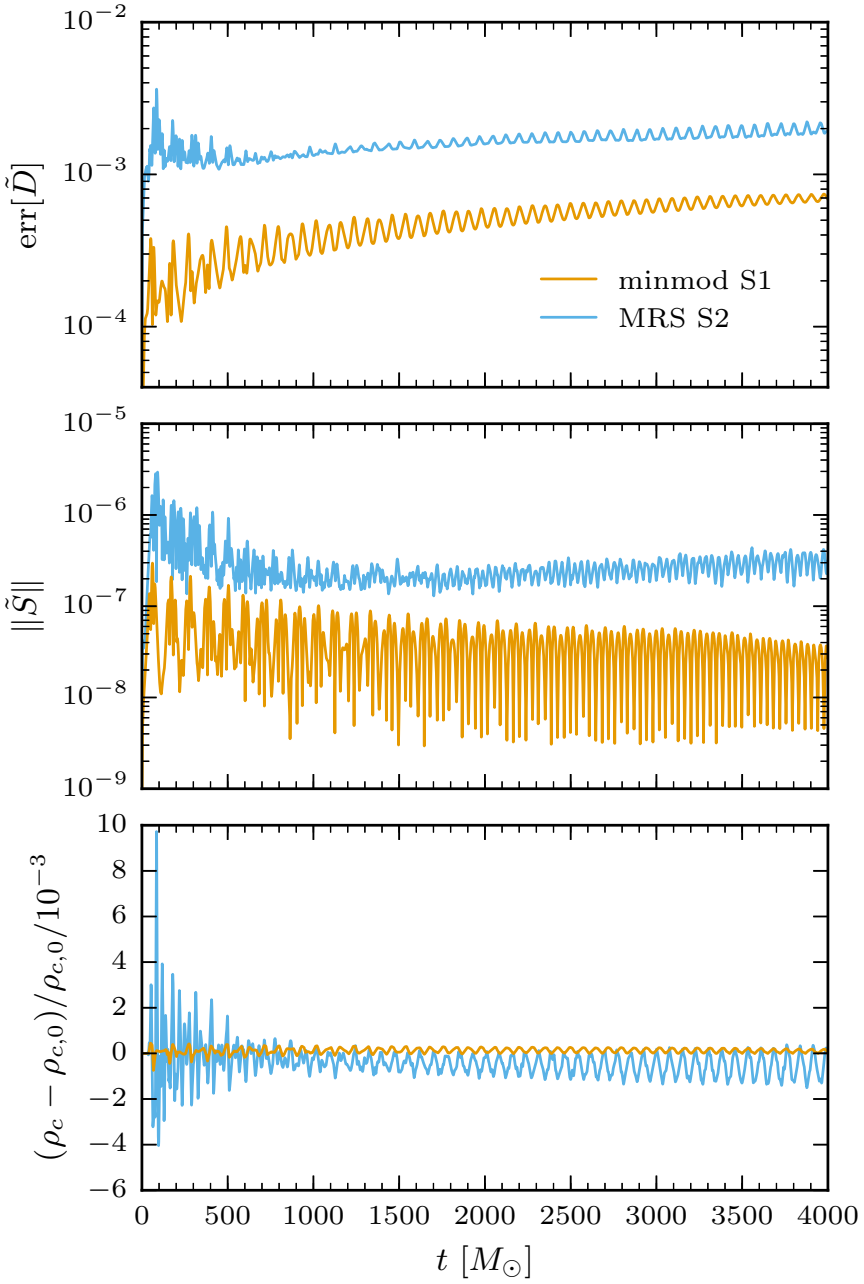

Figure 2.12: The errors in the 3D Cowling neutron star evolution (see Fig. 2.9 for details). Shown are results using the minmod limiter on the S1 grid (thinner, linear, surface elements) and the MRS limiter on the S2 grid (thicker, quadratic, surface elements).

not perform as well as the combinations shown above. The minmod-S2 configuration, though stable and robust, suffers from large density errors at the surface

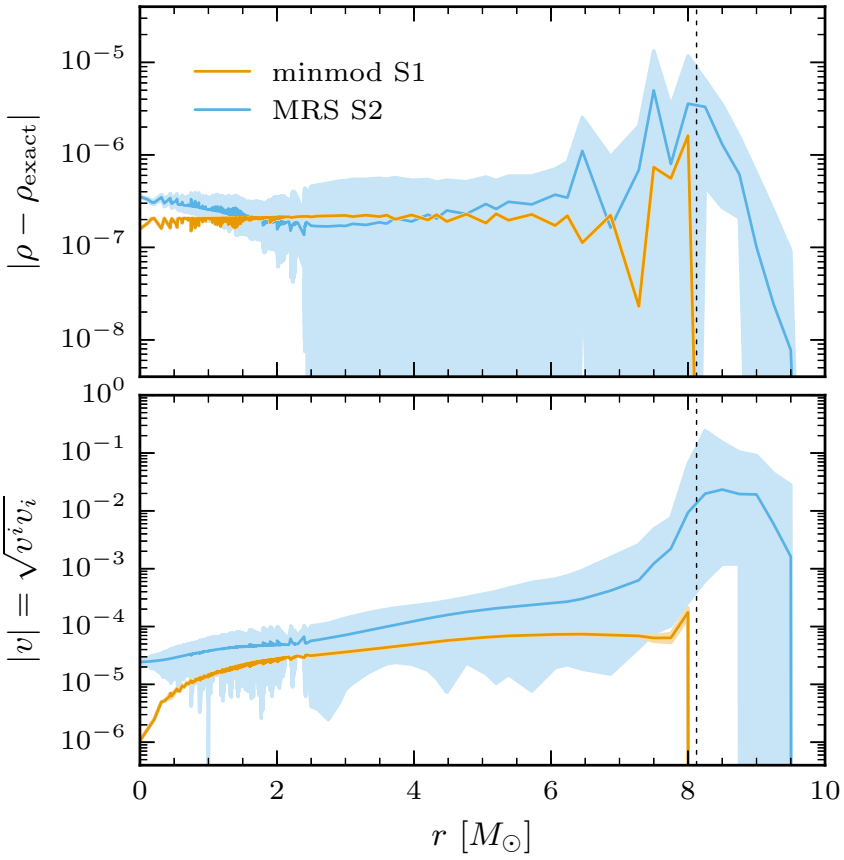

Figure 2.13: The angle-averaged density and 3-velocity error at time $t = 1000$ in the Cowling star evolution. The darker lines indicates the average value of the error vs. radius. The lighter filled region indicates the range of error values. The vertical dotted line indicates the location of the TOV star surface at $r \simeq 8.125$.

of the star. The configuration is also very dissipative, with the initial oscillations being strongly damped on $t \sim 300$ timescales. The larger errors and dissipation occur because the minmod limiter linearizes the solution on the $N = 2$ elements at the surface, resulting in the loss of information. The MRS-S1 configuration has the same qualitative behavior as MRS-S2, but allows the star to expand even more. We find the stellar matter extending out to $r \sim 15$ by a time $t = 1000$, again with a significant loss of spherical symmetry. We surmise that the MRS limiter on low-order elements is even less able to contain the surface of the star because,

with fewer grid points per element, it fails to adequately sample the shape of the solution.

We conclude from these experiments that the MRS limiter — although effective at handling shocks — is poorly suited to the task of controlling a stellar surface on the spherically conforming grids that we are using. The remainder of this paper therefore considers only the minmod limiter.

We again compute the frequency spectrum of the stellar oscillations from ρ_c, using the procedure described for the spherical case. The results for the minmod-S1 case are shown in Fig. 2.14. Comparing this spectrum to the G1 spectrum from Fig. 2.10, we see good agreement: the first two resonant frequencies are clearly resolved, and additional peaks at higher frequencies are suggestive but not conclusive.

2.6.3 GR-hydro neutron star

For the coupled GR-hydro evolutions, we again use two grids: the grid S1, from above, and a higher-resolution grid S1R. We obtain S1R from S1 by h-refinement of the surface elements and p-refinement of the interior and exterior elements; details of the grid structure are given in App. 2.B. The hydrodynamics are treated as for the Cowling star, with a minmod limiter at the star surface. We additionally evolve the spacetime geometry, with the constraint damping parameters set to

$$\gamma_0 = 0.1 \exp[-(r/8)^2] + 0.01 \tag{2.44}$$

$$\gamma_1 = -1 \tag{2.45}$$

$$\gamma_2 = 0.3 \exp[-(r/8)^2] + 0.01. \tag{2.46}$$

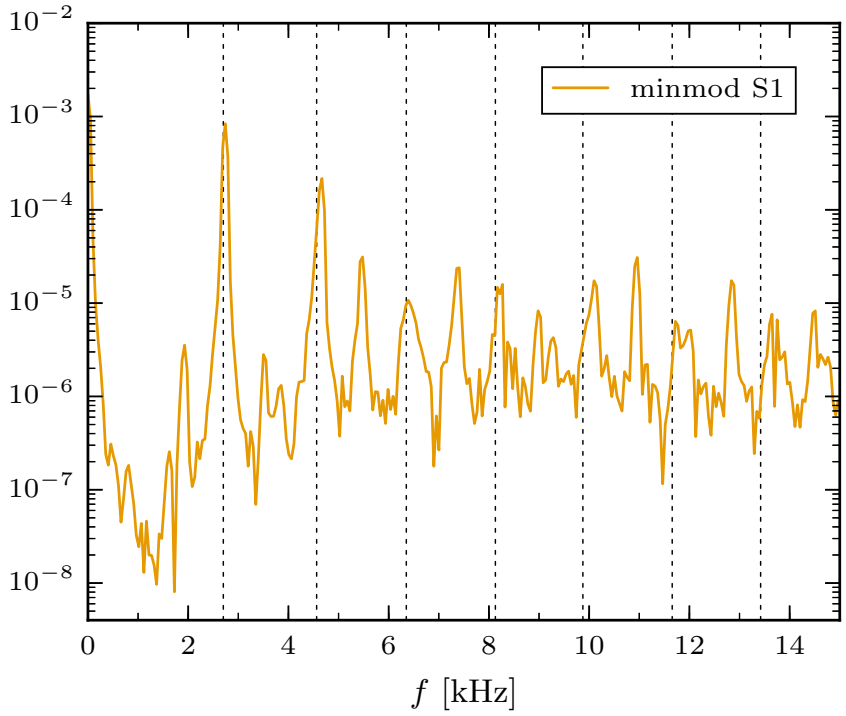

Figure 2.14: The Fourier transform of the central rest-mass density ρ_c from the 3D Cowling neutron star evolution. The vertical dotted lines indicate the frequencies of the fundamental normal mode and the first six overtones. The units of the vertical axis are arbitrary.

The gauge function H_σ is computed, as for the Kerr BH evolution, from the contraction of the Christoffel symbols of the exact metric; it is constant in time. We evolve the combined system until $t = 10^4 \simeq 50$ ms, with timesteps $\Delta t = 0.04$ on the S1 grid ($\Delta t/\Delta x_{\rm min} \simeq 0.61$), and $\Delta t = 0.025$ on the S1R grid ($\Delta t/\Delta x_{\rm min} \simeq 0.59$).

We show in Fig. 2.15 the error norms in $\tilde{D}$, $\tilde{S}_i$, and ρ_c for the self-consistent NS evolution. Comparing the results from the grid S1 to the minmod-S1 Cowling results of Fig. 2.12, we see that the self-consistent NS is more dissipative than the Cowling one — the oscillations decay quickly and become negligible by $t \sim 3000$. Additionally, we see that the star settles to a different equilibrium, because the gravity responds to the fluid rather than providing a fixed potential well. The

equilibrium central density is higher than the TOV values, indicating that in its numerical equilibrium, the star has compressed slightly. The errors using the higher-resolution grid S1R are significantly reduced as compared to the grid S1, both in the global norms of the conserved quantities and in the central density.

We compute once more the frequency spectrum of the stellar oscillations from ρ_c, and we show in Fig. 2.16 the results from evolutions on the grids S1 and S1R. We also indicate the first 7 eigenfrequencies from linear theory by the vertical dotted lines; these values are obtained from Fig. 11 of [20]. In the lower-resolution S1 case, we see clear peaks corresponding to the fundamental mode and the first three harmonics (albeit with an increasing frequency shift towards higher frequencies). The S1R case is qualitatively similar, but curiously has no peak corresponding to the fundamental mode. By evolving a perturbed NS, however, in which the initial density profile has a long-wavelength perturbation of the form

$$\rho \to \rho \left(1 + 10^{-3} \left[r/r_{\rm NS} - (r/r_{\rm NS})^3\right]\right), \tag{2.47}$$

we recover a strong peak in the spectrum at the fundamental frequency. We conclude that, in the unperturbed NS, the initial truncation errors on the S1R grid do not significantly seed the star's fundamental mode of oscillation. No significant improvement in the mode resolution is seen in going from S1 to S1R, but (unlike in the spherically symmetric case) the resolution change is minor: the grid S1R has only 2× more grid points than the grid S1.

We conclude our analysis by comparing the accuracy of the DG and FV methods for the NS problem. We use the SpEC hydro code — a FV code that takes a dual-grid approach for coupled GR-hydro problems — to perform additional evolutions of the NS. The spacetime is evolved on a high-resolution grid of

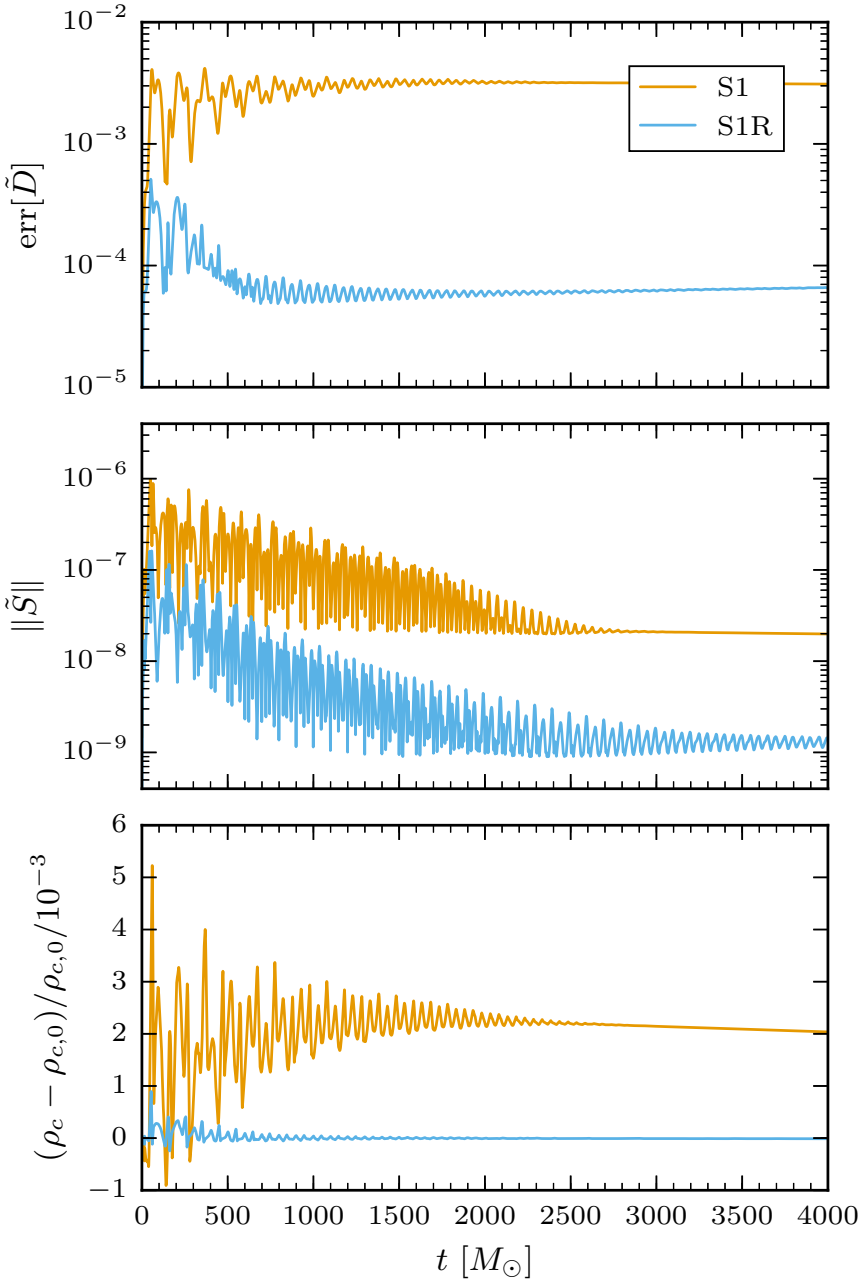

Figure 2.15: The errors in the coupled GR-hydro neutron star evolution (see Fig. 2.9 for details). Shown are results using the minmod limiter on the grids S1 (base resolution) and S1R (higher resolution).

nested spherical shells using a pseudo-spectral penalty method, closely related to the DG method presented in this paper. The matter is evolved on a Cartesian grid covering the interval $[0, 12]$ in each direction (octant symmetry is imposed),

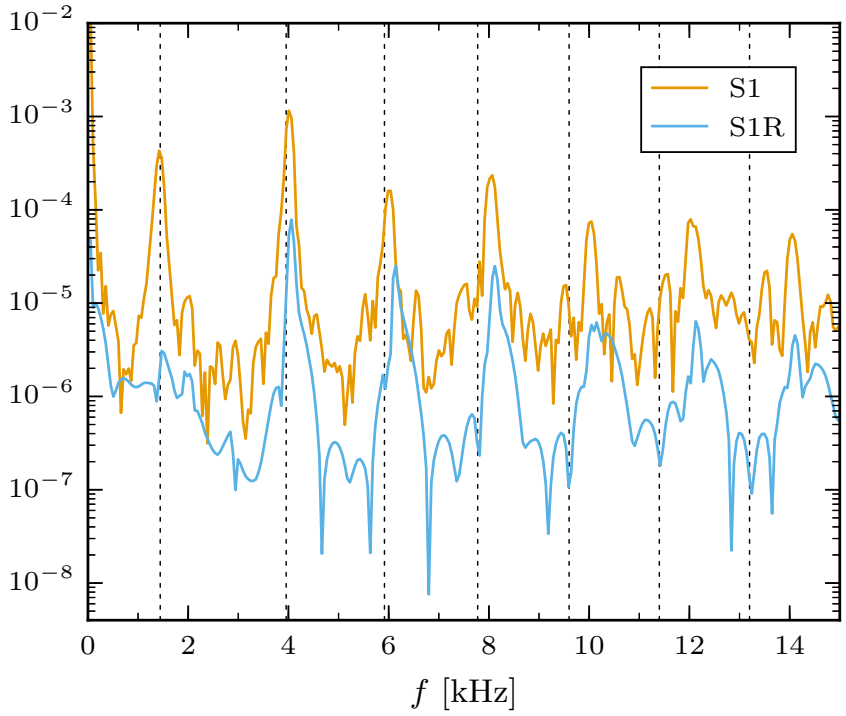

Figure 2.16: The Fourier transform of the central rest-mass density ρ_c from the coupled GR-hydro neutron star evolutions on the S1 and S1R grids. The vertical dotted lines indicate the frequencies of the fundamental normal mode and the first six harmonics. The units of the vertical axis are arbitrary.

using a 4^{th}-order finite difference scheme and a WENO shock-capturing scheme. We consider two resolutions for the hydro grid. For the base resolution, we use the same number of grid points inside the volume of the star as the S1 grid of the DG evolution, giving a grid of 51^3 points on $[0, 12]^3$. The high-resolution grid uses 101^3 points. These cases are labelled FV1 and FV1R respectively.

In Fig. 2.17 we compare the central density errors in evolutions with the DG and FV methods. The DG results make use of the grids S1 and S1R (a $2\times$ increase in the number of grid points), and the FV results make use of FV1 and FV1R (an $8\times$ increase) described above. Comparing the results, we find a few differences between the DG and FV evolutions. First, the DG method is more dissipative

than the FV method used, with the star's oscillations damping significantly on $t \sim 1000$ timescales. We believe this is because of the use of a low-order shock-capturing scheme in the surface regions in the DG case. Second, the error in the central density is greatly reduced in the DG evolution: comparing the cases S1 and FV1 with equal resolution, we see that the drift of the central density over time is much lower in the DG case. Finally, in going to the higher-resolution grids S1R and FV1R, we find that the error decreases much more rapidly in the DG case even though the resolution change is smaller. This is because the DG method has higher order in the bulk of the star's interior, so that p-refinement leads to rapid convergence. Precise statements about the order of convergence for the DG results are difficult to make, however, because we use geometrically adapted grids with elements of different order.

2.7 Conclusions

In this paper we have presented the first 3D evolutions, using a DG method, of (a) a Kerr BH, and (b) a general-relativistic NS treated self-consistently. We adopted the DG formulation of Teukolsky [28] to solve the generalized harmonic formulation of Einstein's equations and the València formulation of general-relativistic hydrodynamics. We used conforming grids to take advantage of the problem symmetries, and we evolved the spacetime and matter together on this grid. We implemented the DG method in the SpEC framework and showed convergence and shock-capturing tests for our code. We also evolved NSs under the Cowling approximation (fixed spacetime metric) in spherical symmetry and in 3D.

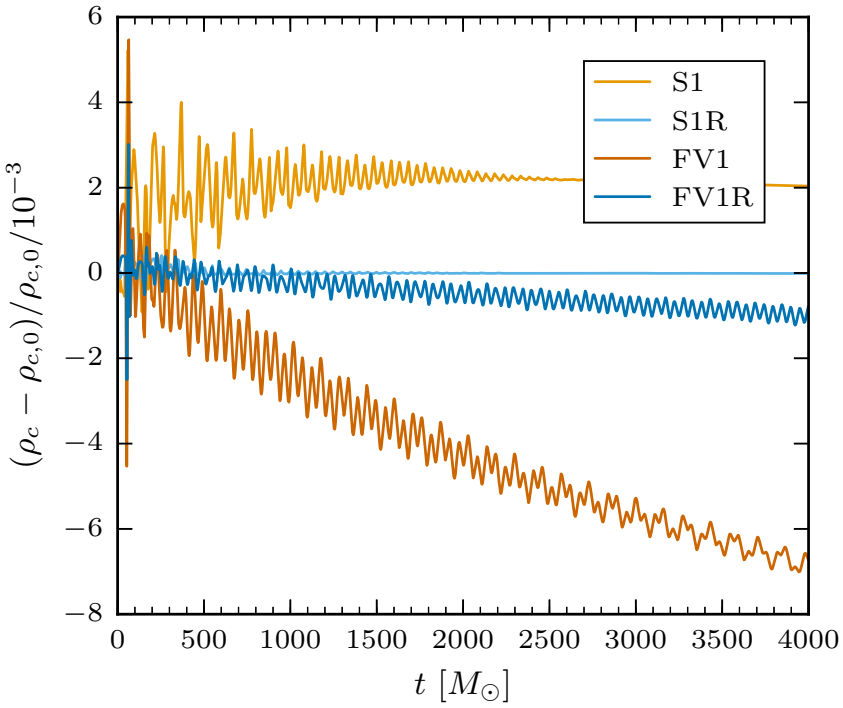

Figure 2.17: The central-density error in the coupled GR-hydro neutron star, for evolutions using the DG and FV methods. For each method, two resolutions are shown: the DG method uses grids S1 (base) and S1R (refined, with 2× as many grid points); the FV method uses grids FV1 (base) and FV1R (refined, with 8× as many grid points).

With the 3D Kerr BH evolution, we showed that the DG method is accurate and stable for long-timescale spacetime evolutions. By adapting the grid to the (nearly) spherical geometry of the BH spacetime, we were able to excise the singularity from the domain — a promising result for the future use of the DG method in compact-object binary simulations. The success of the DG method here draws on previous successes of the (closely-related) spectral penalty methods for the BH problem.

For the NS, we again showed long and stable evolutions and we additionally recovered the eigenfrequencies from linearized theory. By using domains conforming to the star's spherical geometry and adapted to resolve the surface,

we were able to obtain good accuracy with comparatively few elements and a low-order shock-capturing scheme. We compared the DG evolution to a FV evolution and found significantly lower errors and improved rate of convergence from the DG case.

Improvements to our work will include the adoption of higher-order shock-capturing schemes (e.g. WENO) to lower the errors in the treatment of the star surface. The development of an adaptive mesh-refinement scheme will allow geometrically adapted grids to be used in systems with reduced symmetry and/or dynamics. These improvements are planned for implementation in the SpECTRE code, where they will enable evolutions with the DG method of dynamical systems such as rotating or unstable stars.

Though one of the benefits of the DG method over the FV method lies in its ability to scale to large machines, we were not able to show scaling results from our implementation in SpEC. As discussed, the SpEC framework scales poorly to large numbers of elements. For the NS results shown, the domains are composed of over 5000 elements, enough for SpEC's scaling to break down and for timing measurements to lose their significance. We do note that our DG method, which uses the same grid for the spacetime geometry and the matter, solves the Einstein equations on a denser grid of points than the dual-grid SpEC hydro code. This adds a significant computational cost for the runs presented in this paper, but the cost would be reduced in the context of a "production" simulation with a spacetime grid extending to large radii, where the addition of extra grid points in the central portion of the domain is less significant.

Acknowledgements

We thank Andy Bohn, Mike Boyle, Nils Deppe, Matt Duez, Francois Foucart, Curran Muhlberger, and Will Throwe for many helpful conversations through the course of this work. We gratefully acknowledge support for this research at Cornell from the Sherman Fairchild Foundation and NSF grants PHY-1606654 and AST-1333129. F.H. acknowledges support by the NSF Graduate Research Fellowship under Grant No. DGE-1144153. Computations were performed at Caltech on the Zwicky cluster, which is supported by the Sherman Fairchild Foundation and by NSF award PHY-0960291, and on the Wheeler cluster, which is supported by the Sherman Fairchild Foundation. The figures in this paper are produced with matplotlib [61].

2.A Cubed sphere mappings

In simulations of systems with spherical symmetry, we use grids based on the cubed sphere [62]. The cubed sphere is obtained by projecting the faces of a cube onto the sphere, thereby defining a grid on the sphere composed of six deformed Cartesian grid patches. The radial direction is introduced by tensor product, giving a grid on a hollow spherical shell composed of six mapped cubes; we call each of these mapped cubes a "wedge" of the spherical shell. For our neutron star simulations, however, we require a filled sphere topology, rather than a hollow spherical shell.

To obtain a grid on the filled sphere, we place an element at the center of the sphere and deform the surrounding grid to conform to the central element. One

possibility is to use an unmapped central cube, surrounded by a shell of elements that interpolate from the cube to an enclosing sphere, as shown in panel (a) of Fig. 2.18. In numerical experiments, we find that this grid often suffers from large errors along the diagonal axes (e.g. the line $x = y = z$) where three of the wedges meet, due to the large grid distortions at these locations. This source of error can be reduced by using a "rounded" cube, which reduces the grid distortion in the wedges, as shown in panel (b) of Fig. 2.18. We are not aware of previous uses of such a grid configuration, so we show here the mappings used.

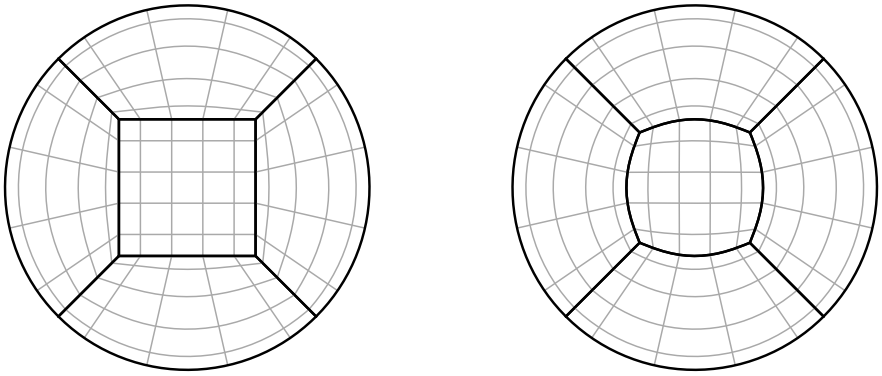

(a) Unmapped cube (b) Rounded cube

Figure 2.18: Two grids on the filled sphere, constructed from a cubed sphere with (a) an unmapped cube as central element, and (b) a rounded cube as central element. Both panels show an equatorial cut through the grid. The grids are obtained from the mappings given in App. 2.A, with parameters $c_{\min} = 0$ in panel (a), and $c_{\min} = 0.66$ in panel (b); in both panels $c_{\min} = 1$, $x_{\min} = 0.75$, and $x_{\max} = 2$. The black lines show the element boundaries, the light grey lines show the Gauss Legendre Lobatto grid within each element for order $N = 5$.

2.A.1 Wedges

Each of the six wedges of the cubed sphere is uniquely defined by three sets of parameters:

1. The position of the wedge on the sphere, indicated by one of the axes $+x$, $-x, +y, -y, +z, -z$.
2. The curvatures of the inner and outer surfaces, c_{min} and c_{max} respectively. When $c = 0$, that surface is flat (i.e. forms a cube); when $c = 1$ that surface is spherical. Each curvature satisfies $c \in [0, 1]$.
3. The "radii" x_{min} and x_{max} where the wedge's inner and outer surfaces intersect its defining axis. When one of these surfaces is spherical, the corresponding $x_{\text{min/max}}$ is the true radius of that surface. These "radii" satisfy $0 < x_{\text{min}} < x_{\text{max}}$.

The mapping from the reference element to each of the six wedges of the cubed sphere is obtained by composing four transformations,

$$\mathbf{x}(\bar{\mathbf{x}}) = (\mathbf{x}_{\text{rot}} \circ \mathbf{x}_{\text{cs}} \circ \mathbf{x}_{\text{tan}} \circ \mathbf{x}_{\text{affine}})(\bar{\mathbf{x}}). \tag{2.48}$$

The first transformation, $\mathbf{x}_{\text{affine}}$, shifts and scales the reference cube along the $+x$ axis to obtain a parallelepiped spanning $0 < x_{\text{min}} \leq x \leq x_{\text{max}}$. The y and z coordinates are unaffected. The second transformation, $\mathbf{x}_{\text{tan}}$, is optional; it maps the tangential coordinates y and z according to $y \to \tan(\pi y/4)$ (and same for z), which produces an equiangular grid on the destination spherical surface. Unless otherwise specified, this optional mapping is used. Then $\mathbf{x}_{\text{cs}}$ deforms the parallelepiped into one wedge of the cubed-sphere, intersecting the $+x$ axis at x_{min} and x_{max}. This transformation is given below. Finally $\mathbf{x}_{\text{rot}}$ rotates the wedge to the correct position on the sphere.

The transformation $\mathbf{x}_{\text{cs}}(\bar{\mathbf{x}})$ is computed with the intermediate steps

$$a = 1/\sqrt{1 + \bar{y}^2 + \bar{z}^2} \tag{2.49}$$

$$b_{\min} = x_{\min}\,(1 + c_{\min}(a - 1)) \tag{2.50}$$

$$b_{\max} = x_{\max}\,(1 + c_{\max}(a - 1)) \tag{2.51}$$

$$\xi = b_{\min} + (b_{\max} - b_{\min})\frac{\bar{x} - x_{\min}}{x_{\max} - x_{\min}} \tag{2.52}$$

$$\mathbf{x}_{\text{cs}}(\bar{\mathbf{x}}) = (\xi, \xi\bar{y}, \xi\bar{z}). \tag{2.53}$$

Fig. 2.18 shows two (filled) cubed sphere grids where the outer surface is spherical and the inner surface has $c = 0$ or 0.66. Fig. 2.3 shows a cubed sphere grid where both surfaces are spherical, and each wedge is divided radially and tangentially into several elements. This is achieved by dividing the unit cube into the corresponding elements before applying the chain of maps in (2.48).

2.A.2 Rounded central cube

The mapping from the reference element to the rounded central cube is chosen to conform to the inner boundary of the cubed sphere wedges. The cube is therefore parametrized by $x_{\min}$ and $c_{\min}$ from the inner boundary of the wedges, and by whether (or not) the equiangular transformation is applied. The mapping is again obtained by composition,

$$\mathbf{x}(\bar{\mathbf{x}}) = (\mathbf{x}_{\text{rc}} \circ \mathbf{x}_{\tan})(\bar{\mathbf{x}}), \tag{2.54}$$

with $\mathbf{x}_{\rm rc}$, the transformation that deforms the cube, given by,

$$a = 1/\sqrt{1 + \bar{x}^2\bar{y}^2 + \bar{x}^2\bar{z}^2 + \bar{y}^2\bar{z}^2 - \bar{x}^2\bar{y}^2\bar{z}^2} \tag{2.55}$$

$$b_{\rm min} = x_{\rm min}\,(1 + c_{\rm min}(a-1)) \tag{2.56}$$

$$\mathbf{x}_{\rm rc}(\bar{\mathbf{x}}) = (b_{\rm min}\bar{x}, b_{\rm min}\bar{y}, b_{\rm min}\bar{z}). \tag{2.57}$$

Inverting this mapping for $\bar{\mathbf{x}} = \mathbf{x}_{\rm rc}^{-1}(\mathbf{x})$ requires root finding and so is done numerically.

Fig. 2.11 shows a cubed sphere grid with a rounded central cube. The shape of the cube is set by the curvature $c = 0.55$ of the inner wedge surface. In this grid, the equiangular mapping is *not* used. Just as for the wedges, the division of the central cube into several elements is achieved by dividing the unit cube prior to applying the chain of maps in (2.54).

2.B The neutron star grids

Here we give the parameters of the cubed-sphere grid structures used in our 3D neutron star evolutions. The grids are divided into four physical regions: the cube-to-sphere transition elements are placed in the center of the star; the bulk of the star's interior is made up of spherical shells with higher-order elements; the surface region has thin spherical shells with low-order elements; the exterior again has spherical shells with higher-order elements. Three grid structures are used over these regions, denoted S1, S2, and S1R.

The grids S1 and S2 differ only in the resolution at the star's surface. In this region, the S1 grid uses 10 shells of linear ($N = 1$) order, whereas the S2 grid uses 5 shells of quadratic ($N = 2$) order. The overall radial structure of the grids is

given in Table 2.2: for each region of the grid, the table gives the parameters of the cubed sphere wedges that make up the region. The angular structure of both grids is obtained by splitting each wedge into 6×6 elements, each of which has order $N = 3$ in the two tangential directions. The equiangular tangent mapping is *not* applied — omitting this mapping gives a more optimal resolution of the cube in the center of the star, but creates a non-uniform grid on the spherical surface. The central cube-to-sphere mapping is fixed by the parameters of the innermost shell, and the resolution of these elements is set by conforming to the angular grid of the shells. The S1 grid has a total of 5184 elements, with $\Delta x_{\min} \simeq 0.0657$. The S2 grid, shown in Fig. 2.11, has a total of 4104 elements, and the same $\Delta x_{\min}$.

The S1R grid is obtained from S1 by selectively refining to further take advantage of the hp-adaptivity of the DG method: h-refinement is used in the neighborhood of the surface where the solution is not smooth, and p-refinement is used in the smooth interior and exterior regions. The radial parameters are again given in 2.2; the angular parameters are as for S1 but with $N = 4$ in the two tangential directions. This grid has 7344 elements, with $\Delta x_{\min} \simeq 0.0447$, and with roughly twice as many grid points inside the NS as for the S1 case.

2.C Cubed sphere filtering

In our NS evolutions on cubed sphere grids, we find an instability in the conserved momentum $\tilde{S}_i$ that leads to a slow growth of this quantity on timescales of hundreds of $M_\odot$. We therefore apply a filter to the $\tilde{S}_i$ variable in the NS simulations on cubed spheres.

Table 2.2: The radial grid structures used for the 3D neutron star simulations. For each grid, for each region, the location and curvature of the surfaces that bound the cubed sphere elements are given. Duplicated information is omitted: the missing regions of S2 are identical to those of S1.

		x_i	c_i	N_r
S1	trans.	1.3, 1.9, 2.5	0.55, 0.85, 1	4
	int.	2.5, 3.0, 3.6, 4.33, 5.2, 6.24, 7.5	1	4
	surf.	7.5, 7.75, 8, ..., 9.5, 9.75, 10	1	1
	ext.	10, 12, 15, 18, 21, 24	1	3
S2	surf.	7.5, 8, 8.5, 9, 9.5, 10	1	2
S1R	trans.	(see S1)	(see S1)	5
	int.	(see S1)	(see S1)	5
	surf.	7.5, 7.625, 7.75, ..., 9.875, 10	1	1
	ext.	(see S1)	(see S1)	4

The filter we apply takes the form (2.31). In the central rounded cube, and in the cube-to-sphere transition shells, the instability is well controlled by a filter with $\alpha = 0.03$ and $s = 2$, or

$$F(i) = \exp\left(-0.03(i/N)^2\right). \tag{2.58}$$

In the spherical shells, the instability is more slowly growing, so is controlled by a weaker filter with $\alpha = 0.01$ and $s = 2$. These filters on $\tilde{S}_i$ are simultaneously broad, in the sense that many modes are damped, but weak, in the sense that the filters damp these modes over long timescales of hundreds of $M_\odot$. The filters' effect is to drive the $\tilde{S}_i$ values on each element towards their mean, effectively reducing the order of the scheme for this particular variable. The stars presented in this paper have a rest state with no velocity, i.e. $\tilde{S}_i = 0$, and the dynamics consist entirely of short-timescale oscillations while the system settles to the rest state. The filters therefore have negligible effect. For stars undergoing prolonged dynamics (e.g. tidal effects in an orbit) or rotation, the use of our filters should not qualitatively affect the results, but would reduce the method's order of

convergence.

In contrast to the filters normally used in spectral methods, the filters we use are *extremely* mild. A more typical filter might have $\alpha = 36$ and $s = 16$, with the effect of setting the top mode (or few modes) to roundoff. This stronger filter is designed for use on high-resolution grid where the top few modes might alias. Since the instability we aim to control is slowly growing, and since we use low-order elements, we find best results with the broad and weak filter described here.

While filtering is able to control the instability, another possibility would be to better resolve the quadratures in the integration of (2.11), and therefore reduce the aliasing problem. This could be done by one of,

1. More numerous, smaller elements, which will better resolve the curvature of the grid.
2. Higher-order elements, for which the error introduced by the inexact quadratures will be reduced and for which less broad filtering can be used. These elements do not perform well at the star's surface, however, so need to be used with mesh refinement.
3. The use of an exact quadrature in deriving the DG method. This technique would be be most effective for low-order elements, where the extra order of accuracy gained in the quadrature will be more significant.

CHAPTER 3

WHAT DOES A BINARY BLACK HOLE MERGER LOOK LIKE?

We present a method of calculating the strong-field gravitational lensing caused by many analytic and numerical spacetimes. We use this procedure to calculate the distortion caused by isolated black holes and by numerically evolved black hole binaries. We produce both demonstrative images illustrating details of the spatial distortion and realistic images of collections of stars taking both lensing amplification and redshift into account. On large scales the lensing from inspiraling binaries resembles that of single black holes, but on small scales the resulting images show complex and in some cases self-similar structure across different angular scales.

3.1 Introduction

Black holes are the most compact gravitating objects in the universe, with such strong gravitational fields that not even light can escape them. In the vicinity of a black hole, light rays can be very strongly deflected from a straight-line path, sometimes orbiting around the black hole before continuing on their way. It is now well-known that the bending of light by massive objects like galaxy clusters can create brightness amplification [63], deformed images, or even multiple images [64] of background objects such as quasars. These signatures have so far only been directly observed in cases where the deflection of light is very slight, up to approximately 11 arc seconds [65, 66]. However, here we are interested in the lensing effects associated with much more extreme bending of light near single or binary black holes, where the deflection angle is unbounded.

The lensing effects near general-relativistic bodies were first studied in the 1970s, with Cunningham and Bardeen [67] looking at a star on an orbit in a Kerr spacetime, and Luminet [68] studying an accretion disk around a Schwarzschild black hole. More recently, open-source codes such as GYOTO [69] and GeoViS [70] have produced images of lensing in the neighborhood of various compact objects. While the lensing caused by an isolated black hole has been understood analytically, the case of lensing by a binary black hole (BBH) is much more challenging because of the difficulty of solving for the geometry of the spacetime. With some arguably unrealistic assumptions (e.g., two maximally charged black holes in static equilibrium), analytic solutions can be found and subsequently used for lensing [71, 72, 73, 74, 75, 70].

For astrophysically relevant binaries, however, we must instead rely on numerical solutions. Solving these binary spacetimes numerically to high accuracy has been possible for the last decade (see [77, 78] for a review), motivated by the need to provide gravitational-wave templates used by experiments such as LIGO, VIRGO, and KAGRA to make detections. By using the spacetimes computed in such simulations, we gain the ability to solve for the lensing effects in BBH systems.

In this paper, we focus on the question of what an observer in the vicinity of a BBH would actually *see* as the black holes orbit, spiral inward, and merge, with an example shown in figure 3.1. This is in contrast to most BBH visualizations, in which the positions or horizons of the two black holes are simply shown as a function of time in some coordinate system. We instead compute the paths of light rays that enter the observer's eye or camera to find what would actually be seen. Furthermore, this path must be computed in the fully time-dependent

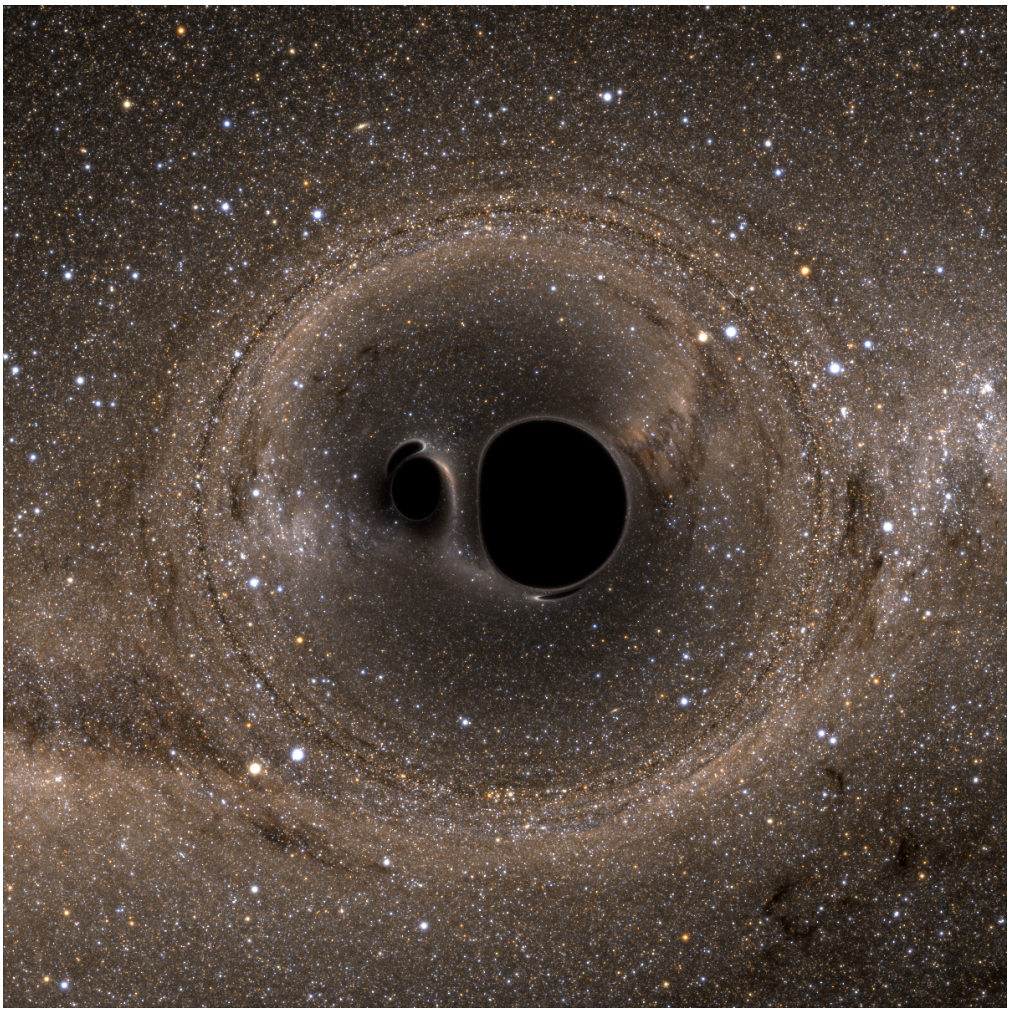

Figure 3.1: A pair of black holes that are about to merge, with the Milky Way visible in the background. Supplementary images and movies can be found at [76].

spacetime, as the orbital velocities for a black-hole binary are typically large enough that the system cannot be approximated as time-independent during the time taken by the photons to travel across it.

Because the black holes themselves do not emit light (we ignore Hawking radiation, which is significant only for microscopic black holes), the observer would see nothing unless there is some additional light source. For illustrative purposes, we will take an artificial background "painted on" at infinity (figure 3.3)

as the light source for most of our examples; this will allow us to study in detail where each light ray originates.

We begin by describing the problem setup and the methods that we use to generate lensing images in section 3.2. In section 3.3 we show images of lensing by single and binary black holes, and we then conclude in section 3.4.

3.2 Methods

We set up the problem with our black hole(s) near the center of our chosen coordinate system. While any physical system representable by a spacetime metric can be used, we specialize in this paper to single and binary black holes. The observer (henceforth taken to be a camera) can be located anywhere in the space and is typically chosen to look towards the origin. A sphere with our light source encloses the black hole(s) and camera, infinitely far away.

To recreate the image taken by the camera in this configuration, we must find the properties of the light that arrives at each point on the camera's image plane. A naïve approach would be to trace all possible light rays (i.e., null geodesics) emanating from the light source to determine which rays reach the camera and from what directions they arrive, but this is computationally infeasible. A more efficient approach is to reverse the problem by tracing light rays away from the camera and *backwards* in time (the computer graphics community calls this a ray-casting algorithm). This method identifies the origin of any light ray that illuminates the camera, from which we infer the color and intensity of the corresponding photons as detected by the camera. When black holes are present, some of the null geodesics traced backwards in time from the camera

may approach arbitrarily close to an event horizon as $t \to -\infty$; these geodesics correspond to dark image regions.

In what follows we describe how the light rays are traced from the camera using the geodesic language from general relativity. We show how we initialize these geodesics based on camera parameters such as position and viewing angle. Finally, we show how the origin of each light ray is determined and describe how the simulated image is constructed.

3.2.1 Geodesic tracing

Our code can trace geodesics independently through either numerical or analytic metric data. It is common for numerical simulations to use the 3 + 1 decomposition [79], so we express the metric in the form

$$ds^2 = -\alpha^2 dt^2 + \gamma_{ij}(dx^i + \beta^i dt)(dx^j + \beta^j dt), \tag{3.1}$$

where α is the lapse function, β^i is the shift vector, and γ_{ij} is the spatial metric.[1] We obtain numerical data from simulations performed using the Spectral Einstein Code (SpEC) [29, 80, 30, 31, 81]. The geodesics are traced by evolving a solution to the geodesic equation

$$\frac{d^2 x^\lambda}{d\tau^2} + \Gamma^\lambda{}_{\mu\nu} \frac{dx^\mu}{d\tau} \frac{dx^\nu}{d\tau} = 0, \tag{3.2}$$

where x^λ is the four-position of the geodesic, τ is an affine parameter, and $\Gamma^\lambda{}_{\mu\nu}$ are the Christoffel symbols describing the effective force caused by spacetime curvature.

[1] Our convention is that Greek indices, as in x^λ, denote temporal or spatial components, while Latin indices, as in x^i, denote only spatial components.

To facilitate the numerical geodesic evolution, we split this second-order differential equation into two first-order differential equations using an intermediate, momentum-like variable such as $p^\lambda = dx^\lambda/d\tau$. As we have some freedom in the definition of this momentum variable, we look for one that helps to minimize computational time and numerical errors when evolving through spacetimes with black holes.

We initially explored using the variable $p_\lambda = g_{\lambda\kappa}p^\kappa$ from Hughes *et al.* [82], along with converting the evolution equations from affine parameter τ to the coordinate time t of SpEC evolutions through the use of $p^0 = dt/d\tau$. Although the resulting evolution equations are concise and have no time derivatives of metric variables, the variables p^0 and p_i grow exponentially near black hole horizons in typical coordinate systems used by SpEC simulations. This forces our time-stepper to take prohibitively small steps in order to achieve the desired accuracy.

We therefore choose a momentum variable slightly different than p_λ to mitigate this time-stepping problem. Null geodesics satisfy $p \cdot p = 0$, which can be rewritten as $p^0 = \alpha^{-1}(\gamma^{ij}p_i p_j)^{1/2}$ using the metric (3.1). This expression shows that p^0 and p_i scale similarly, so we can eliminate the exponential behavior of these variables by evolving the ratio. Our intermediate variable thus becomes

$$\Pi_i \equiv \frac{p_i}{\alpha p^0} = \frac{p_i}{\sqrt{\gamma^{jk}p_j p_k}}, \tag{3.3}$$

where we also divide by α to reduce the number of terms in the resulting evolution equations. Using Π_i and the 3 + 1 decomposition (3.1), we can express the

geodesic equation (3.2) in the form

$$\begin{aligned}\frac{d\Pi_i}{dt} = & -\alpha_{,i} + (\alpha_{,j}\Pi^j - \alpha K_{jk}\Pi^j\Pi^k)\Pi_i \\ & + \beta^k{}_{,i}\Pi_k - \frac{1}{2}\alpha\gamma^{jk}{}_{,i}\Pi_j\Pi_k, \\ \frac{dx^i}{dt} = & \alpha\Pi^i - \beta^i,\end{aligned} \tag{3.4}$$

where K_{jk} is the extrinsic curvature (see, e.g., [79]) and Π^i is defined via the inverse spatial metric as $\Pi^i \equiv \gamma^{ij}\Pi_j$. Note that the geodesic equation consists of four second-order equations, yet we only have three pairs of coupled first-order equations in (3.4). Because we are evolving a normalized momentum (3.3), we have lost information about p^0 during evolution. Compared to Hughes *et al.* [82], we have introduced a time derivative of the three-metric inside K_{jk}, but we have significantly sped up the evolution near black holes by removing the exponential growth of p^0 and p_i.

The equations in (3.4) are similar to those in (28) of Vincent *et al.* [83]. In fact our intermediate evolution variable Π_i is related to their variable V^i by the three-metric, such that $\Pi^i = V^i$. But our (3.4) has a reduced number of both temporal and spatial derivatives of metric quantities compared to Vincent's (28).

During the backwards-in-time geodesic evolution, many geodesics are traced until they are far from the strong-field region, but some are traced until they encounter a black hole. These latter geodesics slowly converge towards the black hole's event horizon, but as they can in principle be evolved indefinitely, we need some way of identifying them in finite time. We do this by monitoring p^0 for each geodesic, which (as discussed above) grows large near black hole horizons. Since our evolution equations (3.4) do not evolve p^0, we must evolve another equation to keep track of it. However, we would still like to avoid the exponential growth of p^0 near the horizon. This can be accomplished by evolving the logarithm of

p^0. As was done in (3.3), we multiply p^0 by the lapse to reduce the number of terms in the resulting equation, which gives the evolution variable $\ln(\alpha p^0)$. This leads to the evolution equation

$$\frac{d\ln(\alpha p^0)}{dt} = -\alpha_{,i}\Pi^i + \alpha K_{ij}\Pi^i\Pi^j. \tag{3.5}$$

When p^0 becomes too large, signaling a large energy, we flag the geodesic as originating from the black hole and we stop evolving it.

The remaining geodesics are those that originate from infinity, so we need to determine the (θ,ϕ) location at infinity where they come from. In section 3.2.3, we will need the gravitational redshift z of each photon, which can be calculated from the ratio of the photon's energy at the two ends of its trajectory via

$$1 + z = \frac{E_\infty}{E_{\text{camera}}}, \tag{3.6}$$

where E_∞ is the photon's energy at infinity, and E_{camera} is the photon's energy as measured by the camera. Therefore we will need to compute the energy that each photon would have at infinity. In practice, these geodesics are traced backwards in time until they reach a large distance R from the black hole(s), chosen so that the metric at R is equal to the flat space metric within about a percent error. We use the approximation that the metric is exactly flat for $r > R$. Under this approximation, the geodesic's direction and p^0 at infinity are the same as at R. The direction is used to calculate a (θ,ϕ) location on the sky, while p^0 is the photon's energy at infinity, E_∞.

3.2.2 Initial data

Here we outline how we initialize our geodesic evolution variables. Because the geodesics are traced away from the camera, backwards in time, we initialize each geodesic's evolution variables to their values at the camera. We have seven variables to set: three each for the initial position and momentum in (3.4), and one for the initial redshift in (3.5).

The initial position for every geodesic is simply the camera's position. The initial momentum, however, is different for each geodesic and is dependent on the angle at which it enters the camera. We express the momenta in terms of an orthonormal tetrad defined as

- e_0**:** The camera's four-velocity, a timelike vector. For stationary cameras $e_0 \propto (1, 0, 0, 0)$;
- e_1**:** The direction in which the camera is pointing;
- e_2**:** The "upward" direction for the camera;
- e_3**:** The "rightward" direction for the camera.

The four-vectors e_1, e_2, and e_3 are all spacelike, and their orientations in the camera's reference frame are illustrated in figure 3.2.

In order to specify this tetrad, we give guesses for the vectors e_0, e_1, and e_2, with the condition that the guessed time components of e_1 and e_2 must be zero. We then apply the Gram-Schmidt process to the sequence e_0, e_1, and e_2 to transform these vectors into an orthonormal set. The final vector, e_3, is found by calculating the generalized cross product of the other three; explicitly,

$$e_{3\rho} = \epsilon_{\lambda\mu\nu\rho} e_0{}^{\lambda} e_1{}^{\mu} e_2{}^{\nu}, \tag{3.7}$$

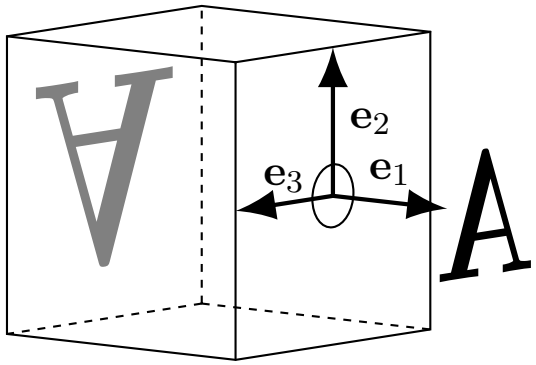

Figure 3.2: Illustration of a pinhole camera in its rest frame with the three vectors e_1, e_2, and e_3 that describe its orientation. The inverted letter "A" demonstrates the optical properties of the camera, which we correct for in the images we generate.

where $\epsilon_{\lambda\mu\nu\rho}$ is the Levi-Civita tensor (see [52, p. 202] for more details).

Given the four orthonormal unit vectors, we can construct a null vector ξ tangent to the geodesic that enters the camera from a given direction. The vector ξ will be proportional to the four-momentum of a photon following the geodesic; that is, $p = q\xi$ for some positive constant q. We define ξ by

$$\begin{aligned} \xi^{\lambda}{}_{(a,b)} = C{e_0}^{\lambda} - {e_1}^{\lambda} - [(2b-1)\tan(\alpha_v/2)]{e_2}^{\lambda} \\ - [(2a-1)\tan(\alpha_h/2)]{e_3}^{\lambda}, \end{aligned} \tag{3.8}$$

where $a, b \in [0, 1]$ give the ray's arrival direction in terms of fractions of the image's horizontal and vertical lengths, respectively, and α_v, α_h are the angular sizes of the camera aperture (field of view angles) in the vertical and horizontal directions. For the sign convention chosen in (3.8), $(a, b) = (0, 0)$ corresponds to a photon seen at the bottom left corner of the image. We find C by requiring that ξ is null, i.e., $\xi \cdot \xi = 0$:

$$C = \sqrt{1 + (2b-1)^2\tan^2(\alpha_v/2) + (2a-1)^2\tan^2(\alpha_h/2)}. \tag{3.9}$$

We then use the metric to lower the index on ξ, and we compute the initial value of our evolution variable Π_i using $\Pi_i = p_i/(\alpha p^0) = \xi_i/(\alpha\xi^0)$. Note that Π_i is

independent of the proportionality constant q relating ξ and the actual photon momentum p; physically, this is because the photon trajectory is independent of the photon energy. The only place where q enters is in the initial value of αp^0 in (3.5). We fix the value of q by demanding that the energy of the photon in the frame of the camera be unity when the photon strikes the camera, so $E_{\text{camera}} = 1$ in (3.6).

3.2.3 Image generation

We create our image of the physical system by dividing the image plane into rectangular regions corresponding to the pixels of the output image and assigning an appropriate color to each region. Because each region has an extended size, there is no single source point we can look at to obtain its color, so we must adopt some prescription for assigning a single color to each pixel. We use two different prescriptions, based on the nature of the light source illuminating the system.

For extended sources, such as the artificial grid in figure 3.3, we use a subpixel sampling method. On each pixel we construct an evenly spaced grid of points, and at each of these points we determine where incident light rays originate, either from one of the holes or a location at infinity. We assign a color to each grid point based on that of the corresponding source point; the color of the pixel is then the average of these. We find that a grid of 4×4 sample points gives sufficiently smooth images without too much computational cost. For these images, we neglect the effects of redshift and focus on the spatial distortions.

To create more astronomically relevant images, we wish to use a collection of point sources (i.e., stars) as our illumination. In this case we cannot determine

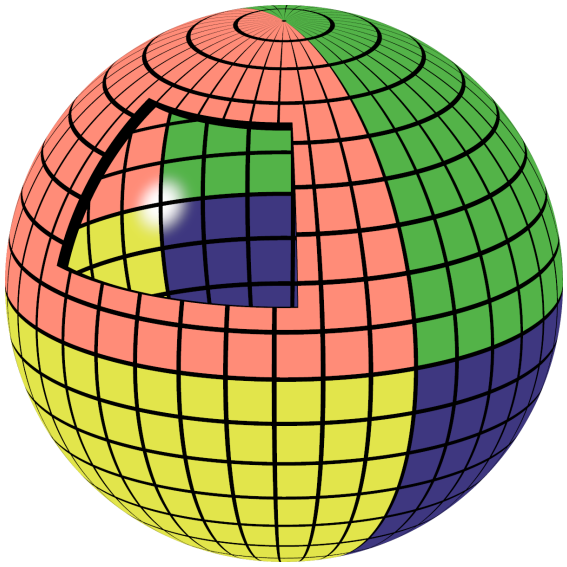

Figure 3.3: An illustration of our artificial background grid "painted on" a sphere at infinity. This background is used for all the images with a grid in this paper. In the figure, we cut a window out of the sphere to show the inside. In addition to four colors differentiating the regions of the sphere, we include a white reference spot in the direction in which the camera is pointing.

a pixel's color using sampling, but must instead sum the contributions from all the point sources contributing light there. For our list of sources, we use about 3.4×10^8 stars from the Two Micron All Sky Survey (2MASS) [84]. To simplify computations, we approximate each star as a thermal source with temperature and brightness determined by fitting to the photometric information in the catalog. When we calculate the contribution of each star to the light arriving at the camera, we must account not only for its properties as a light source, but also for the effects of the spacetime curvature encountered by the photon. These effects come in two forms. First, the observed energies of photons at the camera will be modified by redshift effects, changing sources' apparent brightnesses and temperatures. Second, the spatial convergence or divergence of nearby geodesics produces an overall adjustment to each source's apparent brightness without affecting its spectrum. Both of these effects are discussed in detail in

Mollerach and Roulet [85]. After we have drawn the entire image in this manner, we convolve it with a blurring function to make the stars more visible. This has the effect of transforming each star into a fuzzy circle with size dependent on its brightness.

The result of this scheme can be seen in figure 3.1, which shows the BBH image from figure 3.11 in front of a background of stars. Note that by generating our starfield images from a catalog of point sources, we obtain a substantially more realistic image than would be generated by applying the lensing deformation to a raster image of the unlensed Milky Way stars. In such a raster image, each star is usually represented (whether as a result of camera optics or software rendering) as a blurred circle whose area depends on the star's brightness. These circles are typically hundreds of arc seconds wide, and therefore lensing distortions applied to the image tend to produce stars that appear as smeared ellipses. In contrast, the angular sizes of real stars are many orders of magnitude smaller, so we expect them to remain as unresolved points under all but the most extreme lensing magnifications. These unresolved points can then be rendered as previously described, giving stars that better portray what an observer would actually see (as in figure 3.1). The difference between these methods lies in the non-commutativity between the lensing deformations and the blurring of each star. A minor shortcoming of our method arises at Einstein rings (discussed in section 3.3.1), where the magnification diverges. There a star could in principle (though with very low probability) appear as an extended object, but in our treatment it would remain point-like. On the other hand, blurring first and then lensing is almost guaranteed to produce unphysical extended streaks at the Einstein ring.

3.3 Results

Before applying our lensing code to binary black hole systems, we generate images of simpler analytic spacetimes. These serve both to provide checks that our images are consistent with earlier work, and also to illustrate general features of lensing around black holes that will appear again in BBH images. We then proceed to show two different configurations of BBH mergers.

To help visualize the lensing, we divide our light source at infinity into colored quadrants with a superimposed grid. An external view of this sphere is shown in figure 3.3. In addition to the colored sections, our light source has a bright reference spot in the direction towards which we point our camera. This spot will prove useful in illustrating an important feature of black hole lensing called an Einstein ring.

3.3.1 Analytic spacetimes

In figure 3.4, we compare a flat space image with the images obtained by lensing our light source through Schwarzschild and Kerr black hole spacetimes. The top row from left to right shows flat Minkowski space and a Schwarzschild black hole. These spacetimes are spherically symmetric, so viewing them from different angles produces the same lensing effects. The bottom row shows a Kerr black hole, where in the left frame the spin vector is pointing out of the page and in the right frame it is pointing up. Here the spin breaks the spherical symmetry of the spacetime, leading to different lensing effects from different viewing directions.

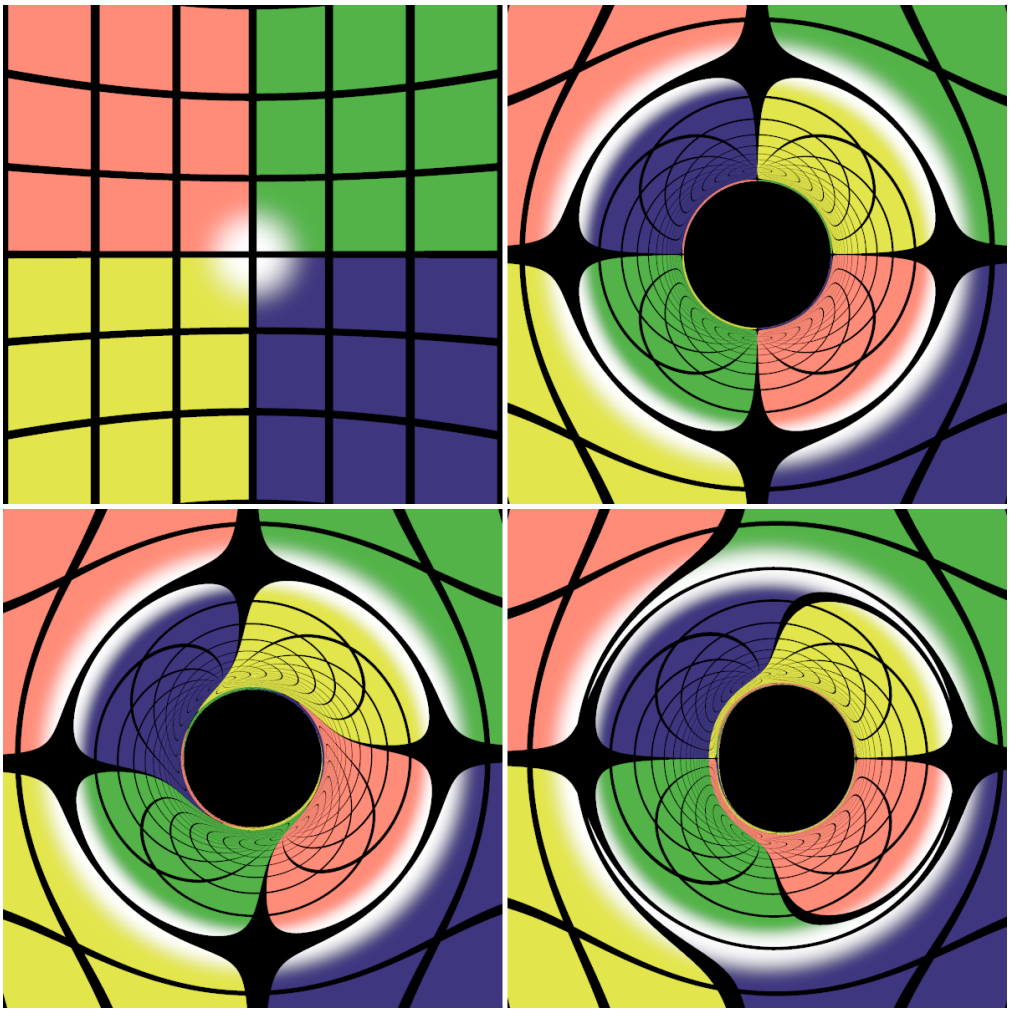

Figure 3.4: Lensing caused by various analytic spacetimes. For all panels, we use figure 3.3 as a background, oriented such that the camera is pointed at the white reference dot. The camera has a 60° field of view and is at a distance of 15 Schwarzschild radii from the origin measured using Kerr-Schild coordinates [52]. The top row shows Minkowski and Schwarzschild spacetimes. The bottom row shows two views of the Kerr spacetime, with dimensionless spin $\chi = 0.95$, viewed with the camera pointing parallel to the spin axis of the black hole (bottom left) and perpendicular to the spin axis (bottom right).

In Minkowski space in the top left image we expect no deflection of light, which is what we observe. The camera sees an upright image of the portion of the grid near the white dot. The bowing of the grid lines is an expected geometric effect of viewing a latitude-longitude grid.

In the top right image, we see the lensing effects of a non-spinning black hole. The black circle in the center of the image is called the shadow of the black hole, where the hole prevents any light from reaching the camera. Alternatively, a shadow is a region of the image where geodesics are traced backwards in time from the camera to a black hole. Another prominent feature is that the white dot on our grid at infinity has been lensed into a large ring, called an Einstein ring [86]. Light from the point situated directly on the opposite side of the black hole, the antipodal point, will by symmetry be lensed into a ring around the black hole as observed by our camera. Regions inside the Einstein ring correspond to photons that are deflected by larger angles than are the Einstein ring photons; this results in an inverted image of the reference grid inside the Einstein ring. A second Einstein ring can be seen near the shadow, corresponding to light from a source behind the camera wrapping around the hole on its way to the camera. In fact, photons can wind an arbitrarily large number of times around the black hole, resulting in an infinite number of Einstein rings.

The bottom row of figure 3.4 shows a single black hole with a large dimensionless spin of $\chi = 0.95$. As in the Schwarzschild case, there is an Einstein ring around the black hole shadow as well as image inversion inside the Einstein ring. However, for the case of a Kerr spacetime, the light coming from the Einstein ring does not originate from a single point directly behind the black hole, but from a small region (unless the camera is pointing directly along the spin axis). The spin of the black hole causes frame dragging, where space is dragged in the direction of the rotation [87, 88]. In the bottom left image, the spin axis of the black hole is pointing out of the page, so space is dragged in a counterclockwise motion. The effect of the frame dragging on the photon trajectories produces an image in which the grid itself appears to be dragged by the spin, as is evident when

compared to the non-spinning black hole in the top right image. The strength of frame dragging increases closer to the black hole, which can also be inferred from the deformation of the background grid.

Frame dragging manifests differently in the bottom right image, where the spin axis is pointing up. The direction of frame dragging is out of the page on the left of the shadow of the black hole and into the page on the right. A photon traveling in the direction of the frame dragging can orbit closer to the black hole without being captured than a photon traveling opposite the frame dragging direction, resulting in an asymmetrical shadow about the spin axis. This causes the shadow to appear offset relative to the shadow of a Schwarzschild hole.

3.3.2 Binary black hole spacetimes

Astrophysical black hole binaries are expected to radiate energy via gravitational waves, leading to a long inspiral followed by a merger, and finally a ringdown to a steady-state single black hole. Lensing by a final, steady-state black hole will look like the single black holes already seen in figure 3.4. However, the situation becomes more interesting when viewing these systems before merger. The first images we will present show an equal-mass BBH with non-spinning black holes—one of the simplest binary inspiral spacetimes to analyze—shortly before merger. The simulation we use is case 1 of Taylor *et al.* [89].

Figure 3.5 shows the image of our reference grid in the presence of this BBH, where the camera is situated such that the orbital angular momentum is pointing out of the page. This image bears a striking resemblance to the bottom left frame of figure 3.4, excluding the details near the shadows. This shows that, away from

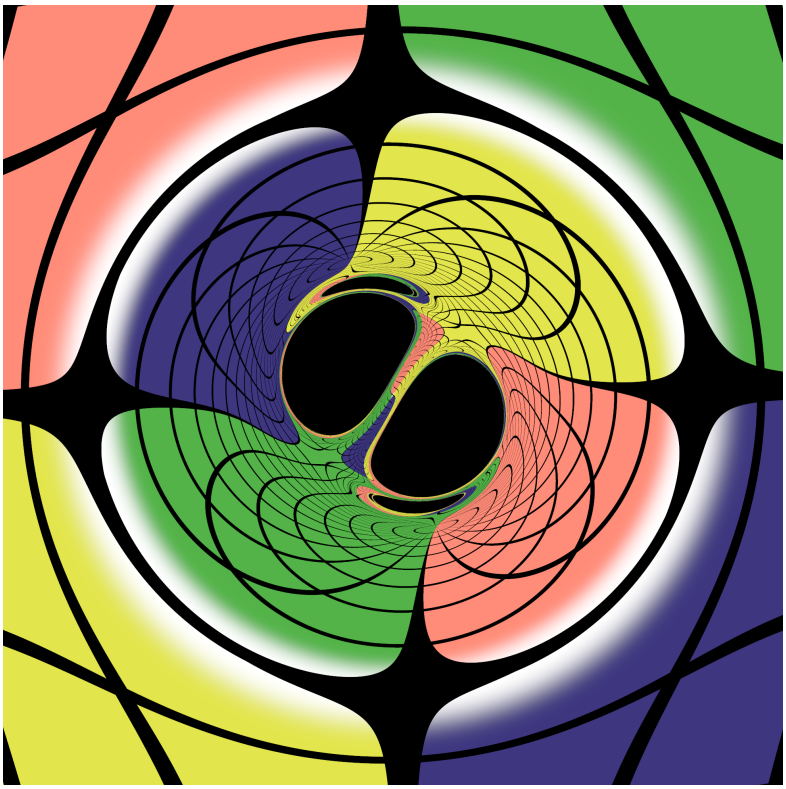

Figure 3.5: A BBH system of equal-mass black holes with no spin, viewed near merger with the orbital angular momentum out of the page.

the shadows, the spacetime looks similar to a single rotating black hole, where the lensing is dominated by the mass monopole with corrections caused by the angular momentum of the system. In the single-hole case, the spin is responsible for frame dragging, whereas here the orbital angular momentum is responsible.

Focusing on the inner portion of the image, we observe that the binary lensing is markedly different from the Schwarzschild or Kerr cases. Figure 3.6 shows a cropped version of figure 3.5, emphasizing the structure of the shadows. As might be expected, there are two prominent shadows visible, each associated with one of the two black holes. We also see a narrow secondary shadow (an "eyebrow" [75]) close to the outside of each primary shadow. These secondary shadows correspond to one black hole (BH) casting a shadow which is lensed

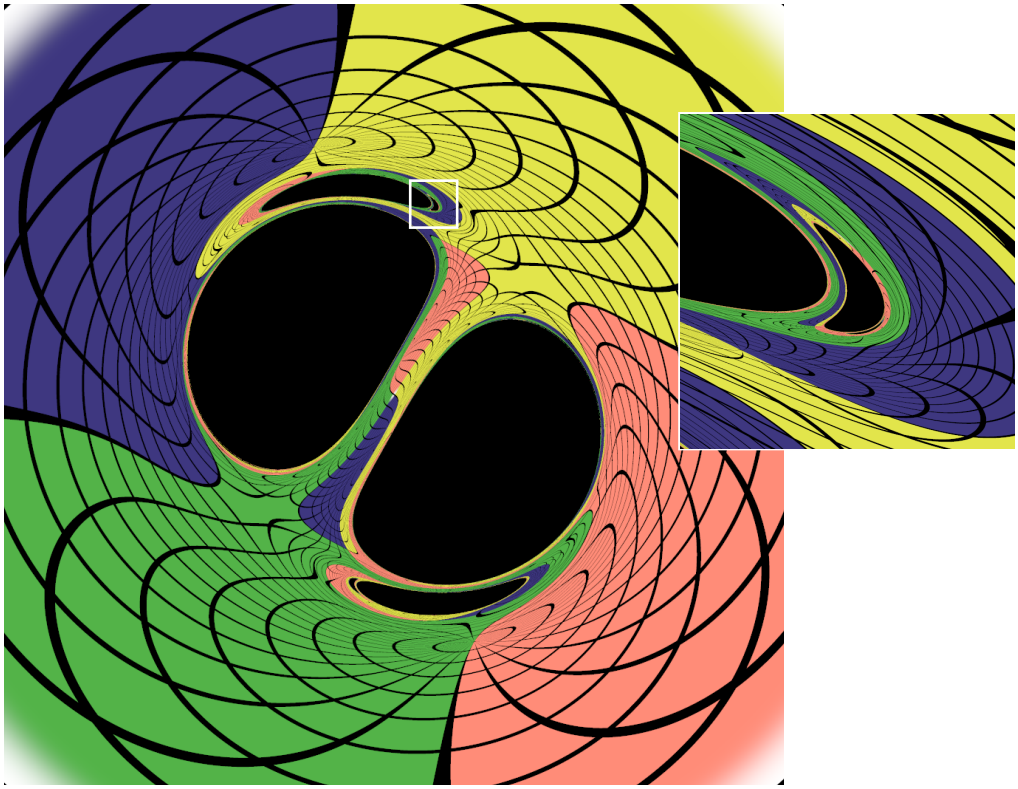

Figure 3.6: A cropped version of figure 3.5 in order to show more detail near the black hole shadows. A small portion of the image (outlined) is enlarged and inset, where a smaller eyebrow is clearly visible.

by the other BH on the way to the camera. Equivalently, they are image regions where geodesics are traced backwards from the camera to a BH, but bend around at least one BH on the way there. The first pair of eyebrows is evident in figure 3.6; however, we can resolve a pair of smaller eyebrows, shown in the inset.

We show another view of the same system in figure 3.7. Here the camera is looking at the system edge on, such that the orbital angular momentum is pointing up. We see again an overall similarity with the corresponding orientation of Kerr spacetime (the bottom-right frame of figure 3.4), indicating the dominant effects of the mass and angular momentum in these images. We can see a primary shadow for each black hole, but in this configuration one black

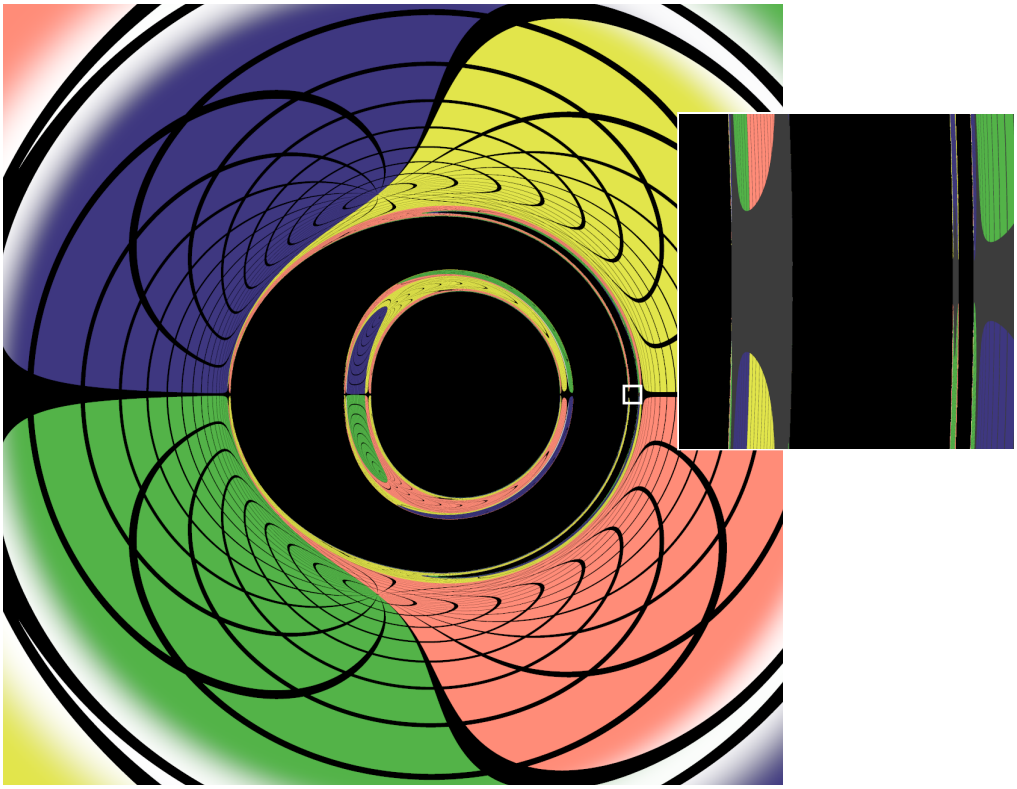

Figure 3.7: The same system as figure 3.6, viewed such that the orbital angular momentum of the system is pointing up. Note that the grid lines in the inset are shown in gray here to distinguish them from the black hole shadows.

hole is located roughly behind the other and as a result its shadow gets lensed into a dark ring. Extending along the right side of this ring we see a long thin eyebrow, which is shown in the inset, along with another, smaller, eyebrow.

To illustrate how photon trajectories behave near shadows, we plot trajectories of a few geodesics on the horizontal line passing through the middle of figure 3.7 near the eyebrow. Figure 3.8 shows four snapshots of these trajectories in time, with their current locations in each frame denoted by large dots. It is easiest to consider these trajectories as we evolve them, out of the camera and backwards in time, to see where they came from. In frames A–C, we see the trajectories under consideration start close together then diverge significantly, demonstrating

how nearby pixels on the image can correspond to vastly different physical locations. In frame D we see the entire trajectories. A few extend to infinity, but most terminate on the black holes; these are denoted by solid lines and dotted lines, respectively. Only the trajectories extending to infinity result in a photon reaching the camera; those that reach the hole on the right of frame D correspond to the primary ring-like shadow in figure 3.7, while those that reach the left hole correspond to the larger eyebrow visible on the right side of figure 3.7. Note that the black holes are orbiting rapidly, so they move significantly while the photons pass through the system.

We can also uniquely identify which black hole casts each shadow, which enables us to show in figure 3.9 the origin of the photons along the horizontal line across the center of figure 3.7. We arbitrarily label the large shadow in the middle of figure 3.7 as BH 2, and the ring-like shadow as BH 1. Regions where photons reach the camera from infinity are labeled ∞. The top plot in figure 3.9 shows the origin of the photons that reach the camera along the entire middle horizontal line in figure 3.7. We see that each transition from ∞ to either of the BHs includes transitions to the other BH. Even though we cannot resolve them numerically, each vertical line in principle contains infinitely many transitions. To illustrate this idea, the second plot in figure 3.9 investigates the group of shadows indicated by the zoomed inset of figure 3.7. Here we find a structure which resembles the first plot. The third plot in figure 3.9 zooms to a similar group of shadows on the right side of the second plot to again reveal the same structure. This figure clearly shows evidence of self-similarity in the structure of BBH lensing, where the smaller length scales explore more photon orbits through the system. Furthermore, the structure of shadows in BBH lensing is more complex than figures 3.6 and 3.7 appear to suggest. The shadows these

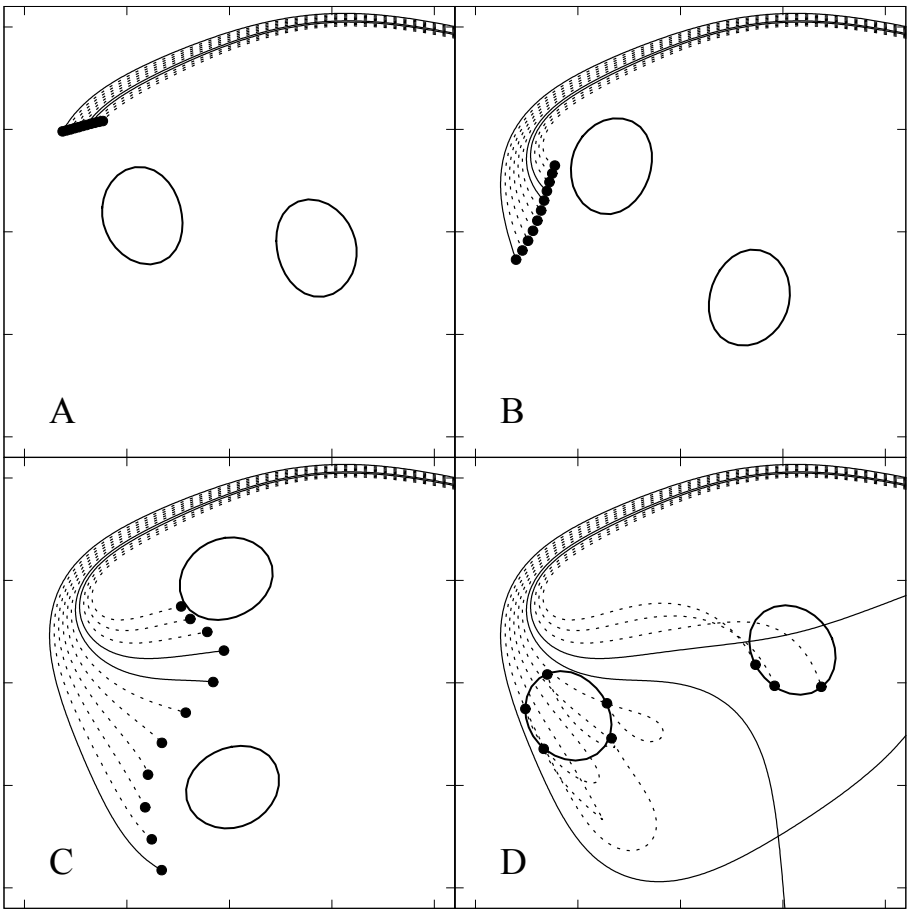

Figure 3.8: Geodesic trajectories plotted in relation to the black hole event horizons during the lensing evolution for figure 3.7. Each frame shows a snapshot in time, with the dots representing the current positions of the geodesics, and the lines indicating the trajectories from the camera. The solid and dashed lines indicate whether the geodesics originate from infinity or from a black hole, respectively.

images focus on are merely some of the largest visible shadows, associated with simpler geodesic orbits around the binary.

If we consider this equal-mass BBH earlier in the inspiral when its separation is large, the black holes are only weakly interacting. Therefore most camera viewpoints of this binary will yield images with two primary shadows, one for

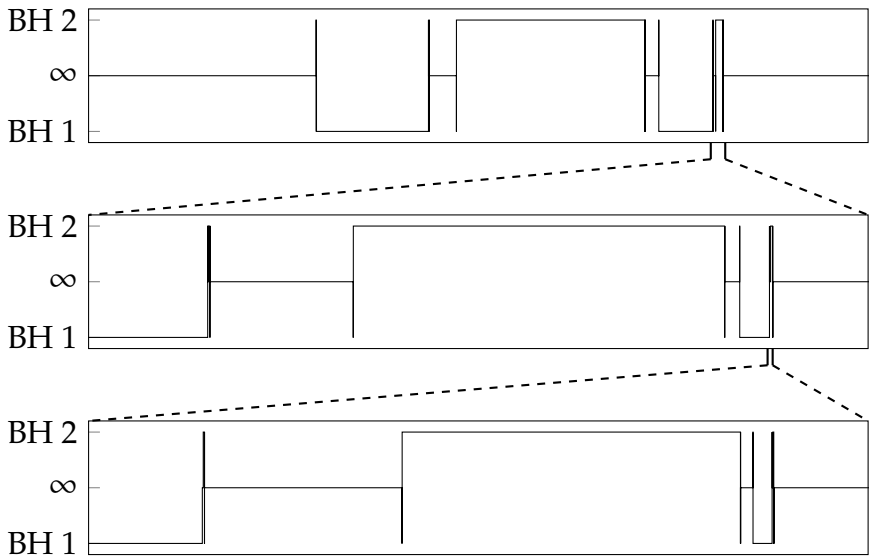

Figure 3.9: Plots identifying the origins of photons along the horizontal line through the center of figure 3.7. Photons coming from infinity are labeled ∞, and the shadows are labeled either BH 1 or BH 2. The first plot corresponds to the main portion of figure 3.7. The second plot focuses on the zoomed square in the inset of figure 3.7, showing a small feature of the first plot. The third plot zooms to a similar feature of the second plot. This figure demonstrates a striking self-similarity of the lensing structure of a binary black hole system.

each black hole. Each shadow will be similar to an isolated Schwarzschild or Kerr shadow but with the addition of small eyebrows. However, when the binary is viewed edge-on and the black holes are nearly aligned with the camera, we see an interesting image.

Figure 3.10 shows the equal-mass binary in this configuration, hundreds of orbits before merger. Just as in figure 3.7, the more distant black hole is lensed into a ring-like shadow; however, the ring is thinner here, primarily because of the large separation of the binary. The angular momentum causes the lensed grid outside the shadows to strongly resemble lensing by a Kerr black hole rather than lensing by a Schwarzschild black hole. In addition to the usual primary Einstein ring, another ring is visible between these shadows. Both of these rings

correspond to the same source of light, which is in front of the camera and behind the BBH. The second Einstein ring is caused by photons following an "S"-shaped trajectory through the system.

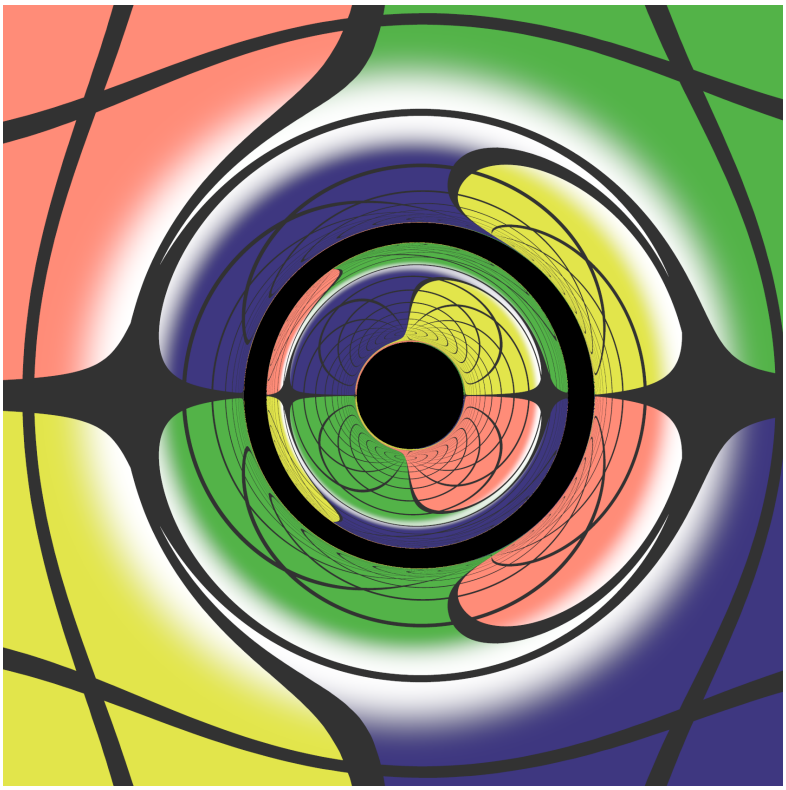

Figure 3.10: A BBH system of equal-mass black holes with no spin, viewed hundreds of orbits before merger, with the orbital angular momentum pointing up. The distance from the camera to the closer black hole in this figure is the same as in figure 3.7. Note that the grid lines are shown in gray here to distinguish them from the black hole shadows.

The second binary system we consider is a fully generic black hole binary with a mass ratio of $m_1/m_2 = 3$ and black hole spins of $\chi_1 = 0.7$ and $\chi_2 = 0.3$ in arbitrary directions. This is case 4 of Taylor *et al.* [89]. In figure 3.11 we see a top view of this system, in analogy with what is presented in figure 3.6. Away from the shadows, the lensing is similar to a single black hole with spin, as was seen with the equal-mass binary images. This appears to be a generic feature of lensing from orbiting BBHs. We can clearly see that the symmetry present in the

equal-mass system is gone. The unequal masses evidently change the relative sizes of not only the primary shadows, but all additional shadows as well. The inset in figure 3.11 zooms to show two successively smaller eyebrows near the small black hole's primary shadow. However, the effects of the black holes' spins are not at all clear from this viewpoint.

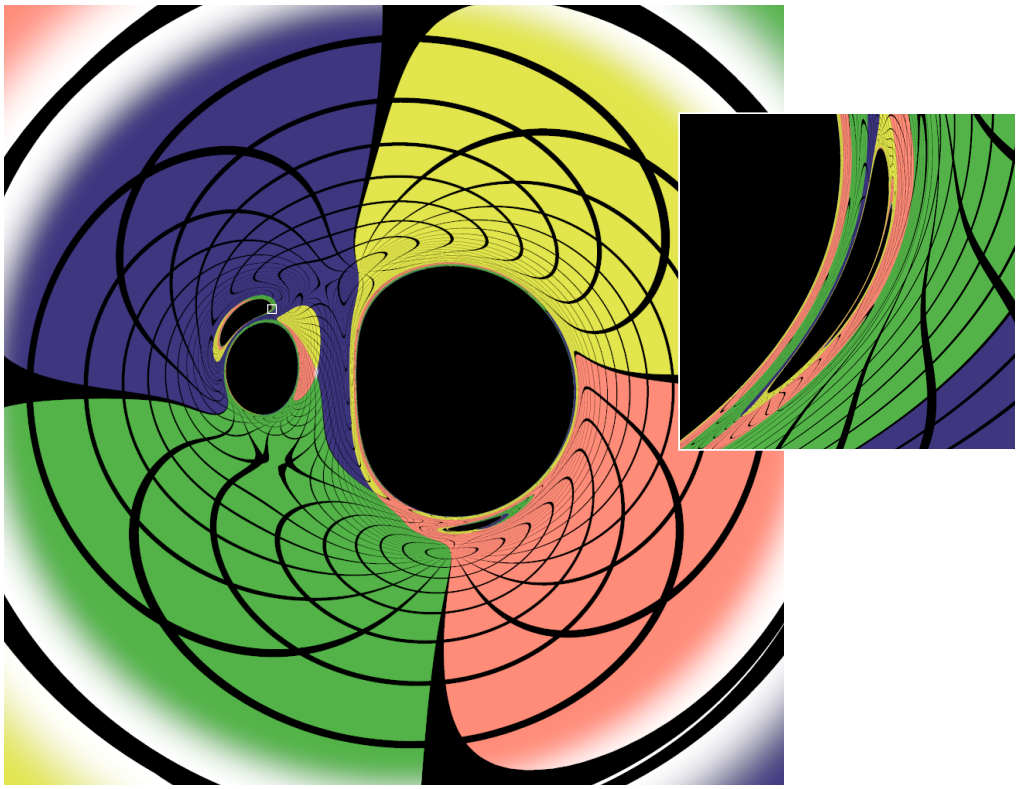

Figure 3.11: A view of a binary inspiral of mass ratio $m_1/m_2 = 3$ near merger, with the orbital angular momentum approximately pointing out of the page. The black hole spins are $\chi_1 = 0.7$ and $\chi_2 = 0.3$ in arbitrary directions. This figure is analogous to figure 3.6. As in previous figures, a small portion of the image is enlarged and inset, displaying additional eyebrows.

In figure 3.12 we see the same binary as in figure 3.11, viewed with the orbital angular momentum pointing upward, in analogy with figure 3.7. We again see that, away from the shadows, the system looks like a Kerr black hole. The unequal mass ratio is apparent here, with the smaller black hole lensing the shadow of the larger black hole into a partial ring. If it were not for the

black hole spins, the lensing by the binary would be symmetric, giving either a ring-like shadow similar to figure 3.7 or a shadow and a very thick eyebrow. In this particular BBH, the effect of the individual black hole spins on the image depends strongly on the camera position.

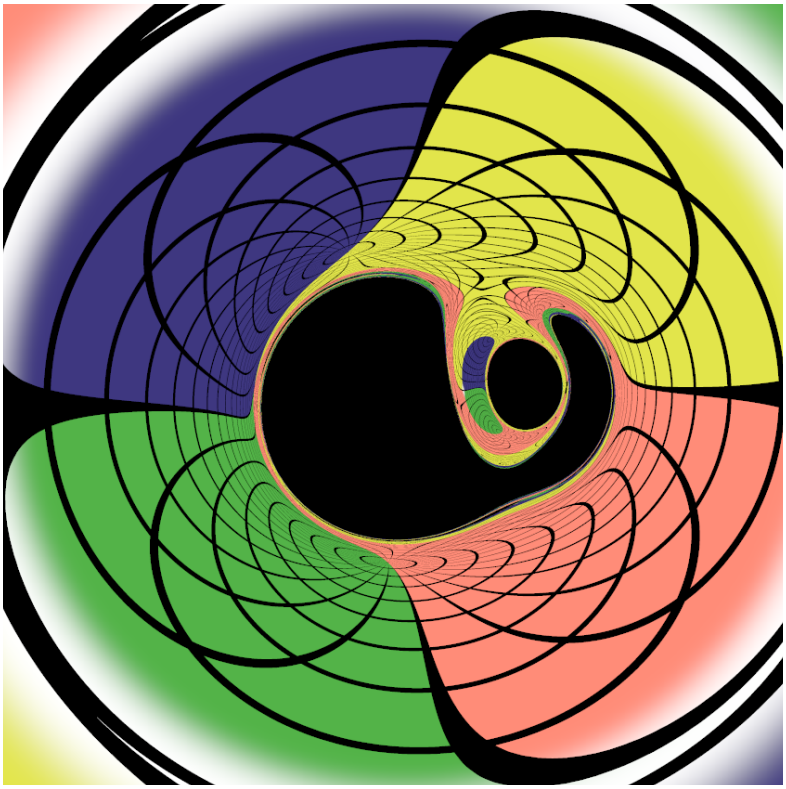

Figure 3.12: Another view of the BBH in figure 3.11, but with orbital angular momentum pointing up. The camera parameters are otherwise identical. This figure is analogous to figure 3.7; however, because of the asymmetry from the black hole spins, the larger black hole's shadow is not lensed completely around the small black hole.

3.4 Conclusions

In this paper, we present the first images of gravitational lensing by astrophysically relevant binary black holes, thereby providing a realistic representation of what an observer near such a system would actually see. To accomplish this, we

have developed a new set of equations that evolve photons efficiently near black hole horizons. Our images show there is a primary shadow—a region where the black hole prevents light from reaching the camera—for each black hole, as well as multiple secondary shadows (or eyebrows).

We have found that, early in the inspiral, images of a BBH look similar to two separate Kerr black hole shadows, unless viewed when the holes are nearly collinear with the camera. Shortly before the merger, all camera angles yield interesting images of not just one shadow for each black hole, but a handful of smaller visible shadows. We showed for an equal-mass binary viewed edge-on that the lensing structure exhibits self-similarity on smaller scales, corresponding to photons taking an increasing number of orbits through the system. Lensing by a fully generic BBH illustrated that the spin of black holes in a binary can have a clear effect on the lensed shadows.

We chose not to classify eyebrows and shadows into a hierarchy in this paper. In the inset of figure 3.6, for instance, identifying the largest eyebrow as the primary eyebrow and the next largest as the secondary eyebrow feels very natural, but the exact definition of such a hierarchy is not immediately clear. For example, simply specifying a geodesic winding number around each black hole is likely not to be sufficient. In addition to the trajectories not lying in a plane, the order that a geodesic orbits the black holes does not commute. Furthermore, the black holes are moving at comparable speeds to the geodesics. For these reasons, we leave the task of classifying shadows as future work.

We have also shown in this paper that, away from the shadows, an image of a binary black hole system looks like that of an isolated black hole. Thus it is necessary to resolve individual shadows in order to discern the unique

visual characteristics present in such images, which places limits on our ability to observe them.

For systems involving matter, however, the combination of the lensing effects of strong gravity with the disruption and distortion of radiation-emitting matter might yield a unique optical signature. Generating lensed images of black hole-neutron star and neutron star-neutron star mergers is an avenue of future investigation. The techniques presented here would allow us to produce detailed visualizations of these mergers; integrating over such images, we could predict the optical signature of an unresolved system.

Acknowledgements

We would like to thank Curran Muhlberger for providing the temperature fits to the 2MASS photometric data. This publication makes use of data products from the Two Micron All Sky Survey, which is a joint project of the University of Massachusetts and the Infrared Processing and Analysis Center/California Institute of Technology, funded by the National Aeronautics and Space Administration and the National Science Foundation. We would like to thank Daniel Hemberger and Saul Teukolsky for comments on an earlier version of this paper. The authors from Cornell would also like to thank Saul Teukolsky and Lawrence Kidder for general advice while writing this paper.

This work was supported in part by NSF Grants PHY-1306125 and AST-1333129 at Cornell University, by NSF Grants PHY-1440083, AST-1333520, PHY-1005655, and DMS-1065438 at the California Institute of Technology, and by a grant from the Sherman Fairchild Foundation. FH acknowledges support by

the NSF Graduate Research Fellowship under Grant No. DGE-1144153. DB acknowledges support from the LIGO Laboratory, with funding from the National Science Foundation under cooperative agreement PHY-0757058 and NSF REU award PHY-1062293. The binary black hole simulations were performed using the Zwicky computer system operated by the Caltech Center for Advanced Computing Research and funded by NSF MRI No. PHY-0960291 and the Sherman Fairchild Foundation.

BIBLIOGRAPHY

[1] A. Bohn, W. Throwe, F. Hébert, K. Henriksson, D. Bunandar, M. A. Scheel, and N. W. Taylor, Class. Quantum Grav. **32**, 065002 (2015), arXiv:1410.7775 [gr-qc] .

[2] B. P. Abbott *et al.* (LIGO Scientific Collaboration, Virgo Collaboration), Phys. Rev. Lett. **116**, 061102 (2016), arXiv:1602.03837 [gr-qc] .

[3] B. P. Abbott *et al.* (LIGO Scientific Collaboration, Virgo Collaboration), Phys. Rev. Lett. **116**, 241103 (2016), arXiv:1606.04855 [gr-qc] .

[4] G. Lovelace, C. O. Lousto, J. Healy, M. A. Scheel, A. Garcia, R. O'Shaughnessy, M. Boyle, M. Campanelli, D. A. Hemberger, L. E. Kidder, H. P. Pfeiffer, B. Szilágyi, S. A. Teukolsky, and Y. Zlochower, Submitted to Class. Quantum Grav. (2016), arXiv:1607.05377 [gr-qc] .

[5] A. Bohé, L. Shao, A. Taracchini, A. Buonanno, S. Babak, I. W. Harry, I. Hinder, S. Ossokine, M. Pürrer, V. Raymond, T. Chu, H. Fong, P. Kumar, H. P. Pfeiffer, M. Boyle, D. A. Hemberger, L. E. Kidder, G. Lovelace, M. A. Scheel, and B. Szilágyi, ArXiv e-prints (2016), arXiv:1611.03703 [gr-qc] .

[6] F. Foucart, Phys. Rev. D **86**, 124007 (2012), arXiv:1207.6304 [astro-ph.HE] .

[7] V. Paschalidis, M. Ruiz, and S. L. Shapiro, Astrophys. J. **806**, L14 (2015), arXiv:1410.7392 [astro-ph.HE] .

[8] M. Ruiz, R. N. Lang, V. Paschalidis, and S. L. Shapiro, Astrophys. J. Lett. **824**, L6 (2016), arXiv:1604.02455 [astro-ph.HE] .

[9] S. M. Couch, E. Chatzopoulos, W. D. Arnett, and F. X. Timmes, Astrophys. J. Lett. **808**, L21 (2015), arXiv:1503.02199 [astro-ph.HE] .

[10] T. Kuroda, T. Takiwaki, and K. Kotake, Astrophys. J. Suppl. Ser. **222**, 20 (2016), arXiv:1501.06330 [astro-ph.HE] .

[11] L. F. Roberts, C. D. Ott, R. Haas, E. P. O'Connor, P. Diener, and E. Schnetter, Astrophys. J. **831**, 98 (2016), arXiv:1604.07848 [astro-ph.HE] .

[12] B. D. Metzger, ArXiv e-prints (2016), arXiv:1610.09381 [astro-ph.HE] .

[13] K. Barkett, M. A. Scheel, R. Haas, C. D. Ott, S. Bernuzzi, D. A. Brown, B. Szilágyi, J. D. Kaplan, J. Lippuner, C. D. Muhlberger, F. Foucart, and M. D. Duez, Phys. Rev. D **93**, 044064 (2016), arXiv:1509.05782 [gr-qc] .

[14] X. Zhong and C.-W. Shu, J. Comput. Phys. **232**, 397 (2013).

[15] J. Zhu, X. Zhong, C.-W. Shu, and J. Qiu, Communications in Computational Physics **19**, 944 (2016).

[16] G. Zumbusch, Class. Quantum Grav. **26**, 175011 (2009), arXiv:0901.0851 [gr-qc] .

[17] S. E. Field, J. S. Hesthaven, S. R. Lau, and A. H. Mroue, Phys. Rev. D **82**, 104051 (2010), arXiv:1008.1820 [gr-qc] .

[18] J. D. Brown, P. Diener, S. E. Field, J. S. Hesthaven, F. Herrmann, A. H. Mroué, O. Sarbach, E. Schnetter, M. Tiglio, and M. Wagman, Phys. Rev. D **85**, 084004 (2012), arXiv:1202.1038 [gr-qc] .

[19] J. M. Miller and E. Schnetter, Submitted to Phys. Rev. D (2016), arXiv:1604.00075 [gr-qc] .

[20] D. Radice and L. Rezzolla, Phys. Rev. D **84**, 024010 (2011), arXiv:1103.2426 [gr-qc] .

[21] J. Zhao and H. Tang, J. Comput. Phys. **242**, 138 (2013).

[22] M. Bugner, T. Dietrich, S. Bernuzzi, A. Weyhausen, and B. Brügmann, Phys. Rev. D **94**, 084004 (2016), arXiv:1508.07147 [gr-qc] .

[23] L. E. Kidder, S. E. Field, F. Foucart, E. Schnetter, S. A. Teukolsky, A. Bohn, N. Deppe, P. Diener, F. Hébert, J. Lippuner, J. Miller, C. D. Ott, M. A. Scheel, and T. Vincent, Submitted to J. Comput. Phys. (2016), arXiv:1609.00098 [astro-ph.HE] .

[24] A. Bohn, L. E. Kidder, and S. A. Teukolsky, Phys. Rev. D **94**, 064009 (2016), arXiv:1606.00436 [gr-qc] .

[25] R. Owen, J. Brink, Y. Chen, J. D. Kaplan, G. Lovelace, K. D. Matthews, D. A. Nichols, M. A. Scheel, F. Zhang, A. Zimmerman, and K. S. Thorne, Phys. Rev. Lett. **106**, 151101 (2011).

[26] D. A. Nichols, R. Owen, F. Zhang, A. Zimmerman, J. Brink, *et al.*, Phys. Rev. D **84**, 124014 (2011), arXiv:1108.5486 [gr-qc] .

[27] `https://www.youtube.com/user/SXSCollaboration` ().

[28] S. A. Teukolsky, J. Comput. Phys. **312**, 333 (2016), arXiv:1510.01190 [gr-qc] .

[29] `http://www.black-holes.org/SpEC.html`.

[30] B. Szilágyi, L. Lindblom, and M. A. Scheel, Phys. Rev. D **80**, 124010 (2009), arXiv:0909.3557 [gr-qc] .

[31] D. A. Hemberger, M. A. Scheel, L. E. Kidder, B. Szilágyi, G. Lovelace, N. W. Taylor, and S. A. Teukolsky, Class. Quantum Grav. **30**, 115001 (2013), arXiv:1211.6079 [gr-qc] .

[32] M. D. Duez, F. Foucart, L. E. Kidder, H. P. Pfeiffer, M. A. Scheel, and S. A. Teukolsky, Phys. Rev. D **78**, 104015 (2008), arXiv:0809.0002 [gr-qc] .

[33] F. Foucart, R. Haas, M. D. Duez, E. O'Connor, C. D. Ott, L. Roberts, L. E. Kidder, J. Lippuner, H. P. Pfeiffer, and M. A. Scheel, Phys. Rev. D **93**, 044019 (2016), arXiv:1510.06398 [astro-ph.HE] .

[34] R. Haas, C. D. Ott, B. Szilágyi, J. D. Kaplan, J. Lippuner, M. A. Scheel, K. Barkett, C. D. Muhlberger, T. Dietrich, M. D. Duez, F. Foucart, H. P. Pfeiffer, L. E. Kidder, and S. A. Teukolsky, Phys. Rev. D **D93**, 124062 (2016), arXiv:1604.00782 [gr-qc] .

[35] J. Hesthaven and T. Warburton, *Nodal Discontinuous Galerkin Methods: Algorithms, Analysis, and Applications* (Springer, Berlin, New York, 2008).

[36] D. A. Kopriva, *Implementing spectral methods for partial differential equations: Algorithms for scientists and engineers* (Springer, Berlin, New York, 2009).

[37] J. Hesthaven, S. Gottlieb, and D. Gottlieb, *Spectral Methods for Time-Dependent Problems* (Cambridge University Press, Cambridge, UK, 2007).

[38] M. A. Scheel, H. P. Pfeiffer, L. Lindblom, L. E. Kidder, O. Rinne, and S. A. Teukolsky, Phys. Rev. D **74**, 104006 (2006), gr-qc/0607056 .

[39] F. Pretorius, Class. Quantum Grav. **22**, 425 (2005), gr-qc/0407110 .

[40] C. Gundlach, G. Calabrese, I. Hinder, and J. M. Martin-Garcia, Class. Quantum Grav. **22**, 3767 (2005), gr-qc/0504114 .

[41] L. Lindblom, M. A. Scheel, L. E. Kidder, R. Owen, and O. Rinne, Class. Quantum Grav. **23**, S447 (2006), gr-qc/0512093 .

[42] J. A. Font, Living Rev. Rel. **11** (2008), 10.12942/lrr-2008-7.

[43] F. Banyuls, J. A. Font, J. M. Ibáñez, J. M. Martí, and J. A. Miralles, Astrophys. J. **476**, 221 (1997).

[44] F. Galeazzi, W. Kastaun, L. Rezzolla, and J. A. Font, Phys. Rev. D **88**, 064009 (2013), arXiv:1306.4953 [gr-qc] .

[45] A. Harten, P. D. Lax, and B. van Leer, SIAM Review **25**, 35 (1983).

[46] E. F. Toro, *Riemann solvers and Numerical Methods for Fluid Dynamics: A Practical Introduction* (Springer, Berlin, New York, 2013).

[47] S. F. Davis, SIAM Journal on Scientific and Statistical Computing **9**, 445 (1988).

[48] B. Cockburn, J. Comput. Appl. Math. **128**, 187 (2001).

[49] S. A. Moe, J. A. Rossmanith, and D. C. Seal, ArXiv e-prints (2015), arXiv:1507.03024 [math.NA] .

[50] S. Gottlieb, C.-W. Shu, and E. Tadmor, SIAM Review **43**, 89 (2001).

[51] M. Alcubierre, B. Brügmann, P. Diener, M. Koppitz, D. Pollney, E. Seidel, and R. Takahashi, Phys. Rev. D **67**, 084023 (2003), gr-qc/0206072 .

[52] C. W. Misner, K. S. Thorne, and J. A. Wheeler, *Gravitation* (Freeman, New York, New York, 1973).

[53] F. C. Michel, Astrophysics and Space Science **15**, 153 (1972).

[54] B. Cockburn, S.-Y. Lin, and C.-W. Shu, Journal of Computational Physics **84**, 90 (1989).

[55] J. Centrella and J. R. Wilson, Astrophys. J. Suppl. Ser. **54**, 229 (1984).

[56] L. Del Zanna and N. Bucciantini, Astron. Astrophys. **390**, 1177 (2002), astro-ph/0205290 .

[57] A. Mignone, T. Plewa, and G. Bodo, Astrophys. J. Suppl. Ser. **160**, 199 (2005), astro-ph/0505200 .

[58] R. C. Tolman, Phys. Rev. **55**, 364 (1939).

[59] J. R. Oppenheimer and G. M. Volkoff, Phys. Rev. **55**, 374 (1939).

[60] J. A. Font, T. Goodale, S. Iyer, M. Miller, L. Rezzolla, E. Seidel, N. Stergioulas, W.-M. Suen, and M. Tobias, Phys. Rev. D **65**, 084024 (2002), gr-qc/0110047 .

[61] J. D. Hunter, Comput. Sci. Eng. **9**, 90 (2007).

[62] C. Ronchi, R. Iacono, and P. S. Paolucci, J. Comput. Phys. **124**, 93 (1996).

[63] S. Refsdal, Mon. Not. Roy. Astr. Soc. **128**, 295 (1964).

[64] R. D. Blandford and R. Narayan, Annual Review of Astronomy and Astrophysics **30**, 311 (1992).

[65] N. Inada, M. Oguri, B. Pindor, J. F. Hennawi, K. Chiu, W. Zheng, S.-I. Ichikawa, M. D. Gregg, R. H. Becker, Y. Suto, *et al.*, Nature **426**, 810 (2003).

[66] N. Inada, M. Oguri, T. Morokuma, M. Doi, N. Yasuda, R. H. Becker, G. T. Richards, C. S. Kochanek, I. Kayo, K. Konishi, H. Utsunomiya, M.-S. Shin, M. A. Strauss, E. S. Sheldon, D. G. York, J. F. Hennawi, D. P. Schneider, X. Dai, and M. Fukugita, Astrophys. J. Lett. **653**, L97 (2006).

[67] C. T. Cunningham and J. M. Bardeen, Astrophys. J. Lett. **173**, L137 (1972).

[68] J.-P. Luminet, Astron. Astrophys. **75**, 228 (1979).

[69] F. Vincent, T. Paumard, E. Gourgoulhon, and G. Perrin, Class. Quantum Grav. **28**, 225011 (2011), arXiv:1109.4769 [gr-qc] .

[70] T. Müller, Comput. Phys. Commun. **185**, 2301 (2014).

[71] S. D. Majumdar, Phys. Rev. **72**, 390 (1947).

[72] A. Papapetrou, Proc. Roy. Irish Acad. **A 51**, 191 (1947).

[73] D. Kastor and J. Traschen, Phys. Rev. D **47**, 5370 (1993), hep-th/9212035 .

[74] D. Nitta, T. Chiba, and N. Sugiyama, Phys. Rev. D **84**, 063008 (2011), arXiv:1106.2425 [gr-qc] .

[75] A. Yumoto, D. Nitta, T. Chiba, and N. Sugiyama, Phys. Rev. D **86**, 103001 (2012), arXiv:1208.0635 [gr-qc] .

[76] `http://www.black-holes.org/lensing`.

[77] J. Centrella, J. G. Baker, B. J. Kelly, and J. R. van Meter, Rev. Mod. Phys. **82**, 3069 (2010), arXiv:1010.5260 [gr-qc] .

[78] H. P. Pfeiffer, Class. Quantum Grav. **29**, 124004 (2012), arXiv:1203.5166 [gr-qc] .

[79] R. Arnowitt, S. Deser, and C. W. Misner, in *Gravitation: An Introduction to Current Research*, edited by L. Witten (Wiley, New York, 1962) pp. 227–265, gr-qc/0405109 .

[80] "Simulating eXtreme Spacetimes," (), `http://www.black-holes.org/`.

[81] `http://www.black-holes.org/waveforms` ().

[82] S. A. Hughes, C. R. Keeton, II, P. Walker, K. T. Walsh, S. L. Shapiro, and S. A. Teukolsky, Phys. Rev. D **49**, 4004 (1994).

[83] F. H. Vincent, E. Gourgoulhon, and J. Novak, Class. Quantum Grav. **29**, 245005 (2012), arXiv:1208.3927 [gr-qc] .

[84] M. F. Skrutskie, R. M. Cutri, R. Stiening, M. D. Weinberg, S. Schneider, J. M. Carpenter, C. Beichman, R. Capps, T. Chester, J. Elias, J. Huchra, J. Liebert, C. Lonsdale, D. G. Monet, S. Price, P. Seitzer, T. Jarrett, J. D. Kirkpatrick, J. E. Gizis, E. Howard, T. Evans, J. Fowler, L. Fullmer, R. Hurt, R. Light, E. L. Kopan, K. A. Marsh, H. L. McCallon, R. Tam, S. V. Dyk, and S. Wheelock, Astron. J. **131**, 1163 (2006).

[85] S. Mollerach and E. Roulet, *Gravitational Lensing and Microlensing* (World Scientific, 2002).

[86] A. Einstein, Science **84**, 506 (1936).

[87] H. Thirring, Physikalische Zeitschrift **19**, 33 (1918).

[88] H. Thirring, Physikalische Zeitschrift **22**, 29 (1921).

[89] N. W. Taylor, M. Boyle, C. Reisswig, M. A. Scheel, T. Chu, L. E. Kidder, and B. Szilágyi, Phys. Rev. D **88**, 124010 (2013), arXiv:1309.3605 [gr-qc] .